SPECTRUM MANAGEMENT FOR HIGH EFFICIENCY PHOTONIC DEVICES

BY

OSMAN SAFA CIFCI

DISSERTATION

Submitted in partial fulfillment of the requirements
for the degree of Doctor of Philosophy in Materials Science and Engineering
in the Graduate College of the
University of Illinois at Urbana-Champaign, 2018

Urbana, Illinois

Doctoral Committee:

Professor Paul V. Braun, Chair
Professor Moonsub Shim
Assistant Professor Qian Chen
Associate Professor Kimani C. Toussaint, Jr.

ABSTRACT

Spectrum management holds great promise for high-performance photonics devices. Optical elements that split, up- or down-convert the available light to a specified spectrum can result in higher efficiencies in various devices such as photovoltaic cells, photodetectors, and electronic displays.

In this thesis, the method of spectrum splitting to efficiently utilize the full spectrum of sunlight in converting from solar energy to electricity was demonstrated. Multi-junction solar cells are already efficient, but further gains are possible by splitting the solar spectrum laterally, rather than vertically, onto electrically isolated cells. A textured thin film was used to diffract two spectral bands to laterally displaced regions in the far field. The optimized optical element having multi-level textures was fabricated using 3D direct laser writing on photoresist. The fabricated samples were optically characterized and potential modifications to achieve even higher efficiencies were pointed out.

Further, this thesis demonstrated a new display architecture that can alleviate problems associated with liquid crystal display (LCD) devices: substantial losses in optical intensity due to employed color filters and low ambient contrast ratio because of reflection of external light from the front surface. A luminescent film having quantum dots was placed inside an enclosed microcavity. The design for a high-contrast and high efficiency display comprised an enclosed cavity having a front wall and a back wall, where the front wall comprised a pinhole opening for emission of light from the cavity and the back wall was configured to transmit light into the cavity. The outer surface of the front wall was made to absorb substantially all optical wavelengths of externally incident light so as to appear black. The inner surface of the front wall

and sidewalls were highly reflective to promote photon recycling within the cavity and light emission through the pinhole opening.

Finally, although the single pixel demonstration served to optimize the optics within the cavity and study the physics of the proposed architecture, a micrometer sized pixel array was proposed since the current portable electronics industry demands displays with large pixel arrays, where each pixel is on the order of micrometers in size. An individually addressable micropixel array was proposed and fabricated using standard microfabrication techniques that can be integrated into commercial displays.

ACKNOWLEDGEMENTS

I feel privileged to have Prof. Paul Braun as my PhD advisor. Without him, I could not even imagine how hard the past six years would be. His teachings on how to tackle problems and how to approach research, on both high-level as well nitty-gritty details. I greatly appreciate his constant encouragement, support and guidance during my PhD. I also learnt the importance of having a broad knowledge and coming up with solutions utilizing seemingly unrelated areas. All the skills and insights will be there to stay with me and I hope that I can carry them during my journey.

I also would like to thank my committee members, Prof. Kimani C. Toussaint, Prof. Moonsub Shim, and Prof. Qian Chen. I am very grateful to have the opportunity to work in Photonics Research of Bio/Nano Environments lab led by Prof. Toussaint and learn from his students. Your contributions and feedbacks to my work are greatly appreciated. I would also appreciate Prof. Ralph Nuzzo and Prof. Eli Yablonovitch which I collaborated for various projects. It was always great to work with their students. It was a great pleasure to collaborate with Lu Xu and Mikayla Anderson in Nuzzo lab.

I would like to specially thank my labmates which I shared so much time with making research fun. Some of these great individuals are Sanghyeon Kim, Runyu Zhang, Jin Gu Kang, Eric Epstein, Dr. Pengcheng (Isa) Sun, Dr. Matthew Goodman, Kaitlin Tyler, Subing Qu. It was great pleasure to work with these talented people and helpful discussions helped me tremendously. Dr. Serkan Demir and Dr. Adem Kocyigit had a special place in my heart which I spent a lot of time discussing and executing experiments. Many staff members at Materials Research Laboratory (MRL) and Micro-Nano Mechanical Systems (MNMS) Cleanroom also

contributed a lot to my success in research by offering equipment training and support. Tao Shang, Julio Soares, Xiaoli Wang, Fubo Rao, Mauro Sardela, Glennys Mensing and Joseph Maduzia were always available to help.

Finally, I must acknowledge my parents that raised me and supported me all those years but I hope all those years to receive my PhD is worth it. Last but not least, I am incredibly indebted to my wife Kezban which gave me unlimited support all along these years and gave us a son which became the joy of our life.

TABLE OF CONTENTS

CHAPTER 1

INTRODUCTION

1.1 Spectral Light Management

Visible light spans a wavelength range of 400 to 700 nm. For certain applications such as solar cells, displays, and photodetectors it is advantageous to use a small portion of the accessible light for enhanced efficiency and functionality. Spectral light management usually involves using additional optical components to filter a certain portion of the available spectrum to achieve better performance. Spectrum management can be subcategorized into spectral beam splitting, separation of the incoming light into multiple bands, and spectral modification, altering the spectrum of incoming light using up or down conversion.[1]

Photovoltaics is an area where spectrally-selective optical structures are shown to improve device efficiency.[2] The origin of solar radiation is thermal and thus makes the sunlight broadband covering from ultraviolet to mid infrared.[3] A photovoltaic cell, made of a semiconductor material, is most efficient at a single wavelength. When the incoming photon has higher energy than the bandgap of the semiconductor material, the photon gives away energy to the lattice to match the bandgap thus partially losing its energy. On the flip side, when the incoming photon has a lower energy than the bandgap of the semiconductor material, the photon is transmitted through the material and the photon's energy is completely lost. As analyzed by Shockley-Queisser[4] maximum efficiency of a single semiconductor photovoltaic system is limited to 33%. Splitting the sunlight laterally and employing different semiconductor absorbers can enable higher efficiencies due to reduced losses. Several optical systems have been proposed to split the sunlight for higher photovoltaic efficiency.

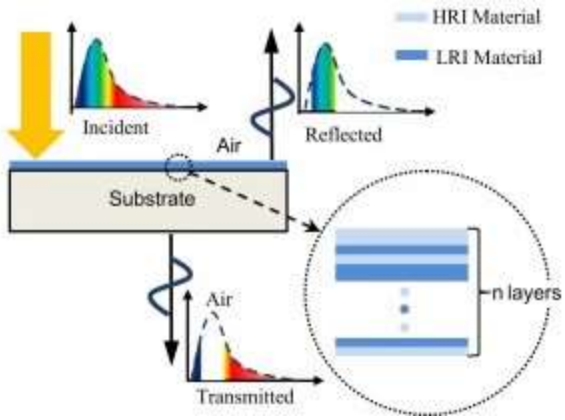

Figure 1.1 Schematic of thin film dichroic mirrors made of n layers[5].

One of the proposed optical element to split sunlight is dichroic filters. The idea behind dichroic filters is to rely on constructive or destructive interference caused by thin-film layers to selectively transmit or reflect a particular portion of the incoming light.[5] One common method of producing a dichroic filter is to deposit alternating layers of materials with different refractive index, such as shown in **Figure 1.1**. Alternatively, a continuous change in refractive index layer could be employed. Such structures are called rugate filters. Vacuum deposition techniques such as physical vapor deposition or chemical vapor deposition is used to deposit different layers. Dichroic filters is a mature technology with an established theory behind it[6] and there are several commercial products that can be used for spectrum splitting. In order to efficiently split the solar spectrum, many layers are necessary. Since the deposition of the layers require vacuum deposition techniques, production of highly efficient filters are complex and costly.[7] So, a trade-off is mandatory to have a balance between cost and efficiency. A significant disadvantage of dichroic filters is the sensitivity of incidence angle because with changing incident angle optical path changes and the reflection band shifts. This is especially problematic when the photovoltaic system employs an optical concentration using elements such as lenses because a cone of

incoming angles generated.[8] Regardless, the oscillating nature of solar incoming angle with season and time of the day makes tracking mandatory. Another important shortcoming of dichroic filters is non-negligible absorption especially in the ultraviolet region.[910]

Another proposed method of splitting incoming solar radiation is to use diffractive optical elements (DOE). These elements diffract light by employing surface relief structures or volume phase gratings. Angular steering of DOEs are based on the size of the slits, wavelength of the light as well as angle of incidence. These elements can be tailored to diffract desired spectral bands of the source light. An important advantage of DOE is the simultaneous splitting and concentration[11] as shown in **Figure 1.2**.

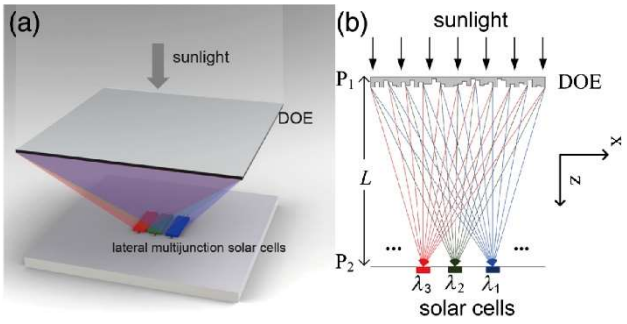

Figure 1.2 a) Schematic of lateral DOE with lateral solar cells b) Cross-section view of DOE[11].

DOEs are usually made out of plastic and can be fabricated by lithography. Since, it has various height structures, multiple lithography steps are needed. Alternative methods such as electron beam lithography or laser direct writing can offer a slower but more straightforward method.[11] However, the cost of lithography is still a considerable concern. Just like dichroic filters, DOEs are also sensitive to the incidence angle of sunlight and needs to be placed on a tracker. So, a trade-off between cost and additional efficiency needs to be analyzed when designing DOEs. So far, the published work on DOEs has mostly focused on various simulations

and proof-of-concept designs mostly in very small scale. There has been no outdoor demonstration in practical scale which is probably due to the cost of making DOEs.

The third method of making spectrum splitters it to use refractive elements which has a significant dispersion characteristic. As the incoming sunlight passes through the refractive element, different wavelengths of light can be collected spatially separate locations. One of the most familiar refractive elements is the prism. When a collimated light propagates through a prism different sub-bands of the sunlight are directed toward different regions.[12] By carefully tailoring the design, it is possible to refract light into focal regions[13] as shown in **Figure 1.3**.

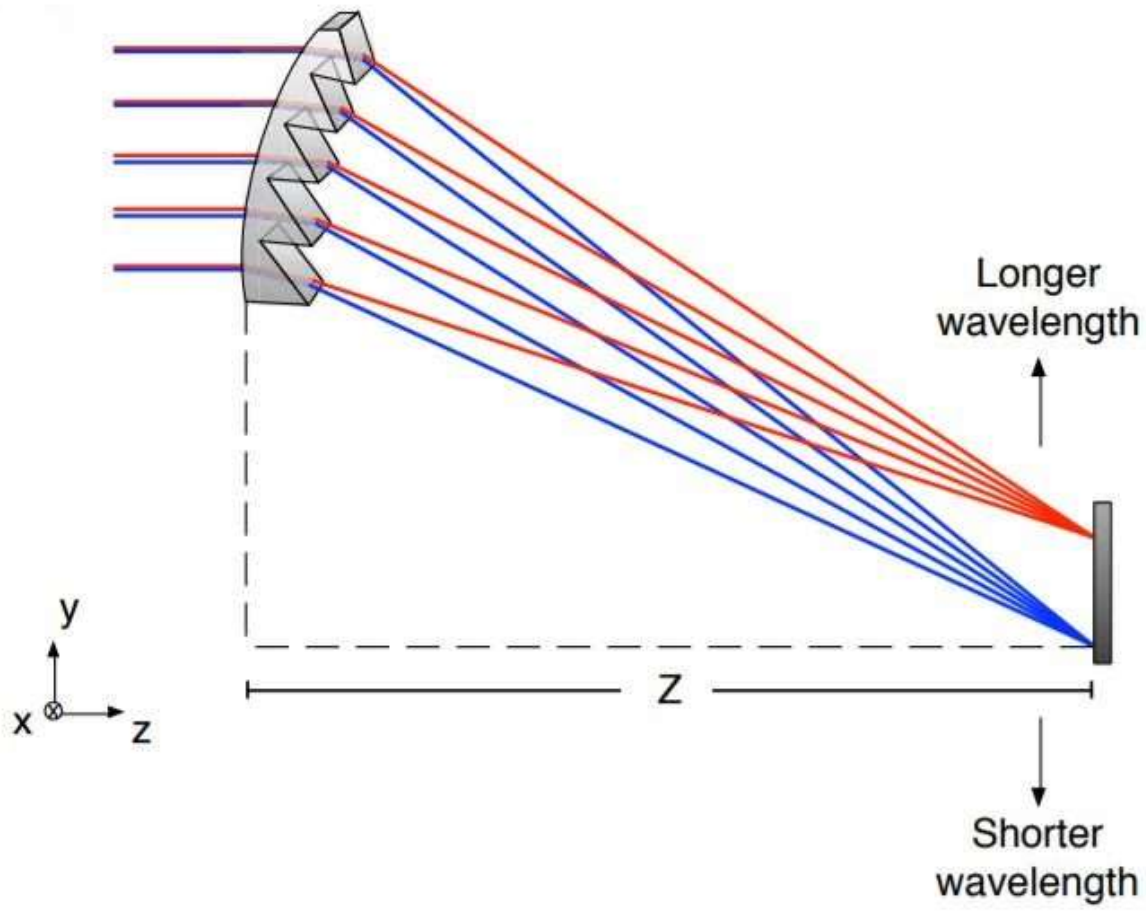

Figure 1.3 Conceptual drawing of the refractive optical element[13].

A significant advantage of using refractive elements is the mature technology of the employed optical elements. One important requirement of refractive elements is the high quality surface finish to eliminate any unwanted light scattering and there are methods such as diamond turning[14] and injection molding[15] that are shown to produce elements with optically smooth surfaces. The most important drawback of such elements is the use of bulky optics which mandates a big footprint.

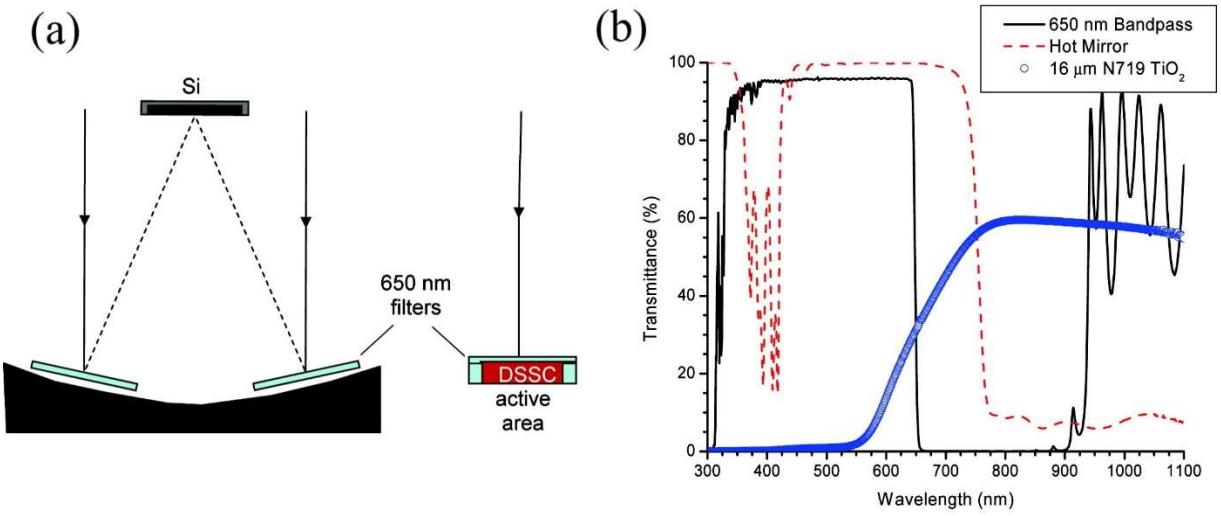

Figure 1.4 a) Schematic of PV-assisted spectrum splitting system b) The spectral transmission of the optical elements in the system[16].

Another approach to spectral management of light is to use photovoltaic (PV) cells' intrinsic properties. Being a semiconductor, a PV cell is transparent to the light that has energy less than the band gap of the cell. When a reflector is placed at the back of a PV cell, any light that does not absorbed by the PV cell could be directed to another PV cell[16] to be absorbed as shown in **Figure 1.4**. In the mentioned study, the photons below 650 nm wavelength will be absorbed by the DSSC cell, the range where the cell is the most efficient. On the other hand, the photons above 650 nm wavelength will be reflected to Si solar cell and could still be efficiently

converted into electricity. Using multijunction solar cells[17] employs a similar approach. They are made up of stacking higher bandgap PV cells on top of lower bandgap cells. In multijunction solar cells, the most energetic photons are absorbed at the top cells and the least energetic photons are absorbed at the bottom cell. So, each PV cell can be thought of a bandpass filter.

The last optical element that could be used to spectrally manage the incoming light is the luminescent solar concentrator (LSC) and is described in detail in **Section 1.4**.

1.2 Color Generation

One of the easiest method of generating colors is to use colorant-based pigmentation. These kind of colors stem from the selective absorption of light by the molecules embedded in materials.[1819] However, it is possible to generate colors without pigments by employing spatial structures. This type of coloration stems from the interaction of the incoming light with spatial structures. These structures tend to be in the submicron scale for visible colors and it can even be observed in the nature.[20]

There are several mechanism to generate structural colors.[18] **Figure 1.5** illustrates some of the mechanisms. The first method to generate colors is to use a reflective diffraction grating (**Figure 1.5b**). When the sample is illuminated as in **Figure 1.5a** in addition to reflected beam there are additional beam at angles satisfying diffraction equation. Another method is to rely on thin film interference (similar to dichroic filters mentioned in the previous section) as shown in **Figure 1.5c**. Third method to generate colors without pigments is to employ photonic crystals[21] which can have one, two or three dimensional periodicity. Photonic crystals possess a spatially periodic refractive index (**Figure 1.5d**). In case of one dimensional photonic crystals, the physics of operation is very similar to a dichroic filter and it is easier to compute the expected reflection

band. For two and three dimensional structures, the aim is to obtain the "photonic band-gaps" which are the frequency ranges where the propagation of light is prohibited by the crystal. Another method of having structured color is to use scattering medium and is shown in **Figure 1.5e**. The reflectance of incoming light from a scattering medium made up of small particles depends on the wavelength. Scattering is what gives white color to milk and blue color to sky.

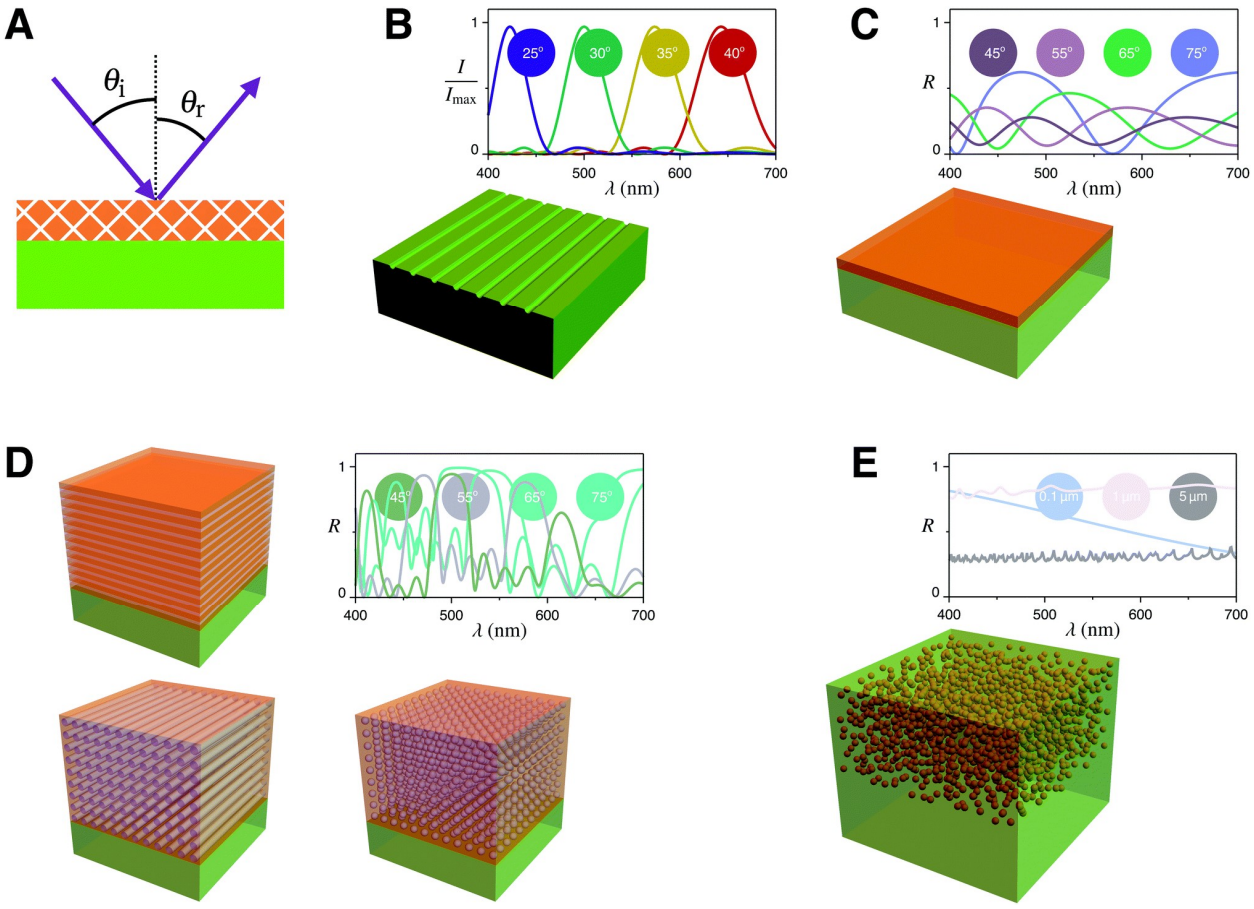

Figure 1.5 a) Incidence and reflectance waves b) A reflective diffraction grating c) Color generation using thin-film interference effect d) One, two and three dimensional photonic crystal e) Light generation using scattering[18].

Another method of producing colors using spatial structures is to use nanopatterned metal films and rely on surface-plasmon resonance[1922] which does not exist in nature and is relatively a

less mature field. Surface plasmons are collective oscillations of electrons that exist at the metal-dielectic surface. They support resonant interactions with incoming light. By carefully tuning the design parameters, it is possible to produce structures that reflects or transmits light at the desired wavelength. An important property of surface-plasmon based devices is that they tend to be much smaller than other methods. This can significantly reduce the footprint at the expense of costly nanofabrication. An example of a surface-plasmon color filter is shown in **Figure 1.6**. A silver nanorod array with changing diameter has a changing reflection peak which can be used as a color filter.

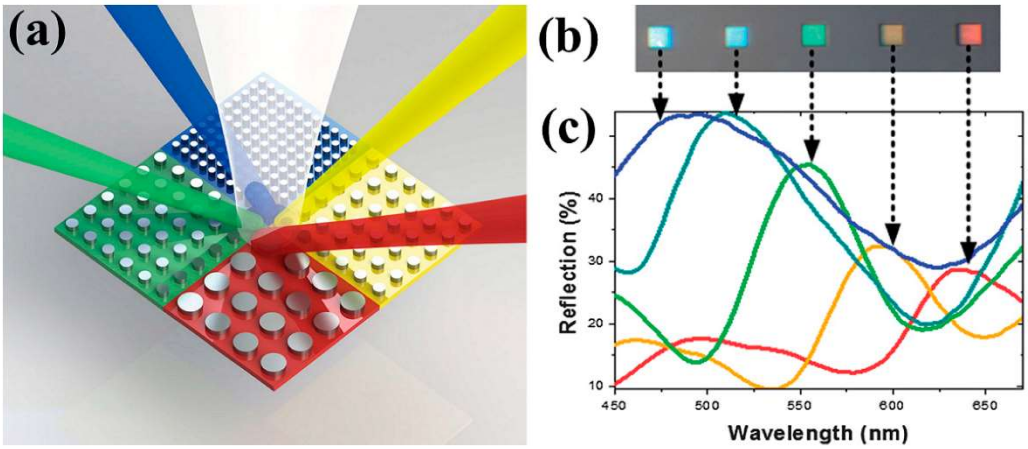

Figure 1.6 a) Schematic of a reflective plasmonic color filter b) Photograph and c) Measured reflection of the color filter.

1.3 Display Technology and Use of Quantum Dots

One of the most fundamental requirements for an electronic display is to convert an electrical signal into a visible change.[23] Two fundamentally different display architectures can achieve this feature. The first method is to emit light directly (emissive display) and the second one is to modulate the ambient light or light from a source (non-emissive display).

Being non-emissive, a liquid crystal display (LCD) is by far the most widely used flat display technology today, dominating the market with roughly 90% share[24] (as detailed in **Figure 1.7)** because these LED-backlit devices are less expensive and more reliable to produce. LCD relies on the effect of directing liquid crystal orientation with a voltage bias. Discovered almost 130 years ago by a botanist named Reinitzer, liquid crystals have properties intermediate between classical liquids and solids, which means they have long-range crystallinity over a limited physical range. The first industrial application of liquid crystals reported changes in optical transmission of thin films under applied voltage.[25] This illustration paved the road to more sophisticated design in just a few years.[26]

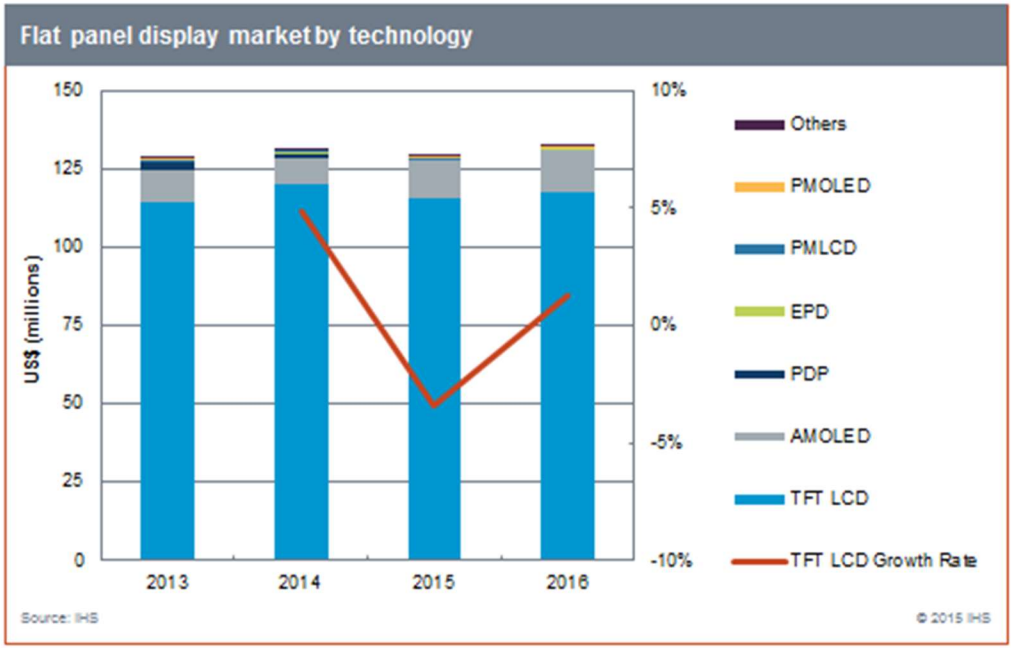

Figure 1.7 Image showing the market share of several technologies in the flat panel display industry. The data from 2016 is extrapolated based on the previous years. Taken from[24].

One simple type of liquid crystal is a twisted nematic cell. In an LCD employing twisted nematic cell, liquid crystals are twisted by 90° continuously from one side of the substrate to the

other, creating an optically active medium that rotates the polarization of light propagating through the cell. However, when a high enough electric field is applied, the continuous orientation of liquid crystals is frustrated except at the boundary layers and incoming light does not undergo polarization rotation. By employing appropriate polarizers, the display has the ability to modulate the incoming light, which can transmit or block the light coming from the source with the help of an applied voltage. A basic illustration is shown in **Figure 1.8.**[27]

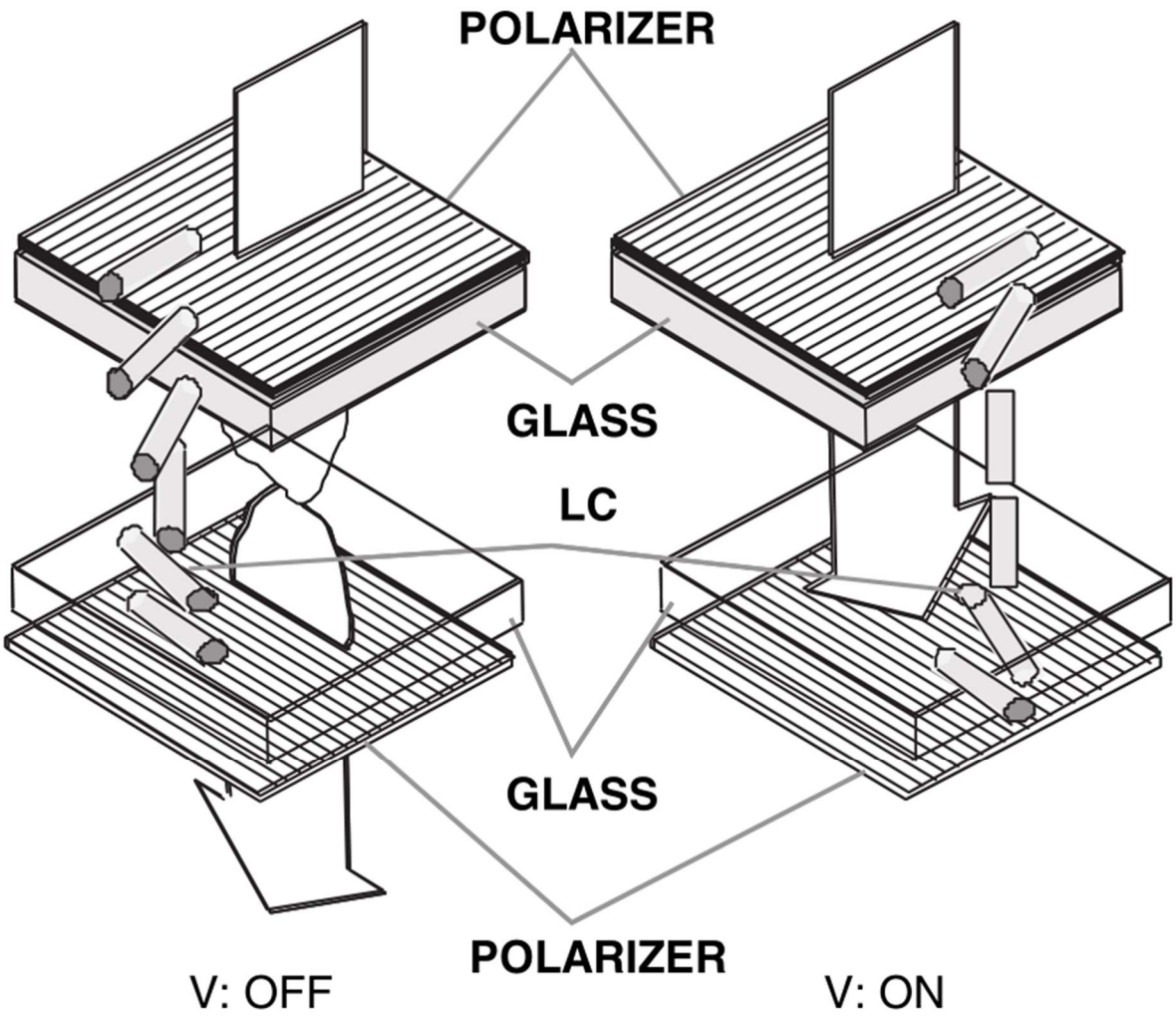

Figure 1.8 Device layout and operation principle of a twisted nematic liquid crystal cell. V: OFF corresponds to 0 V and V: ON corresponds to 5 V. Taken from[27].

A backlight is needed for an LCD since it does not emit light. Cold cathode fluorescent lamps were used as the light source before being replaced by LEDs. Additionally, to have a homogenous light, a diffuser is used after the light source. Apart from liquid crystals and polarizers, an LCD houses a color filter array and electronic elements (transistors) to switch the pixels on and off. The complete design is shown in **Figure 1.9**.[27]

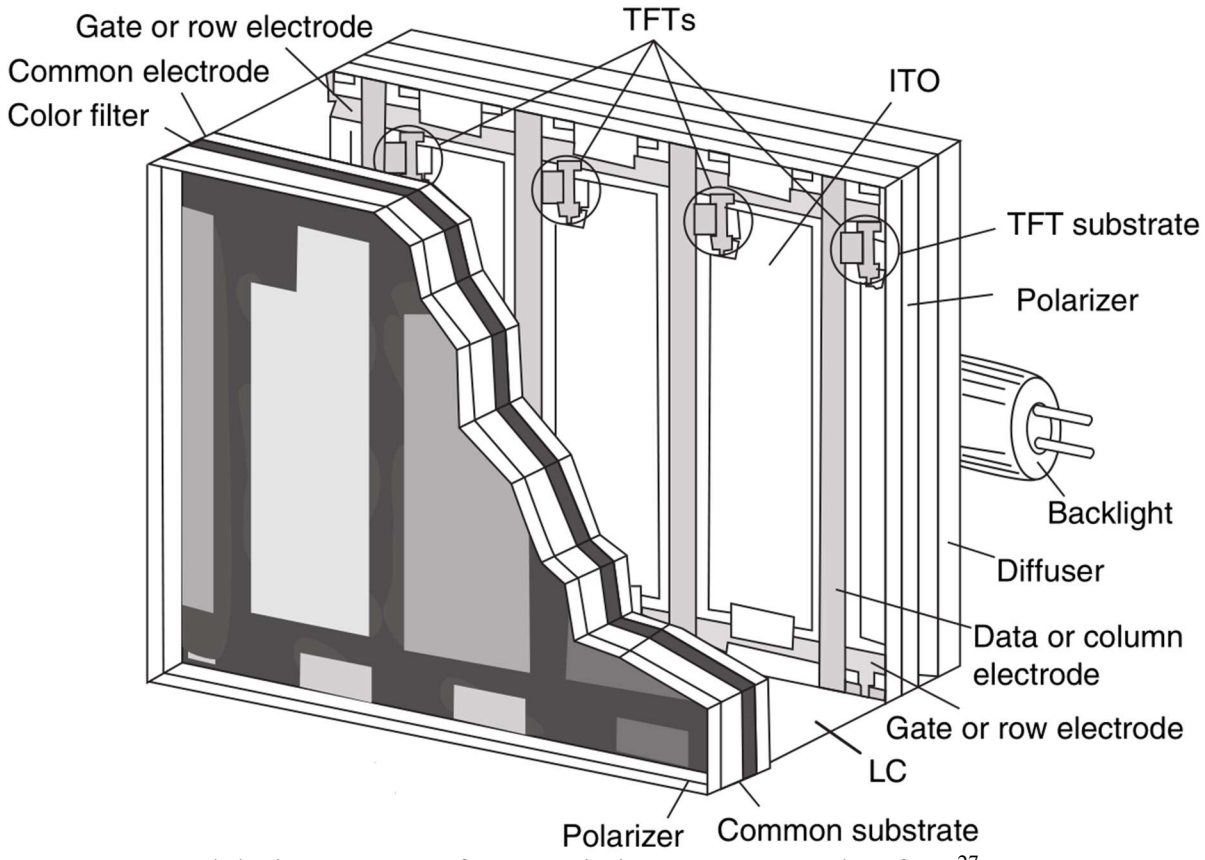

Figure 1.9 General device structure of a transmissive type LCD. Taken from[27].

LED-backlit LCD devices rely on phosphors to generate white light. However, the quality of the colors produced in a display using phosphors is poor compared to OLED devices.[28] Replacing phosphors with quantum dots, the displays can generate higher quality colors.

Quantum dot is a semiconductor nanocrystal whose size is sufficiently small (below 10 nm) in all three dimensions to show size dependent bandgap because of carrier confinement. The term QD was first coined in 1988 by Mark Reed.[29] The fine tuning of absorption and emission properties of these semiconductor nanocrystals, coupled with the ease of colloidal processing, has rendered these particles paramount for a wide variety of areas such as optics, electronics, and biology.[30]

Among the advantages of QDs are very narrow linewidth emission (a red phosphor has an emission linewidth of 55-65 nm[7]) and wide absorption range. Currently, due to the tight control of QD size and shape, linewidths below 30 nm are reached for green and red.[28] These linewidths can be made even smaller (10-20 nm) with the introduction of new QD shapes such as platelets[313233]. The effect of linewidth on color vibrancy can be seen in **Figure 1.10**.[28]

Ever-increasing demands by consumers require displays with more vibrant colors. In 1953, the National Television System Committee (NTSC) set the broadcast standards for color TV[34]. International Commission on Illumination (CIE) introduces a color space to represent visible light independent of the brightness. This color space is a 2D representation on an x-y grid which has a curved triangular shape that covers all the colors visible to the human eye. The wider coverage of this diagram means a wider range of colors, thus a more appealing view. The coverage of NTSC standards on CIE diagram is shown in **Figure 1.11**.[28]

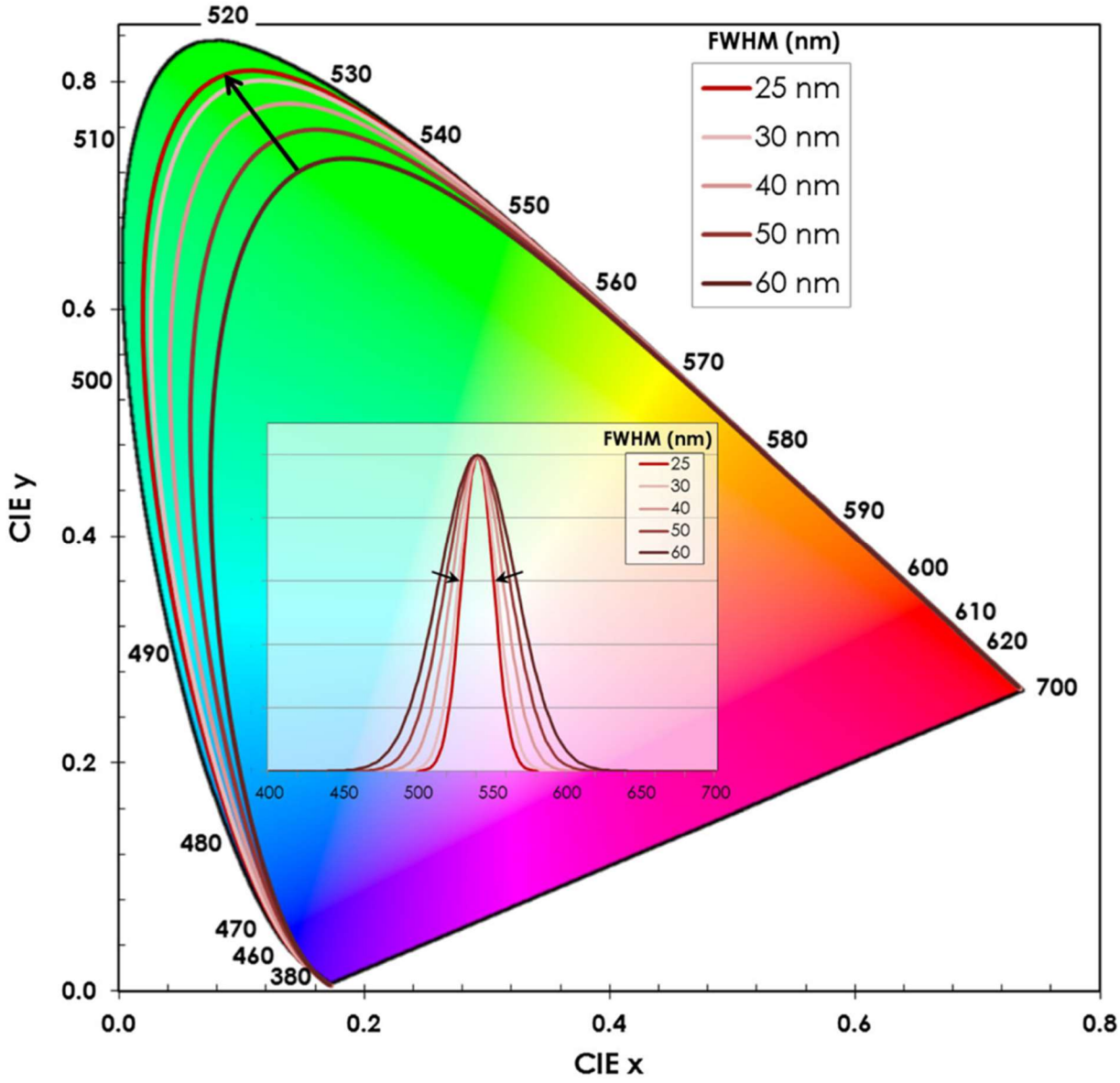

Figure 1.10 Simulation results showing the evolution of spectral locus position as full-width-at-half-maximum of the quantum dot emission narrows from 60 to 25nm (shown in the inset). Tighter linewidth emission corresponds to wider coverage of the CIE. Taken from[28].

It took many decades to finally reach 100% NTSC coverage (as mapped against CIE diagram) and a new emissive type organic light-emitting diode (OLED) display is responsible for this achievement in 2010s. For the case of LCDs, a white LED, made by dispersing phosphors on a blue LED, is used as the light source, but the broad emission by the phosphors causes poor

color gamut,[28] and LCDs can only achieve 70% coverage of the NTSC.[34] There are two possible ways of producing more vibrant colors. One is to design a very narrow filter, and the other one is to use a small, particular color portion of the light source. Using a very narrow filter causes more light to be absorbed and leads to even lower light transmission. The standard color filter array has a transmission value of around 25% as seen in **Figure 1.12,**[35] and overall transmission of an LCD is 6-7%.[27] Thus, further transmittance reduction is undesirable.

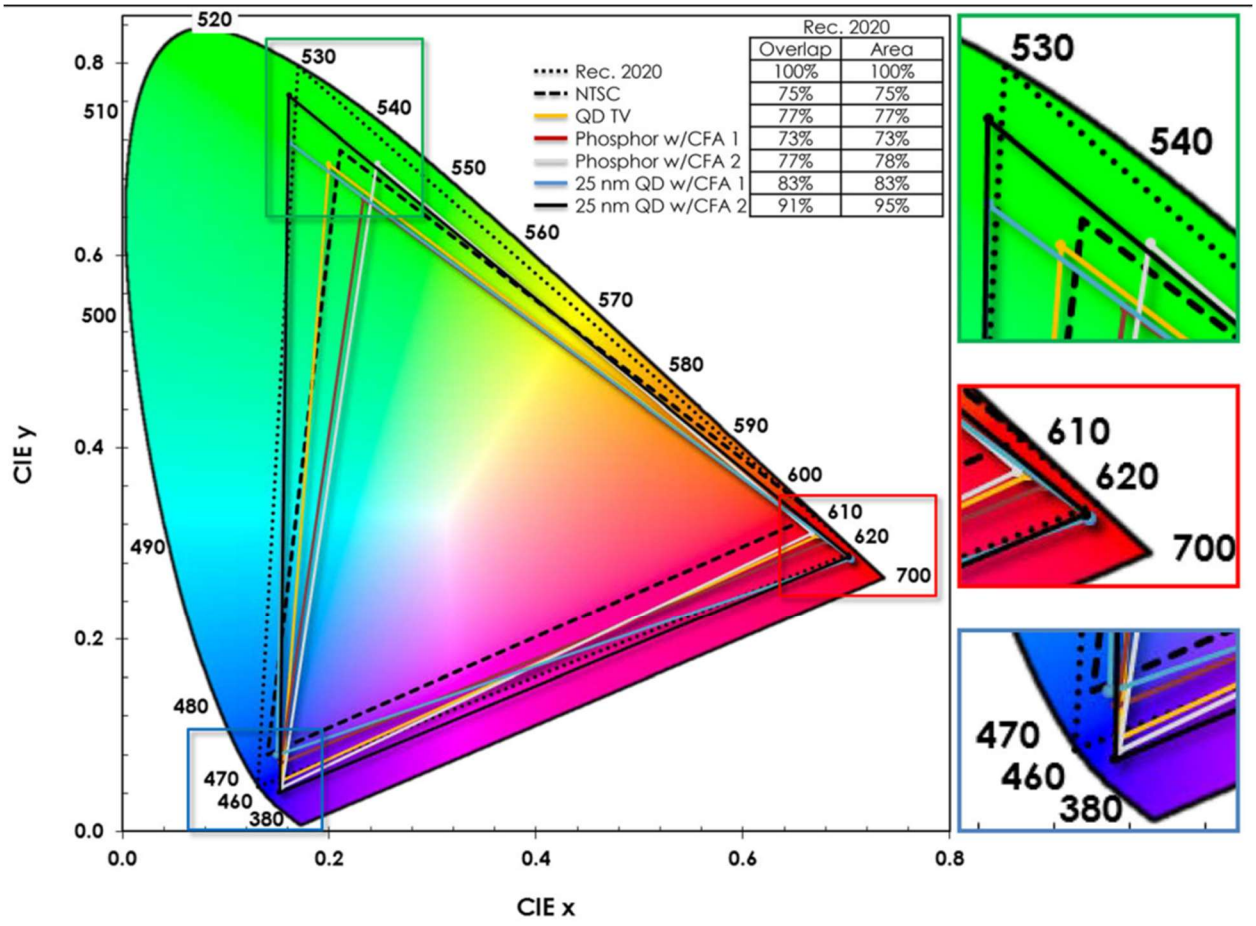

Figure 1.11 Gamut triangles obtained by using phosphor and QD using two different color filter arrays. The phosphor is a combination of red $SrLiAl_3N_4$:Eu (52 nm linewidth) and green β-SiAlON:Eu (45 nm linewidth). The QD has a 25 nm linewidth. QD TV is the 55W900A TV from Sony. Rec. 2020 and NTSC reference gamut triangles are also shown. The results show wider color coverage for devices using QD. Taken from[28].

QD with the capability of achieving very narrow linewidths can solve the poor color gamut problem and two companies, QD Vision and Nanosys, are currently working on the integration of QD with LCD. There are already products such as the Amazon Kindle Fire HDX 9.7" Tablet that use QD in a display.[36] **Figure 1.12** shows how the QD can help achieve NTSC standards. With the introduction of QD, LCD can enjoy large color gamut on par with OLED displays, while still being cost-effective.

1.4 Luminescent Solar Concentrator

A luminescent solar concentrator (LSC) is comprised of glass or polymeric luminescent waveguide and represents a relatively simple alternative to sunlight collection.[37] It has several advantages over other concentrator designs such as potential low cost of production,[38] physical flexibility, and light weight.[39] Another significant advantage of the LSC is the ability to accept diffuse sunlight in addition to direct sunlight.[4041] On the other hand, non-luminescent solar concentrators usually have rigid, massive structures and can only receive direct sunlight. Thus, they need to be tracked precisely to maximize power output.

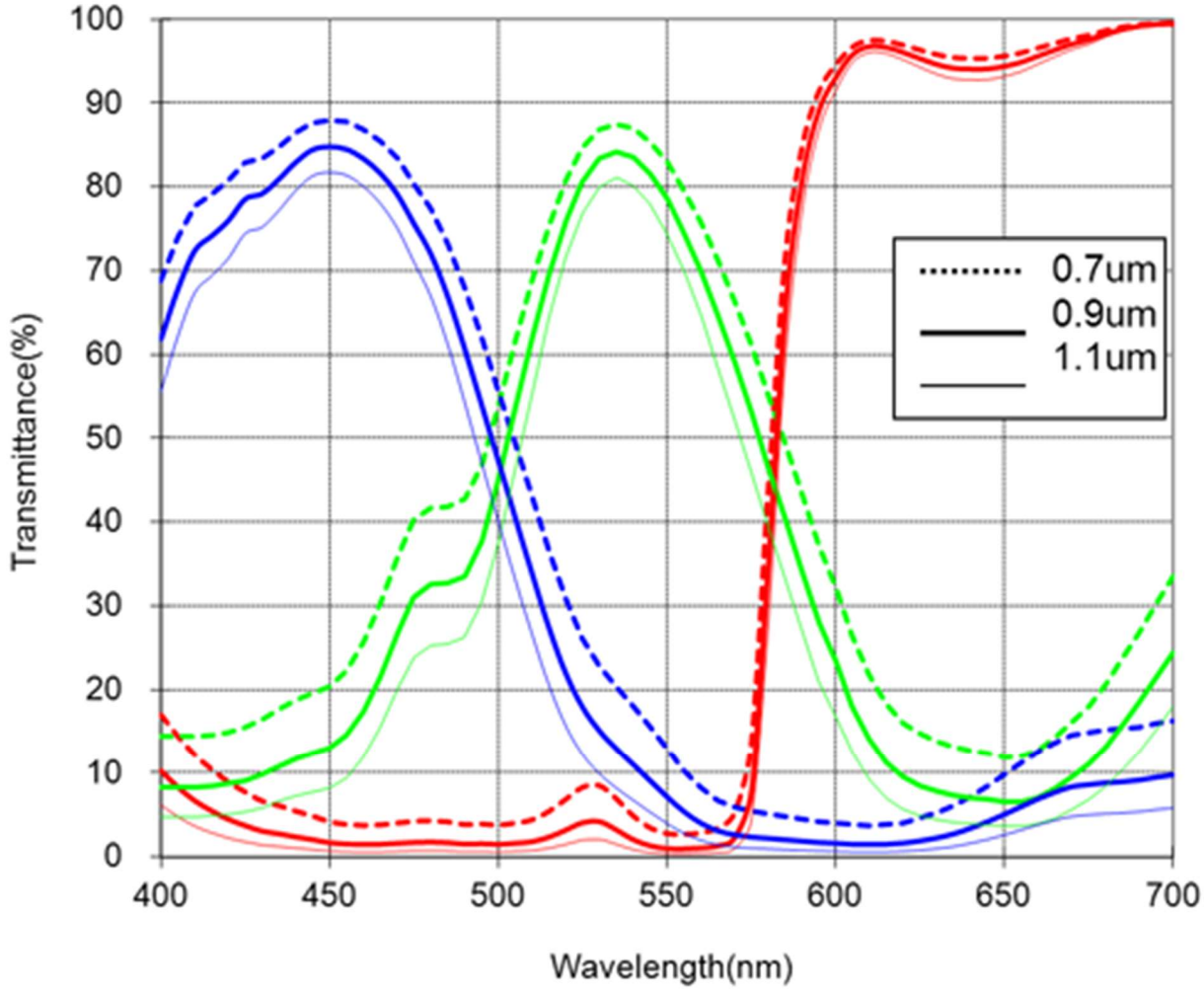

Figure 1.12 The transmission curve of the 5th generation of COLOR MOSAIC® filter by Fujifilm. Dashed, bold, and solid lines refer to color filter array thicknesses of 0.7, 0.9 and 1.1 μm. Taken from[35].

First introduced in 1973 by Lerner,[42] an LSC operates by taking in sunlight from the top, which is absorbed by the luminophores inside the polymeric or glass layer. The host layer also acts as a waveguide for the emitted light at longer wavelengths. The light propagation of the emitted light relies on total internal reflection, and some portion of the light makes it to the side

of the host layer, becoming concentrated in the meantime. A solar cell is attached to the side of the polymer or glass host material. The operation of LSC is shown in **Figure 1.13.**[37]

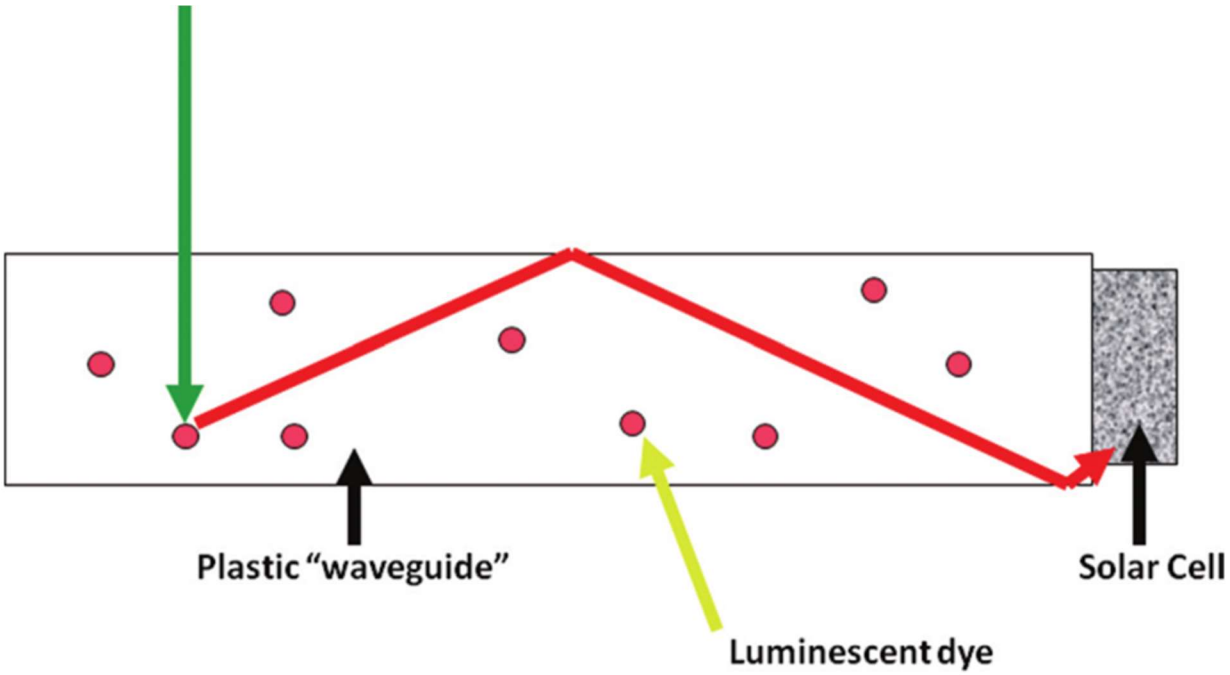

Figure 1.13 The operation of luminescent solar concentrator. Initially, the sunlight (shown in green arrow) enters the waveguide and is absorbed by a luminophore. The light is re-emitted at a longer wavelength (shown in red arrow) and a fraction of it is trapped by total internal reflection, whereas the rest escapes the waveguide. A photovoltaic cell is attached to the edge(s) of the waveguide. Taken from[37].

Although idealized more than 40 years ago, the LSC has not been commercialized yet due to relatively low efficiencies.[4344] There are several loss mechanisms in an LSC that are depicted in **Figure 1.14**[37]. The optical efficiency of the LSC can be formulated as:[45]

$$\eta_{opt} = (1 - R)P_{TIR}\eta_{abs}\eta_{PLQY}\eta_{Stokes}\eta_{host}\eta_{TIR}\eta_{self}$$

The first loss illustrates Fresnel losses, which are around 4% for the conventional host materials having refractive indices of around 1.5.[46] The second loss (P_{TIR}), which is around 25% of the

light, exists because light propagation inside the host relies on total internal reflection (TIR) and some fraction of the photons fall into the escape cone and permanently exit the structure. The third factor affecting the overall optical efficiency is the absorption efficiency (η_{abs}).

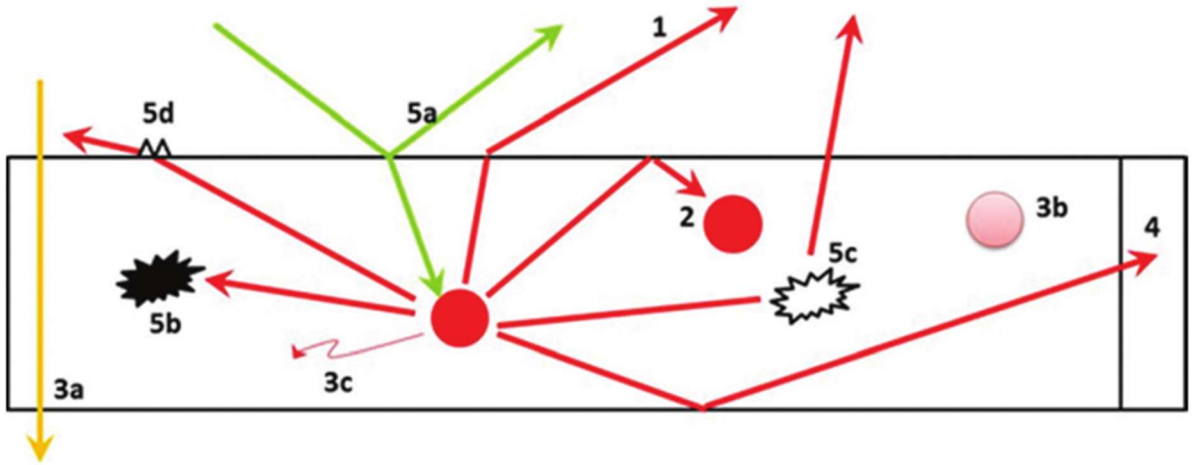

Figure 1.14 Different loss mechanisms in luminescent solar concentrators are shown. These are: 1) escape losses; 2) re-absorption of emitted light by another luminophore; 3a) lack of absorption by the luminophore; 3b) limited luminophore stability; 3c) imperfect quantum efficiency losses; 4) solar cell losses; 5a) Fresnel losses; 5b) absorption of emitted light by the host material; 5c) internal waveguide scattering; 5d) surface scattering. Taken from[37].

By design, LSC only absorbs a fraction of the solar spectrum, which is ideally all the wavelengths above the bandgap of the solar cell. For example, an LSC designed to absorb all the wavelengths above 550 nm has η_{abs} of 26%.[45] Another loss labeled as η_{PLQY} exists because the luminescent material does not have unity quantum yield. Because the emitted photon's energy is always less than the excitation photon's energy, there will be a loss which is called Stokes loss. The other two losses, which can be relatively small in an LSC, are the losses due to the absorption by the host material (η_{host}) and the losses due to scattering sites in the host material

(η_{TIR}). Finally, when the excitation and emission spectrum of a luminophore overlaps, there will be some reabsorption of the emitted photons by another luminophore (η_{self}).

Very recently,[47] with the use of omnidirectional, wavelength-selective optical filters and designer quantum dot materials, a solar concentration ratio of 30 was achieved. The wavelength-selective filter renders the device as a photonic cavity that efficiently transports photons to the solar cell. We propose to exploit a similar structure and use it for current LCDs to replace the color filters by concentrating photons to an exit aperture inside the pixel rather than placing a photovoltaic cell to that region. A figure illustrating our approach is shown on **Figure 1.15**. A high concentration ratio can improve the contrast ratio of the display and with the help of narrow linewidth emission of QD; vibrant colors can be observed in LCDs.

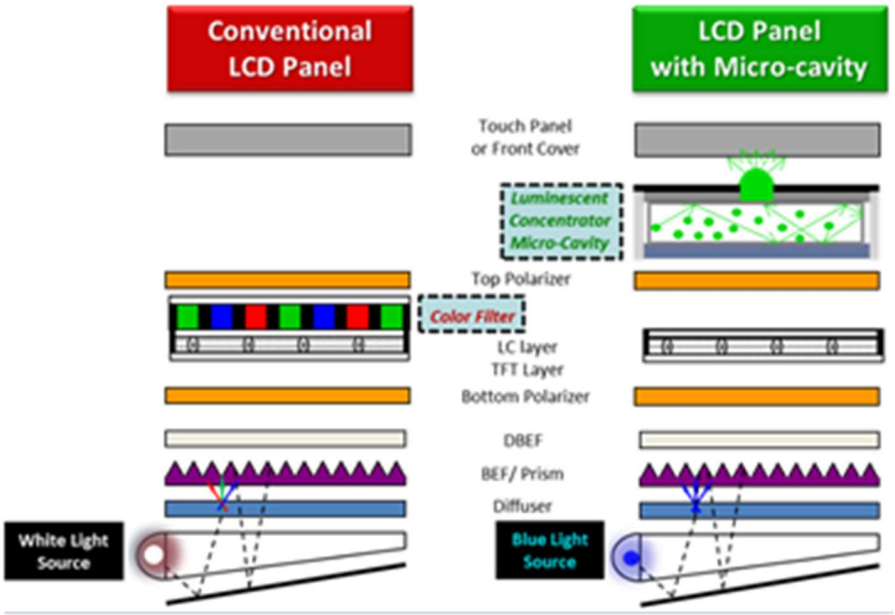

Figure 1.15 Schematic comparison of conventional LED optical display to our proposed micro-cavity design.

1.5 References

1. Stanley, C., Mojiri, A. & Rosengarten, G. Spectral light management for solar energy conversion systems. *Nanophotonics* (2016). doi:10.1515/nanoph-2016-0035
2. Peters, M. *et al.* Spectrally-Selective photonic structures for PV applications. *Energies* (2010). doi:10.3390/en3020171
3. Smith, E. V. P.; Zeilik, M.; Gregory, S. A. *Introductory Astronomy and Astrophysics*. (Saunders College Publishing, 1992).
4. Shockley, W. & Queisser, H. J. Detailed balance limit of efficiency of p-n junction solar cells. *J. Appl. Phys.* (1961). doi:10.1063/1.1736034
5. Mojiri, A., Taylor, R., Thomsen, E. & Rosengarten, G. Spectral beam splitting for efficient conversion of solar energy - A review. *Renew. Sustain. Energy Rev.* (2013). doi:10.1016/j.rser.2013.08.026
6. Macleod, A. Optical Thin Films. in *Handbook of Thin Film Deposition* (2012). doi:10.1016/B978-1-4377-7873-1.00009-7
7. Imenes, a. G., Buie, D., Mills, D. R., Schramek, P. & Bosi, S. G. A new strategy for improved spectral performance in solar power plants. *Sol. Energy* (2006). doi:10.1016/j.solener.2005.04.021
8. Zhang, D. *et al.* Optical performance of dichroic spectrum-splitting filters. *J. Photonics Energy* (2014). doi:10.1117/1.JPE.4.043095
9. Imenes, A. G., Fell, C. & Stein, W. *Spectral Beam Splitter for Solar Hydrogen Production*. (2007).
10. Crisostomo, F. *et al. Experimental testing of SiNx/SiO2 thin film filters for a concentrating solar hybrid PV/T collector*. *Renewable Energy* **72,** (2014).

11. Huang, Q. *et al.* Design and fabrication of a diffractive optical element as a spectrum-splitting solar concentrator for lateral multijunction solar cells. *Appl. Opt.* (2013). doi:10.1364/AO.52.002312

12. Huang, J., Fei, W.-C., Hsu, W.-C. & Tsai, J. Solar concentrator constructed with a circular prism array. *Appl. Opt.* (2010). doi:10.1364/AO.49.004472

13. Maragliano, C., Chiesa, M. & Stefancich, M. Experimental demonstration of a dispersive spectral splitting concentrator for high efficiency photovoltaics. in *MRS Advances* (2016). doi:10.1557/adv.2016.98

14. Brinksmeier, E., Gläbe, R. & Schönemann, L. Review on diamond-machining processes for the generation of functional surface structures. *CIRP Journal of Manufacturing Science and Technology* (2012). doi:10.1016/j.cirpj.2011.10.003

15. Sortino, M., Totis, G. & Kuljanic, E. Comparison of injection molding technologies for the production of micro-optical devices. in *Procedia Engineering* (2014). doi:10.1016/j.proeng.2014.03.122

16. Barber, G. D. *et al.* Utilization of direct and diffuse sunlight in a dye-sensitized solar cell - Silicon photovoltaic hybrid concentrator system. *J. Phys. Chem. Lett.* (2011). doi:10.1021/jz200112m

17. Zeitouny, J., Katz, E. A., Dollet, A. & Vossier, A. Band gap engineering of multi-junction solar cells: Effects of series resistances and solar concentration. *Sci. Rep.* (2017). doi:10.1038/s41598-017-01854-6

18. Dumanli, A. G. & Savin, T. Recent advances in the biomimicry of structural colours. *Chemical Society Reviews* (2016). doi:10.1039/c6cs00129g

19. Zhao, Y. *et al.* Artificial structural color pixels: A review. *Materials* (2017).

doi:10.3390/ma10080944

20. Sun, J., Bhushan, B. & Tong, J. Structural coloration in nature. *RSC Advances* (2013). doi:10.1039/c3ra41096j

21. Joannopoulos, J. D., Johnson, S. G., Winn, J. N. & Meade, R. D. *Photonic crystals: molding the flow of light*. (Princeton university press, 2011).

22. Shao, L., Zhuo, X. & Wang, J. Advanced Plasmonic Materials for Dynamic Color Display. *Advanced Materials* (2018). doi:10.1002/adma.201704338

23. C. Hilsum, "Flat-panel electronic displays: a triumph of physics, chemistry and engineering". Phil. Trans. R. Soc. A. 368, 1027–1082 (2010)

24. http://press.ihs.com/press-release/technology/flat-panel-display-revenues-forecast-fall-2015-ihs-says Accessed: 2/13/16

25. R. Williams, "Domains in liquid crystals". J. Phys. Chem. 39, 382–388 (1963)

26. M. Schadt et al., "Voltage-dependent optical activity of a twisted-nematic liquid crystal". Appl. Phys. Lett. 18, 127–128 (1971)

27. D. Armitage et al., "Introduction to Microdisplays". Chapter 5, John Wiley & Sons, Ltd. (2006)

28. J. S. Steckel et al., "Quantum dots: the ultimate down-conversion material for LCD displays". Journal of the SID 23/07, 294-306 (2015)

29. M. A. Reed et al., "Observation of discrete electronic states in a zero-dimensional semiconductor nanostructure". Phys Rev Lett 60, 535–537 (1988)

30. T. Frecker et al., "Review—Quantum Dots and Their Application in Lighting, Displays, and Biology", ECS Journal of Solid State Science and Technology, 5, R3019-R3031 (2016)

31. S. Ithurria et al., “Quasi 2D colloidal CdSe platelets with thicknesses controlled at the atomic level”. J. Am. Chem. Soc. 130, 16504–16505 (2008)

32. S. Ithurria et al., “Continuous transition from 3D to 1D confinement observed during the formation of CdSe nanoplatelets”. J. Am. Chem. Soc. 133, 3070–3077 (2011)

33. C. She et al., “Low-threshold stimulated emission using colloidal quantum wells”. Nano Lett., 14, 2772–2777 (2014)

34. J. Chen et al., “Quantum-Dot Displays: Giving LCDs a Competitive Edge Through Color”. Information Display, 29, 2-7 (2013)

35. http://www.fujifilmusa.com/products/semiconductor_materials/image-sensor-color-mosaic/rgb/index.html#applications Accessed:2/14/16

36. E. Shum et al., “SIL 2014 sets its sights on SSL evolution in global markets”. LEDs Magazine, 12, 27 (2013)

37. M. Debije et al., “Thirty Years of Luminescent Solar Concentrator Research: Solar Energy for the Built Environment”. Adv. Energy Mater., 2, 12–35 (2012)

38. M. J. Currie et al., “High-Efficiency Organic Solar Concentrators for Photovoltaics”. Science, 321, 226-228 (2008)

39. D. Chemisana, “Building Integrated Concentrating Photovoltaics: A review”. Renew. Sust. Energ. Rev., 15, 603-611 (2011)

40. A. Goetzberger, “Fluorescent solar energy collectors: Operating conditions with diffuse light”. Appl. Phys., 16, 399-404 (1978)

41. M. Carrascosa et al., “Monte Carlo simulation of the performance of PMMA luminescent solar collectors”. Appl. Optics, 22, 3236-3241 (1983)

42. J. S. Batchelder et al., “Luminescent solar concentrators. 1: Theory of operation and techniques for performance evaluation”. Appl. Optics, 18, 3090-3110 (1979)

43. J. C. Goldschmidt et al., “Increasing the efficiency of fluorescent concentrator systems”. Mater. Sol. C., 93, 176-182 (2009)

44. L. H. Slooff et al., “A luminescent solar concentrator with 7.1% power conversion efficiency”. Phys. Status Solidi—R 2, 257-259 (2008)

45. Wilson R. B., “Luminescent Solar Concentrators: A Study of Optical Properties, Re-absorption and Device Optimisation”. Doctoral Dissertation (2010)

46. Hecht, Eugene, Optics, 2nd Ed, Addison Wesley, 1987

47. N. Bronstein et al., “Quantum Dot Luminescent Concentrator Cavity Exhibiting 30-fold Concetration”. ACS Photonics 2, 1576−1583 (2015)

CHAPTER 2

DIFFRACTIVE SPECTRAL-SPLITTING OPTICAL ELEMENT DESIGNED BY ADJOINT-BASED ELECTROMAGNETIC OPTIMIZATION AND FABRICATED BY FEMTOSECOND 3D DIRECT LASER WRITING*

2.1 Introduction and Motivation

Fundamental loss mechanisms set an upper bound on the efficiency of single-junction photovoltaic (PV) cells to 33.5% under one-sun illumination.[1] The most dominant source of loss is the broadband nature of sunlight, as contrasted with the relatively narrow energy range over which a PV cell efficiently converts energy; photons with energy smaller than the bandgap fail to be absorbed, while photons with energy greater than the bandgap lose their excess energy to heat via carrier thermalization. Multi-junction devices have smaller thermalization losses, and thus can more efficiently convert the full energy spectrum of solar radiation. Presently, the highest PV efficiencies are achieved by tandem structures, which use a stack of PV subcells with different bandgaps.[2] However, tandem devices are costly to fabricate, as they generally require epitaxial growth of multiple layers of crystalline semiconductors as well as other processing steps. The tandem structure also imposes constraints on performance and design, as the different PV subcells must be current-matched. The current-matching requirement is of particular importance, as it imposes a strong sensitivity of PV efficiency on the shape of the solar spectrum, which varies with the Sun's position in the sky and with the chemical composition of the atmosphere, both of which will change with the time of day and time of year. As a result, tandem devices have been shown to yield less annual energy production than implied by their high efficiency under the standard AM1.5 spectrum.[3-5]

An alternative multi-junction architecture that decouples spectral filtering from photovoltaic conversion can potentially address these problems. Rather than growing the PV subcells in a vertical stack, they can instead be arranged in a lateral array. Each subcell can be independently grown, reducing cost and relaxing the material choice constraints, and independently connected, eliminating the current-matching constraint. A separate spectral-splitting optical element disperses the wavelengths of the incident sunlight, so that different bands of the solar spectrum are directed to subcells of matching bandgaps. Spectral splitting has previously been implemented with prisms,[6] dichroic mirrors[7] and specular reflection with highly selective interference filters.[8] However, the design freedoms offered by spectral splitting using planar dispersive diffractive optics is particularly attractive for large-area PV applications, in similar fashion to thin dielectric surfaces proposed for light management in PV cells.[9]

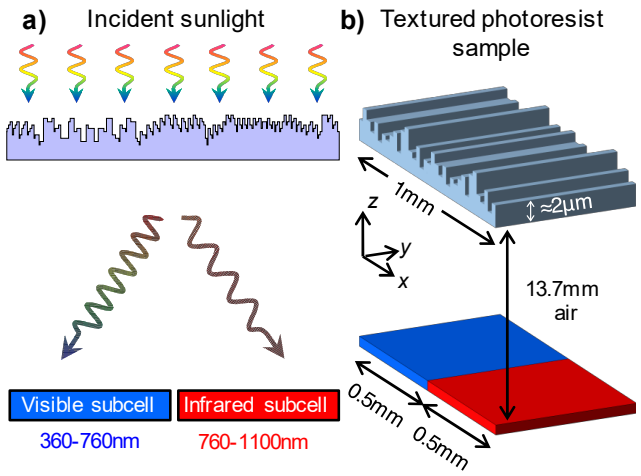

Figure 2.1 a) A thin diffractive phase mask element is designed to laterally split the solar spectrum into two spectral bands and direct each band to separate partitions in the far-field image. b) Diagram of the optical structure designed in this work showing geometric parameters.

Here we demonstrate spectral-splitting using a planar diffractive optical element implemented as a surface texture on a dielectric material, as shown in **Fig. 2.1a**. The surface

texture is composed of flat top "pixels" of 5 μm lateral width, which impart phase shifts to the incident solar wavefront. If the height variation of the pixels is comparable in scale to the solar wavelengths, wavelengths on opposite extremes of the solar spectrum will undergo a significant difference in phase shift. Diffractive optical elements based on this principle have previously been demonstrated to produce different images in the far field when illuminated by different wavelengths of light[10]. The individual pixel heights in our texture are designed such that when the light propagates over a macroscopic distance to the far field, different spectral bands of light are directed to different spatial partitions of the image plane. PV subcells can be placed in these partitions to complete the multi-junction system.

Spectral splitting elements of this type have been previously investigated using a photoresist material and a direct binary search algorithm to optimize the pixel height levels.[11,12] However, heuristic optimization methods require a very large number of simulations of the structure before arriving at an optimal solution. In this work, we present a method that exploits the reciprocity properties underlying Maxwell's equations to quickly obtain the gradient of the objective function with respect to the design variables – in this case, the individual pixel heights. Our approach, which we call the adjoint method, allows the optimization of electromagnetic structures with complex figures of merit at a much smaller computational cost compared to heuristic methods. The number of simulations required per iteration with this optimization approach does not scale with the number of design variables, allowing for the design of much larger or more complex structures without incurring an orders-of-magnitude increase in computational cost (i.e. number of simulations needed).

2.2 Concept

There are many possible ways to optimize an electromagnetic structure. One strategy is to heuristically sample the design space until a solution is found that adequately performs the desired function. These methods are widely applicable and are commonly used.[12-14] However, complicated functionalities call for a complicated structure, which is necessarily described by a large number of design degrees of freedom. In these cases, heuristic methods are computationally cumbersome or infeasible to implement, due to the large number of physical simulations needed to explore a very large design space. Gradient-based optimization algorithms can circumvent this problem by finding a more direct path to a local optimum of the design space. However, a finite-difference calculation of the gradient still requires N simulations for each iteration of the design, one for each of N design variables used to specify the electromagnetic structure.[15] In this section, we show that the adjoint method in electromagnetics can reduce the cost of the gradient calculation to just *two* simulations per iteration – we call these the forward and adjoint simulations, as shown in **Fig. 2.2a**. These methods have been successful in designing electromagnetic structures of various types.[15-19] Similarly to Scranton et. al,[17] we specifically analyze the case of optical diffraction to the far field (distance much greater than a wavelength). A more general treatment of the adjoint method for the optimization of electromagnetic structures can be found in Refs. 15 and 16.

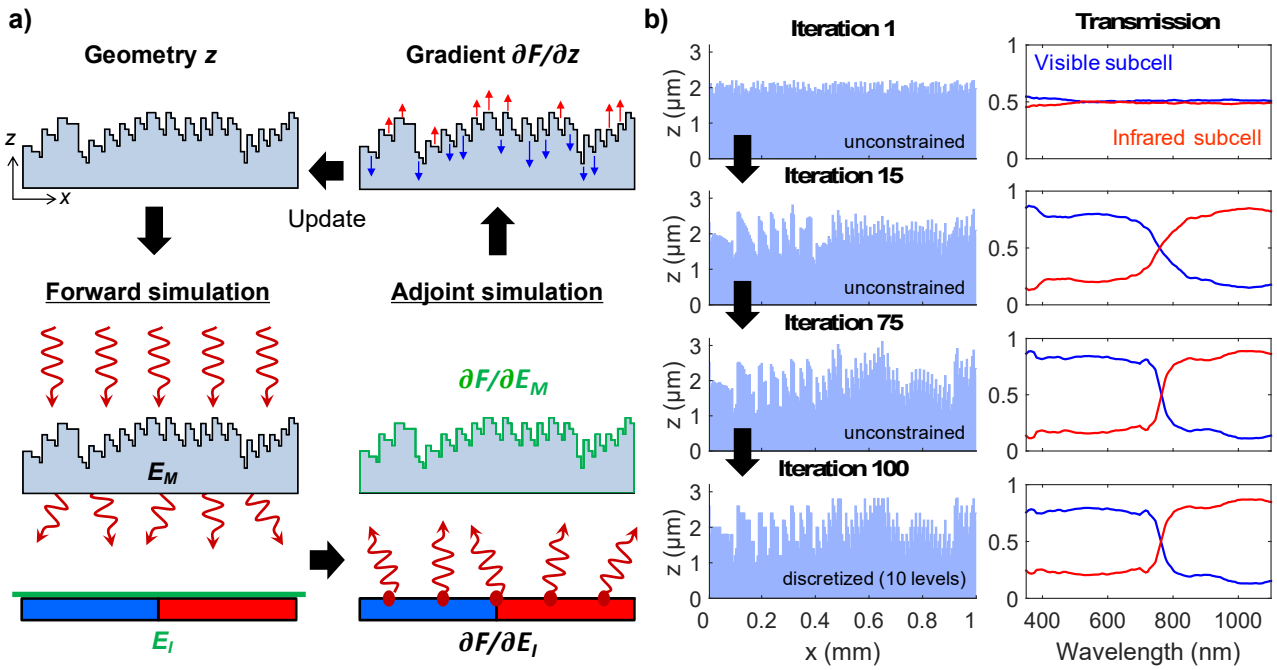

Figure 2.2 a) An iteration of the optimization procedure involves a forward simulation of the structure to retrieve the far-field image and an adjoint simulation to compute the gradient of the figure of merit with respect to the design variables. The gradient is then used to make an iterative change to the structure. b) Sample optimization showing the phase mask texture (left) and transmission coefficient into the visible and infrared image half-planes (right) throughout the optimization. After iteration 75, the height levels were constrained to yield a discretized final design.

We approximate the spectral splitting element as a fully transmitting thin mask that modulates the phase of the incident wavefront. The phase mask is described by a surface texture $z(\overrightarrow{r_M})$ patterned across the mask plane M. The scalar electric field E_M below the mask plane in response to an incident plane wave from air is:

$$E_M(\overrightarrow{r_M}) = \exp\left[i\frac{2\pi}{\lambda}(n(\lambda)-1)z(\overrightarrow{r_M}) + i\Phi(\theta,\phi,k_0)\right] \tag{2.1}$$

where λ is the free-space wavelength, n is the refractive index of the mask material, and $\Phi(\theta, \phi, k_0)$ is the phase associated with a non-normally incident plane wave. At normal incidence, $\Phi = 0$. Equation (1) is an accurate approximation if the mask is optically thin, the angle θ is small, and the lateral size of the design pixels is greater than a wavelength. Although the phase mask's response is calculated using Equation (1) during the optimization to accelerate the design process, the exact electromagnetic response of the final design is evaluated using the finite-difference time-domain (FDTD) solution to Maxwell's equations. For a pixel size of 5μm and wavelengths of 350nm-1100nm used in this work, close agreement is found between Equation (1) and the FDTD method.

We apply Huygens' principle to propagate the mask field E_M to the image plane I, located at a distance $L \gg \lambda$ from the mask. Using the angular spectrum method of propagation,[20] the field E_I at the image plane can be expressed without approximation as a convolution integral:

$$E_I(\vec{r_I}) = \int_M E_M(\vec{r_M}) \cdot h(\vec{r_I} - \vec{r_M})\, d^2\vec{r_M} \tag{2.2}$$

where M denotes the mask plane and $h(\vec{r_I} - \vec{r_M})$ is the Green's function associated with the propagation of an electromagnetic point source along the vector $\vec{r_I} - \vec{r_M}$, which points from the mask to image. The field $E_M(\vec{r_M})$ specifies the complex amplitudes of the point sources, distributed across the bottom surface of the phase mask. The computation of Equation (2) is vastly accelerated by evaluating the convolution integral using Fourier domain methods. Once E_I is obtained, the figure of merit F of the structure is found by evaluating a local objective function f across the image:

$$F = \int_I f[E_I(\vec{r_I})]\ d^2\vec{r_I} \tag{2.3}$$

For spectral splitting, a simple choice for f is the optical intensity $|E_I(\overrightarrow{r_I})|^2$ weighted by a binary function (either 0 or 1) at each position $\overrightarrow{r_I}$ that defines the desired region of the image plane for a given wavelength.

The derivative of the figure of merit with respect to the design variables $z(\overrightarrow{r_M})$ is found by applying the chain rule:

$$\frac{\partial F}{\partial z(\overrightarrow{r_M})} = \mathrm{Re}\left(\frac{\partial F}{\partial E_M(\overrightarrow{r_M})} \cdot \frac{\partial E_M(\overrightarrow{r_M})}{\partial z(\overrightarrow{r_M})}\right) \tag{2.4}$$

Although the fields are complex, only the real part of the gradient is relevant since both F and z are real. The second term on the right side can be found easily using Equation (1). The first term is expressed by differentiating Equation (3), again applying the chain rule. The result is:

$$\frac{\partial F}{\partial E_M(\overrightarrow{r_M})} = \int_I \frac{\partial f}{\partial E_I(\overrightarrow{r_I})} \cdot h(\overrightarrow{r_M} - \overrightarrow{r_I})\, d^2\overrightarrow{r_I} \tag{2.5}$$

Here, we have invoked the well-known reciprocity of electromagnetic Green's functions, which expresses the principle that any optical path between two points is identical in either direction, a property of Maxwell's equations first recognized by Poynting[21] and Lorentz.[22] This implies that the same Green's function h can be used to propagate an electric field in both the forward direction (mask to image, $\overrightarrow{r_I} - \overrightarrow{r_M}$) and the reverse direction (image to mask, $\overrightarrow{r_M} - \overrightarrow{r_I}$):

$$h(\overrightarrow{r_I} - \overrightarrow{r_M}) = h(\overrightarrow{r_M} - \overrightarrow{r_I}) \tag{2.6}$$

This equivalence can also be seen directly from the expression for the propagation Green's function h in diffractive optics.[20]

Equation (5) is completely analogous to Equation (2), except that the propagation is from the image to the mask, and the point sources are defined on the *image* plane with complex amplitudes $\partial f / \partial E_I(\overrightarrow{r_I})$. We thus have the result that the calculation of the gradient on the left side of Equation (5) can be reduced to a single physical simulation from the image to the mask.

We call this the *adjoint* simulation, so named because this method is an instance of the more general adjoint (or dual) method in linear algebra.[15,16] The adjoint simulation provides the gradient of F with respect to *all* N variables, regardless of the size of N. This key advantage makes our gradient-based approach highly scalable, allowing for efficient optimization of structures with a large number of design variables. Additionally, an arbitrarily complex function f can be chosen as the optimization figure of merit, provided that the expression for f can be differentiated to obtain the complex amplitudes $\partial f / \partial E_I(\overrightarrow{r_I})$ in the adjoint simulation.

Since sunlight is an incoherent source, a complete forward simulation requires evaluating Equations (1) and (2) once separately for each wavelength or incidence angle for which the mask is to be designed. The figure of merit in Equation (3) is then evaluated for each input wavefront (unique wavelength and incidence angle), and the total electromagnetic figure of merit is obtained by summing over all of the input wavefronts: $F = \sum_i F_i$. Likewise, the complete adjoint simulation requires Equations (4) and (5) to be evaluated once for each input wavefront, and the gradients are summed: $\partial F / \partial z = \sum_i (\partial F_i / \partial z)$. Schemes other than a sum can also be used to obtain F that emphasize, for instance, the worst-performing input wavefront. In these cases, the expression for F must be carefully differentiated to obtain the total gradient. These schemes were not used to produce the final design in this work.

In practice, the pixel heights $z(\overrightarrow{r_M})$ in the spectral-splitting texture cannot be adjusted with infinite precision. With the fabrication capabilities available to produce such an element, a multi-level structure is more realistic, in which all of the pixel heights $z(\overrightarrow{r_M})$ in the design are selected from a small number of discrete height levels with constant spacing. Rather than explicitly discretizing the pixel heights in the optimization, we continue to treat $z(\overrightarrow{r_M})$ as a continuous variable and include an additional term in the figure of merit expression to penalize F

if the height $z(\overrightarrow{r_M})$ does not belong to a set of allowed height values. This step requires no new simulations. The relative weights of the electromagnetic merit function and the constraint function can be adjusted so that neither value suffers significantly during the constrained optimization (see Supporting Information for more details).

Once the gradient $\partial F / \partial z$ is known, various algorithms are available to find the optimal update to the geometry Δz. In this work, we use the steepest descent algorithm, which gives an update Δz that is proportional to the gradient. The constant of proportionality, or optimization step size, is found using a line search algorithm.[23] After the update is made, the forward and adjoint simulations are performed on the new geometry to calculate the next update. This iterative process is continued until a convergence condition is met. If sufficient memory is available for the computation, the geometry update can also be calculated from the gradient information using a quasi-Newton method to obtain faster convergence.[23] This was not implemented to produce the main optimization result in this work.

2.3. Methods

Sample fabrication: A glass slide was used as a substrate. The sample is fabricated by a direct laser writing system (Photonic Professional GT, Nanoscribe, Eggenstein-Leopoldshafen, Germany) using IP-Dip photoresist from Nanoscribe. The design was fabricated by using a dip-in technology. The final structure consists of numerous fields stitched next to each other. Each field has a size of 150 x 150 µm² and is fabricated layer-by-layer. The layers are separated by 400 nm. In each layer the scan lines are separated by 250 nm. The horizontal movement is carried out by laterally scanning the laser focus by galvanometric mirrors, whereas the vertical movement is carried out by piezo actuators. Each line is written with a scan speed of 50 mm/s.

Characterization setup: The schematic of the setup is shown in **Figure 2.4c**. For the light source, fiber coupled tungsten halogen lamp with wavelength range of 360 to 2400 nm was used (HL-2000, Ocean Optics, Dunedin, FL). The light passes through a 75 mm focal length achromatic lens (49-538, Edmund Optics, Barrington, NJ), reflects off of a silver mirror and finally passes through an in-house fabricated aperture matching the sample size. The transmitted light is collected with a fiber (NA of 0.22 which yields an acceptance angle of 12.7° in air) coupled Si photodiode array spectrometer (USB2000+, Ocean Optics, Dunedin, FL) that covers the 380 to 970 nm wavelength range. Ten scans were used to improve signal-to-noise ratio. Background noise was subtracted within the manufacturer's software.

Instrument: Height values of the sample were determined by a dual confocal laser scanning microscope (OLS4100, Olympus, Waltham, MA) using a 50x objective.

2.4 Results

Fig. 2.1b shows the geometric parameters chosen for the spectral splitting element designed in this work. The surface texture of the thin film is discretized to ten equally spaced height levels spanning a range of 1.8μm in steps of 0.2μm. The texture's height is modulated along x with a pixel width of 5.0μm, so that one period of the design contains 200 pixels over a total length of 1.0mm. The height is constant in the y direction. In our experiment, the light propagates through an air gap after passing through the thin photoresist film. Alternatively, the texture can also be patterned on the top surface of an optically thick dielectric or polymer slab that rests directly on top of the photovoltaic cells.

The design was optimized for 127 wavelengths over the range of 360nm to 1100nm, which contains about 82% of the power in the AM1.5G solar spectrum.[24] Wavelengths shorter than the chosen cutoff of 760nm (roughly corresponding to the band of visible light) were directed to one half-plane of the image plane as shown in **Fig. 1a**, and wavelengths longer than 760nm (near-infrared light) were directed to the other half-plane. We henceforth refer to these half-planes as the visible and infrared subcells, respectively, following the placement of the PV subcells in the image plane shown in **Fig. 1a**. The structure in this work was optimized for normal incidence only. As our figure of merit, we define the design's spectral splitting efficiency to be:

$$\textit{Spectral splitting efficiency} = \frac{1}{N_\lambda}\sum_i \left[T_{\text{vis}}(\lambda_i) \times (\lambda_i \leq 760\text{nm}) + T_{\text{IR}}(\lambda_i) \times (\lambda_i > 760\text{nm})\right] \quad (2.7)$$

where N_λ is the number of wavelengths sampled for the figure of merit calculation, T_{vis} is the transmission coefficient through the visible subcell, and T_{IR} is the transmission coefficient through the infrared subcell. The optimal solution should transmit nearly all of the incident visible light (λ<760nm) to the visible subcell, and nearly all of the incident infrared light (λ>760nm) to the infrared subcell, with a sharp transition between the subcells near the cutoff of λ=760nm. In keeping with the goal of large-area photovoltaic power conversion, the structure was optimized assuming periodic boundary conditions along *x* and extended infinitely along *y*.

The optimization was performed in two phases. Starting from a randomly generated texture, an unconstrained optimization was first performed to obtain a high spectral splitting efficiency. Next, we impose the discretization constraint to yield a structure with ten discrete height levels. The first phase of the optimization was run for 75 iterations, and the second phase was run for 25 iterations, for a total of 200 physical simulations through the entire design process using the adjoint method. Both the simulation and optimization steps were written using

MATLAB scripts, and the design process took less than 2 minutes on a single machine using two 3.2GHz processors.

The optical performance at several points during the optimization process is shown in Fig. 2b for a representative design. The optimization algorithm requires only a few iterations to reach a design that efficiently splits the wavelengths to the desired cells, as shown by the performance at iteration 15, then continues to refine the design as it approaches the local optimum at iteration 75. Due to the relatively large size of our 200-dimensional design space, many high-performing local optima exist even when the design is constrained. Therefore, the splitting efficiency does not substantially deteriorate during the constrained optimization step to produce a ten-level structure (iterations 76 to 100).

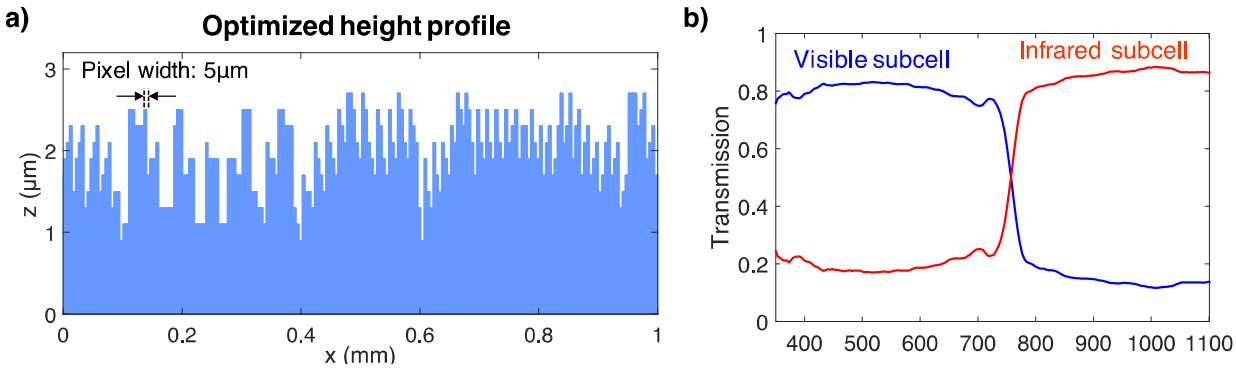

Figure 2.3 a) Height profile for the final result of the computational optimization. b) Simulated spectral response of the optimized design. c) Height profile of one period of the fabricated sample, measured using confocal microscopy. d) Simulated (dotted) and experimentally measured (solid) spectral performance of the fabricated structure.

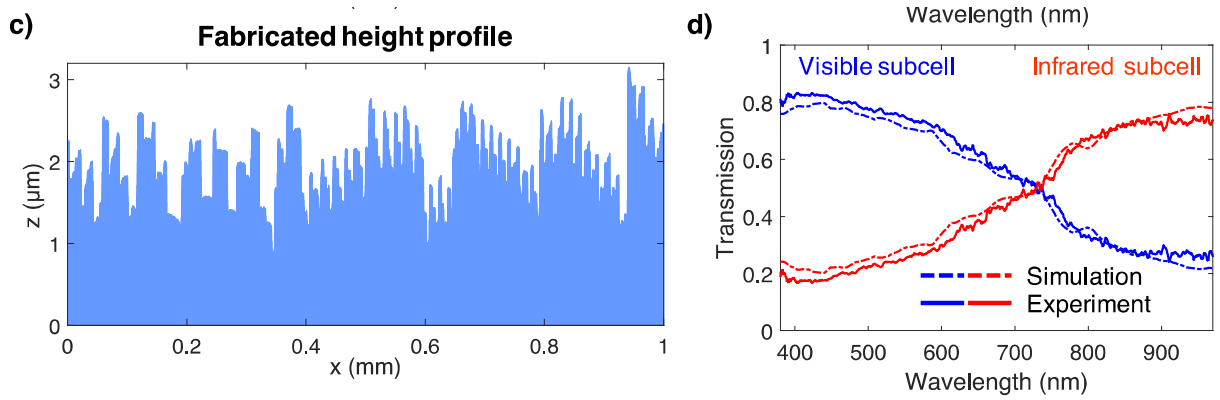

Figure 2.3 (cont.)

The optimal mask texture found using the adjoint method is shown in **Fig. 2.3a**. To evaluate the spectral splitting efficiency of this design, the near-field response of the structure is evaluated using FDTD methods, and the calculated fields are propagated to the far field using scalar diffraction methods. To enable comparison of the optimized structure with experimental results, periodic boundary conditions were not assumed during the propagation step. For a feature size of 5μm and a distance of 13.7mm, about ~87% of the optical power transmitted through one phase mask period is diffracted into its own image plane (directly underneath) or to the image planes of its two nearest neighbors along *x*. Therefore, to approximately replicate the periodic boundary conditions in the experiment, it is sufficient to produce a system with three repeated 1mm phase masks and measure the response at the image plane directly beneath the central period. This situation was simulated in the propagation step, with the transmission coefficients in Equation (7) normalized to the power on the central image plane. Since a small amount of the incident light is diffracted to large angles beyond the nearest-neighbor image planes, this calculated efficiency will slightly overestimate the spectral splitting efficiency of a true infinitely periodic system.

Under these considerations, the spectral response of the final design is shown in **Fig. 2.3b**, predicting a spectral splitting efficiency of 81.5% over the full design range of 360-1100nm. The efficiency of this design over the spectral range of our characterization instruments (380-970nm) is 80.4%. We also note that the spectral splitting efficiency predicted using Equation (1) for the near-field response deviates from the result of the FDTD simulation by <1% (absolute difference), validating the accuracy of the thin mask approximation used to accelerate the optimization process.

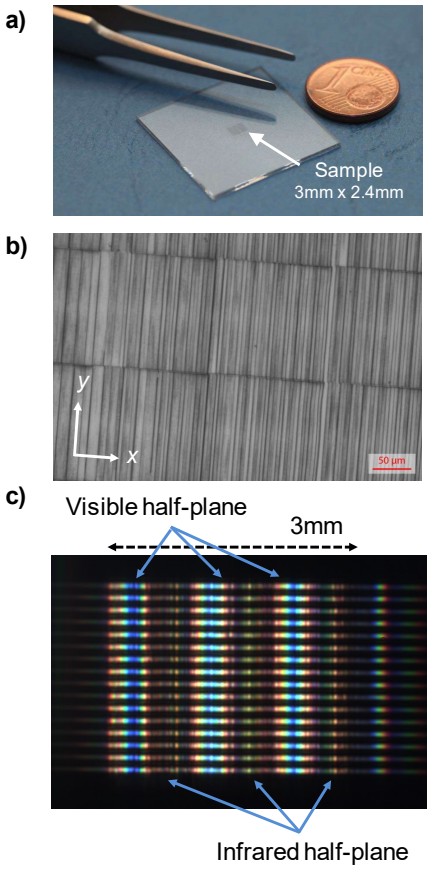

Figure 2.4 a) Photograph of the fabricated phase mask sample. b) Scanning electron microscopy (SEM) image of a portion of the sample, showing 5µm strips of constant height. Deep black lines mark the separation between stitched areas. c) Visible CMOS image of the sample's far field, showing lateral splitting of the spectrum from three periods of the phase mask texture.

A sample (Fig. 2.4a) containing three periods of the phase mask specified in Fig. 2.3a was fabricated using femtosecond 3D direct laser writing with IP-Dip photoresist. The laser writing system produces the textured photoresist sample in a single three-dimensional scan without requiring multiple masks or alignment steps, and achieves submicron structural resolution by exciting nonlinear optical processes in the photoresist material.[25] We note that multi-photon laser writing remains a viable fabrication option even for submicron lateral pixel dimensions should such pixels be required for future spectral-splitting designs. The total area of the fabricated sample is 3 mm (x) × 2.4 mm (y), formed by stitching together individually written regions that have a length of 0.15mm along y (see stitching lines in Fig. 2.4b). The height profile of the central period, measured using confocal microscopy, is shown in Fig. 2.3c. Although many of the important features of the optimized height profile are reproduced, the tops of individual pixels in the fabricated sample are not completely flat, and both pixel heights and widths exhibited some deviations from the design values.

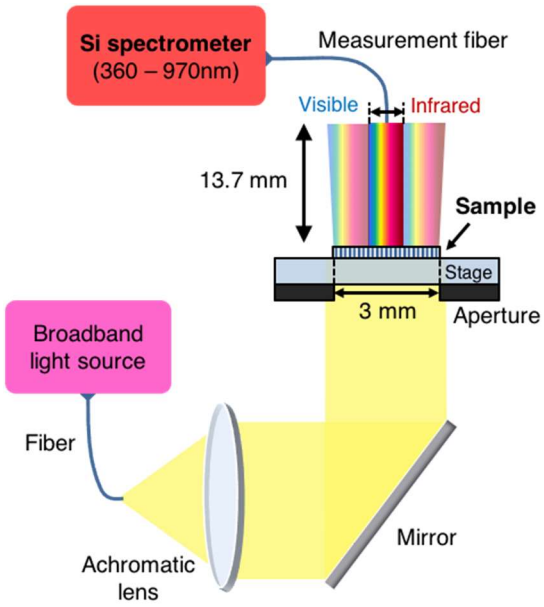

Figure 2.5 Schematic of the optical characterization experiment.

The optical response of the phase mask was characterized using the setup shown in **Fig.2.5**. A broadband light source was collimated using an achromatic lens to reproduce the normal incidence beam assumed during the optimization. To uniformly illuminate only the area of the phase mask, an aperture of the same dimensions as the sample was placed above the sample to define the incident beam. Visual inspection of the image plane reveals that spectral splitting is taking place. **Fig. 2.4c** shows the image plane (under the full three periods of the sample) captured by a color CMOS camera with a built-in infrared filter. Much of the transmitted visible light is split to one half of the image, with some undesired visible light arriving on the infrared side.

The spectral splitting efficiency was measured by scanning a measurement fiber across the image below the central period of the sample (along the *x* direction). The fiber tip has a diameter of 50μm, and accordingly the output light was collected at 50μm steps of the fiber tip position and passed through the fiber into a photodiode array spectrometer. **Figure 2.3d** plots the result of the observed and simulated performance of the fabricated texture in **Figure 2.3c**, over the operational range of the spectrometer (380-970nm). The measured splitting efficiency of the fabricated sample over this spectral range is 69.5%. The simulation methodology is the same as that used to produce **Fig. 2.3b**, but now also accounts for the circular shape and discrete positions of the measurement fiber (this addition affects the splitting efficiency by <1%). The simulated and experimental results show close agreement; averaged over 380-970nm, the absolute difference in transmission into the desired cell is ±3.1% between the simulation and experiment. Relative to the optimized design in **Figure 2.3b**, over the same range the observed spectral splitting efficiency is reduced by 10.9%. The efficiency drop is manifested mostly in the reduced sharpness of the splitting transition from the visible cell to the infrared cell, while the

peak splitting ratios on the two sides of the splitting transition are not significantly degraded. The agreement of the simulation and experiment in **Fig. 2.3d** suggests that fabrication errors are mainly responsible for the degraded performance.

Equation 2.1 predicts that the phase response of the sample is polarization-independent, which rests on the assumption that the texture is locally flat to the incident light. When this holds, the structure's response to the different vector components of the electric field are not coupled.[20] In evaluating **Equation 2.1**, this condition is satisfied by assuming a pixel width that is several times larger than the wavelength. FDTD simulations of the fabricated structure in response to light polarized along and orthogonal to the design direction (x) show less than a 0.1% absolute difference in spectral splitting efficiency (under normal incidence, 380-970nm). Experimental results also show insensitivity to incident polarization. The sample's spectral response in **Fig. 2.3d** was characterized using a broadband, unpolarized light source. Separate measurements that filter one of the two polarizations show that the sample's spectral splitting efficiency under either polarization differs from the case of unpolarized light by no more than 0.33% (see Supporting Information). Since sunlight is also unpolarized, this lack of polarization sensitivity is advantageous for solar energy harvesting.

Neither the simulated nor measured spectral splitting efficiency accounts for light that is lost while traveling through the system. FDTD simulations of the fabricated structure in **Fig. 2.3c** predict the transmittance through the phase mask to be 91.4%, averaged over the two polarizations and weighted by the power spectrum of the light source. This loss can be explained by Fresnel reflections from the two air-photoresist interfaces in the sample. Experimentally, the transmittance through the sample is found to be 89.5%, by comparing the power before the sample surface and at the image plane. The deviation between simulation and experiment is

within the measurement uncertainty of the power sensors.[26] As would be required for a high-efficiency PV system, the reflection losses may be reduced by replacing the air gap with a dielectric layer index-matched to the phase mask, eliminating one of the two reflective interfaces, as well as the use of an anti-reflection coating on the top surface of the phase mask.

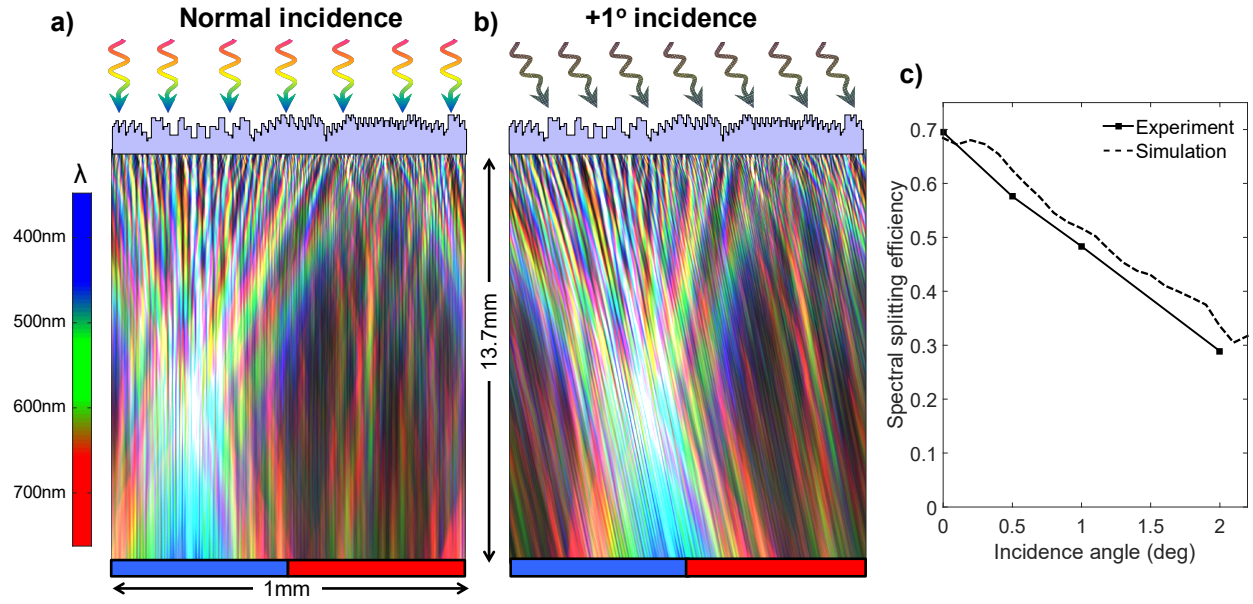

Figure 2.6 a) Colored profile of the simulated optical intensity between the sample and the image plane, under visible light (360nm to 760nm) at normal incidence. The color at a point in space denotes the wavelengths with large relative flux density in that region, following the color scheme on the left. (Wavelengths corresponding to different colors are added using their RGB color values.) b) Intensity profile under collimated illumination from +1° polar angle. c) Spectral splitting efficiency vs. incidence angle, averaged from 380nm to 970nm.

Under solar irradiation, an important additional consideration is the angle of the incident light. Although the collimated light in our experiment has negligible angular spread, the Sun subtends an angle of $\Delta\theta = \pm 0.27^{\circ}$ in the sky, and terrestrial solar radiation has a large diffuse component due to atmospheric scattering.[27] **Fig. 2.6a** and **Fig. 2.6b** illustrate the simulated

optical intensity profile of the fabricated diffractive element under normal incidence and under collimated light at θ =+1° from normal, respectively (the incident wavefronts have no *k*-vector component along the *y*-axis). For clarity, only the photons in the visible band from 360nm to 760nm are included, and the color of the profile indicates the wavelengths that have the greatest flux in a given region of space. At normal incidence, the diffractive element concentrates most of the visible light into the correct cell, with the shorter wavelengths (blue) focused onto the middle of the cell while the longer wavelengths (red) closer to the cutoff of 760nm lie at the boundary between the two cells. At θ =+1°, all of the diffracted wavefronts undergo a shift in angle, so that the entire field at the image plane undergoes a lateral shift. This causes some of the visible light to leak into the infrared cell, starting with the wavelengths near the cutoff.

The spectral splitting efficiency of the fabricated sample is shown in **Fig. 2.6c** for several values of the incidence angle. Due to the predictable shift in the image with changing θ, the portion of the solar spectrum received by the two cells dramatically changes with incidence angle. With large enough θ, the two spectral bands will almost fully illuminate the wrong cell. Since the image must shift by half a period for this reversal to occur, this reversal angle is determined by half the geometric aspect ratio (lateral period to vertical height) of the device: $\theta_{rev} = \tan^{-1}(0.5\text{mm}/13.7\text{mm}) = 2.1°$. Indeed, the measured spectral splitting efficiency at $\theta = 2°$ is found to be approximately 28.9%, which is close to 100% minus the efficiency at normal incidence. At an angle of $\theta_{rev}/2$, roughly half of each spectral band should illuminate the correct cell, so that the spectral splitting efficiency should be ~50%. This is also seen in the experiment, where the spectral splitting efficiency at $\theta = 1°$ is 48.4%. Since a splitting efficiency of 50% is equivalent to no splitting, the angular acceptance of the structure is limited to $\approx \pm 1°$. The angular response of the sample is thus robust enough to split direct sunlight with little loss in efficiency

(see Supporting Information), but the diffuse radiation is randomly dispersed between the cells. We have considered here only light with no *k*-vector along the *y*-axis; since there are no variations in both the sample and image plane along the *y* direction, the efficiency has no significant dependence on angular shifts along this dimension.

Further optimization of the design can improve the efficiency of the structure in **Fig. 2.3b**. For the same sample size of 1mm, a reduction in pixel size can increase the efficiency by adding more degrees of freedom to the structure, while allowing the diffracted light to bend at sharper angles. By increasing the geometric aspect ratio, the angular acceptance can also be increased (see Supporting Information). However, a pixel size reduction does not fundamentally change the image-shifting angular response of the diffractive element, and the pixel size cannot be reduced indefinitely without fundamentally changing the physics of the dielectric structure so that it no longer operates by diffraction. For instance, when the pixel size is smaller than a wavelength, resonances can be excited in the device,[9,28] and entirely new design strategies will be needed. Therefore, simply scaling the device in this direction cannot yield a substantial improvement in the angular acceptance.

Reductions in the pixel size still have the potential to improve the spectral splitting efficiency under direct sunlight, and increasing the pixel aspect ratio allows the photovoltaic system to be made more compact. Furthermore, the ability of more tightly packed pixels to diffract light at sharper angles dramatically improves the efficiency of splitting incident light to three or more PV cells with different bandgaps. To allow for these design improvements, the fabrication process must be improved to faithfully reproduce the optimized multi-level structure while allowing for better lateral and vertical resolution. Alternative fabrication methods can also be considered as the structure is scaled for large-area photovoltaics. Nanoimprint lithography[29] is

an appealing option that has also been proposed for the fabrication of dielectric nanostructures on PV cells for light management.[9] With this method, a hard mask of the design (made using direct laser writing or electron-beam lithography) may potentially be patterned over many dielectric or polymer surfaces at high throughput. We do note that the adjoint method is fully compatible with three or more PV cells and diffractive designs based on smaller pixels.

2.5 Applying the discretization constraint

Although the pixel heights $z(\overrightarrow{r_M})$ in the spectral-splitting surface texture are continuously adjusted by the optimization routine, in practice these values cannot be specified with infinite precision. With the direct laser writing process used in this work, a multi-level structure is more realistic, where all the pixel heights $z(\overrightarrow{r_M})$ in the design are selected from H discrete height levels with constant spacing z_{step}. The set of possible pixel heights is $\{z_j = z_{min} + j \cdot z_{step}, j \in [0, H-1]\}$. Rather than explicitly discretizing z in the optimization, we can continue to treat z as a continuous variable and introduce the discretization requirement as a constraint in the figure of merit expression. The figure of merit expression is hence modified to:

$$F = F_{elec} + \beta \int_M \cos\left[\frac{2\pi}{z_{step}}\left(z(\overrightarrow{r_M}) - z_{min}\right)\right] d^2\overrightarrow{r_M}, \tag{2.8}$$

where F_{elec} is the electromagnetic (spectral-splitting) figure of merit given by **Equation 2.3** in the manuscript, and the second term on the right is F_{cons}, the constraint figure of merit. β is the strength of the discretization constraint relative to F_{elec}. The local constraint function is differentiable and has maxima where $z(\overrightarrow{r_M})$ belongs to the set $\{z_j\}$. Additional terms in F_{cons} (not shown) ensure that $z(\overrightarrow{r_M})$ falls inside the desired range $[z_{min}, z_{min} + H \cdot z_{step}]$. To obtain the gradient

of the constraint, we simply differentiate the second term in **Equation 2.8**. Since the constraint function is taken over the variables in the mask, this step requires no new simulations.

2.6 Smaller pixels yield larger diffraction angles

As a direct result of Huygens ' Principle, it is well known that an object of smaller size is able to diffract light to larger angles than objects of larger size. This is true as long as the size of the object is at least several times larger than a wavelength. The diffraction angle as a function of feature size can be quantified by examining the case a circular aperture with diameter D, representative of a single pixel in a more complex diffractive element. The far-field pattern of the circular aperture is a rotationally symmetric Airy disk. The intensity profile of the Airy disk directly gives the diffracted power as a function of diffraction angle from a pixel:[30]

$$I(\lambda, D, \theta_D) \propto \left[2 \cdot \frac{J_1(\pi(D/\lambda)\sin\theta_D)}{\pi(D/\lambda)\sin\theta_D}\right]^2 . \tag{2.9}$$

Here, θ_D is the diffraction angle and J_1 is the Bessel function of the first kind. The prefactor to I is proportional to the area of the aperture. **Fig. 2.7** plots **Equation 2.9** for four values of the feature size D and two relevant wavelengths. Each curve is normalized to the intensity at the center of its Airy disk ($\theta_D = 0^o$). The angular distribution of the diffracted light $I(\theta_D)$ is a function of the ratio D/λ, so that longer wavelengths are diffracted to larger angles than the shorter wavelengths. However, when the feature size is close to the wavelength, the pixels in a phase mask no longer behave as a diffractive object, so the model cannot be extended to pixel sizes below ~1 μm for the wavelengths of interest.

The choice of the structure's geometric aspect ratio (lateral period divided by vertical distance) imposes a diffraction angle requirement, since some of the light incident on the edges

of one period must be diffracted to the opposite side on the image plane. This implicit diffraction angle requirement should not exceed the maximum diffraction angle that can be provided by the pixels of the phase mask. Since the shorter wavelengths are diffracted to smaller angles, the aspect ratio must be compatible with the maximum diffraction angle of the shortest wavelengths near 400nm.

From the aspect ratio of our periodic structure, we can deduce that the maximum required diffraction angle is 0.5mm/13.7mm = 2.1°. From **Fig. 2.7**, we observe that a single pixel with a size of 5μm diffracts a significant amount of power to an angle of 2.1° (~58% of the power at normal) at a wavelength of 400nm. Therefore, the pixel size chosen for the design is compatible with the geometric aspect ratio of the structure to yield a high spectral splitting ratio. Nonetheless, performance can be further improved by scaling the pixel size, without going below a wavelength, and thereby extending the accessible range of diffraction angles.

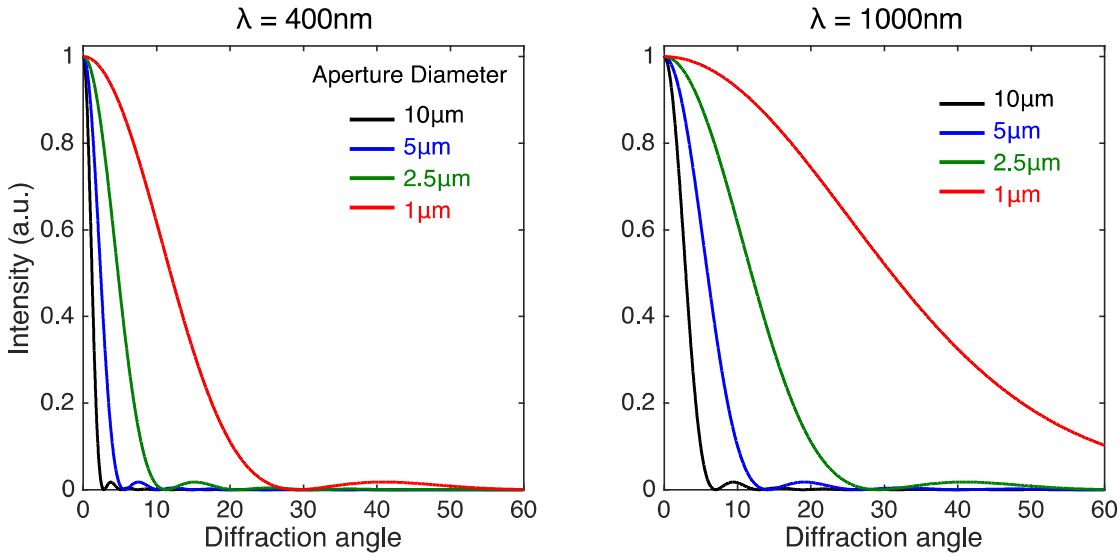

Figure 2.7 Normalized optical intensity vs. diffracted angle for a circular aperture of several sizes and two wavelengths. The diameter of the circular aperture can be compared to the pixel size in a more complex diffractive element.

2.7 Characterization Setup

The optical setup used for the sample characterization (schematically illustrated in **Fig. 2.5** above) was built on a laser table, as shown in **Fig. 2.8**. The incident light leaves from an optical fiber that is coupled to a tungsten halogen lamp (not shown) and stabilized by a fiber holder on a translation stage. The light is then collimated by an achromatic lens and the beam is directed to the sample stage by a silver mirror.

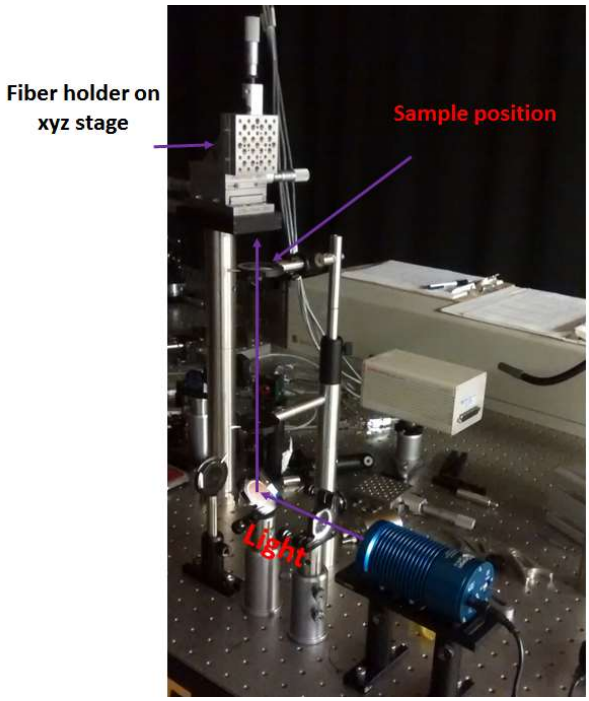

Figure 2.8 Photo of the optical setup used for sample characterization.

2.8 Polarization Sensitivity

The phase mask was designed under the assumption that its phase response is polarization-independent. This relies on the condition that the texture is locally flat to the incident light, so that the sample's response to the different vector components of the electromagnetic fields do not become coupled.[30] In simulations, this is satisfied by using a pixel width that is several times larger than the wavelength. The broadband light source used in the

experimental characterization is unpolarized, similar to the real solar spectrum. To analyze the phase mask's sensitivity to incident light polarization, the sample was also characterized under linearly polarized light by placing a linear polarizer in the path of the light beam before the sample stage. The polarizer orientations were chosen to polarize the incident beam parallel and orthogonal to the direction of height modulation in the sample. Since the texturing is along x, these correspond to the cases of E_x=0 and E_y=0, respectively.

The results of the measurements are shown in **Fig. 2.9**. Relative to the results for unpolarized incident light (**Fig. 2.9a**), the wavelength-averaged deviation in the spectral splitting efficiency (defined in **Equation 2.7**) is 0.32% for light polarized along the grating (**Fig. 2.9b**), and 0.33% for light polarized orthogonal to the gating (**Fig. 2.9c**). The sample's response has negligible dependence on polarization. This suggests that the optical response of the phase shifting elements is not sensitive to the small amount of surface roughness within each pixel, validating the assumption made in **Equation 2.1**. This lack of polarization sensitivity is advantageous for solar energy harvesting.

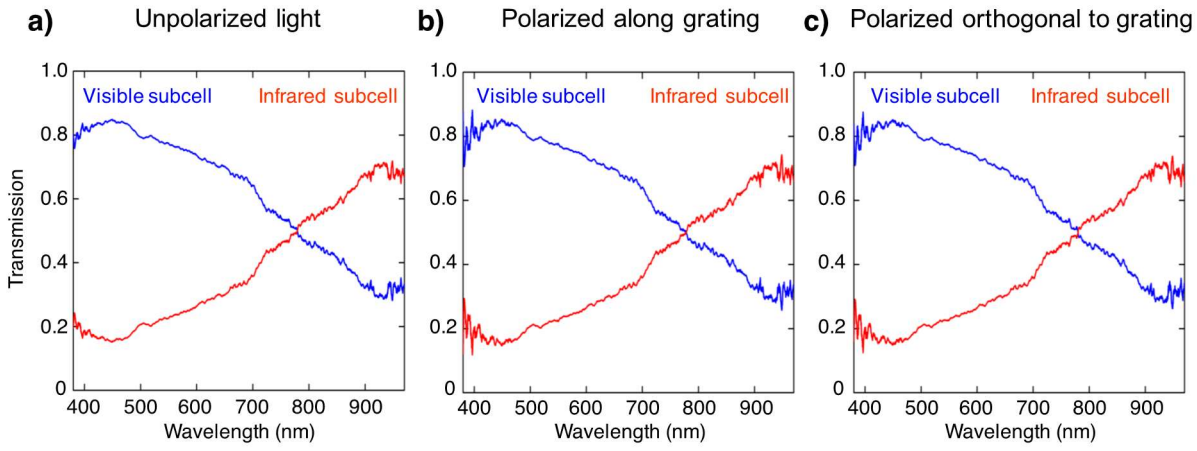

Figure 2.9 Measured spectral splitting response of the fabricated sample under incident light that is a) unpolarized, b) polarized along to the grating, c) polarized orthogonal to the grating.

2.9 Response to Non-Collimated Light

Sunlight is not collimated and is spatially incoherent. The simulated spectral response of the fabricated diffractive element under non-collimated illumination is shown for several values of angular spread in **Fig. 2.10**. For these results, a finite number of incidence angles were sampled over the half-angle $\Delta\theta$, and for each incidence angle a separate set of simulations (over the 380-970nm wavelength range) was run using collimated light. The incident power was assumed to be equal for all angles in the cone spanning $\Delta\theta$, which is accurate for a Lambertian distribution at small angles. Only incidence angles with no *k*-vector along *y* were considered, since the image plane does not change with *y*. We then add the optical *intensity* at the image plane for all of the incidence angles to obtain the final image. This last step is equivalent to an incoherent addition of the contributions from each incidence angle, and accounts for the spatial incoherence of sunlight.

The simulated spectral splitting efficiency of the fabricated sample under normal incidence is 68.3% (less than the experimentally measured value of 69.5%). The angle subtended by the Sun in the sky is about 0.54º, corresponding to a half-angle of $\Delta\theta = \pm 0.27^{\circ}$. The simulated spectral splitting efficiency under the angular cone corresponding to direct sunlight is 65.7%, which is a relatively small degradation from perfect normal incidence. The spectral splitting performance continues to fall for larger values of $\Delta\theta$, similar to the trend of decreasing efficiency with the incidence angle of collimated light shown in **Fig. 2.6c**. However, for the same decrease in efficiency, the required value of $\Delta\theta$ is twice as large as that of the collimated incidence angle θ. This is because the response under an angular spread of $\Delta\theta$ contains contributions from all of the angles inside the cone, including the comparatively high-performing angles near normal. Notably, the spectral splitting efficiency is very close to 50% for $\Delta\theta = \pm 2^{\circ}$, even though the

efficiency falls to 50% at $\theta = 1^{o}$ in the collimated case. This is because this continuous range includes all the angles between normal incidence, where the efficiency is maximum, and the reversal angle $\theta_{rev} = 2^{o}$, where the efficiency is minimum.

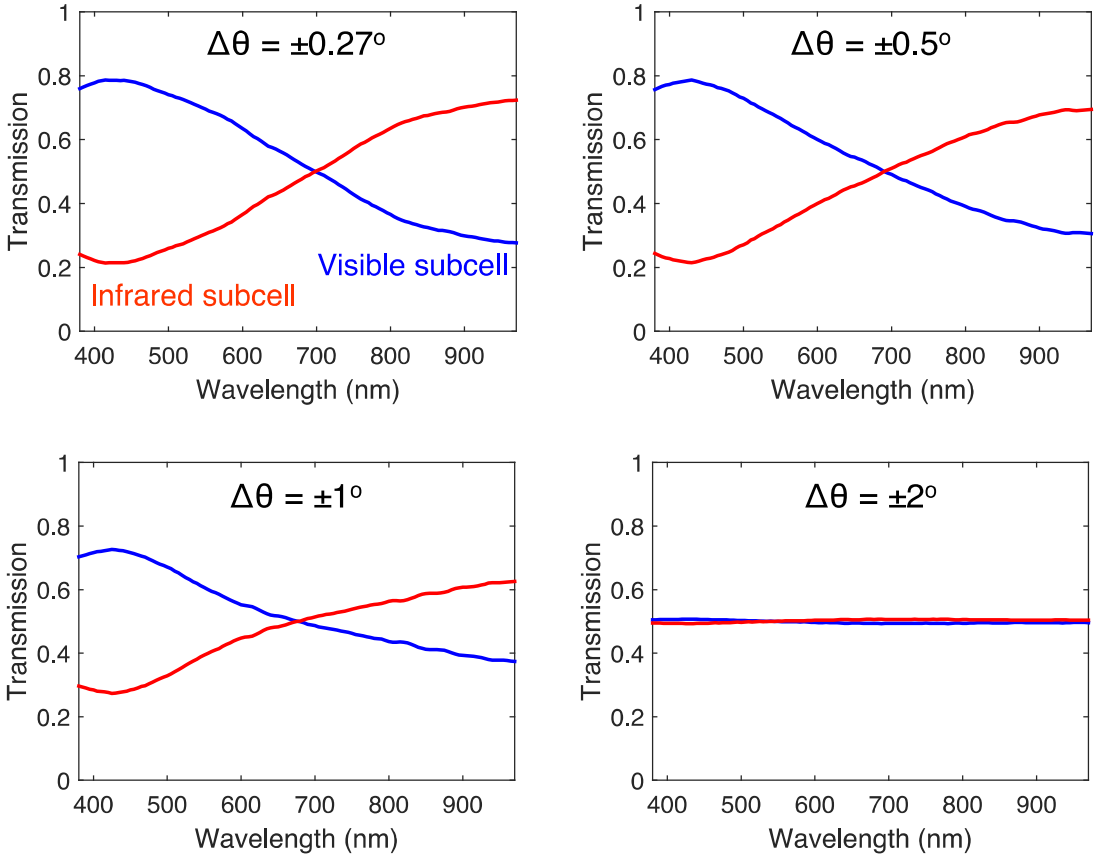

Figure 2.10 Simulated spectral splitting efficiency of the fabricated sample (**Fig. 2.3c**) when illuminated by a continuous distribution of incidence angles spanning a half-angle of $\Delta\theta$ from a spatially incoherent source.

2.10 Photovoltaic Efficiency Calculation under Direct Sunlight

To evaluate the effectiveness of our spectral-splitting phase mask for solar energy applications, we use detailed-balance methods[1] to calculate the photovoltaic efficiency of the two-junction system. We consider the spectral splitting system illustrated in **Fig. 2.1a** with two subcells, under

direct (near-normal) solar illumination with the standard AM1.5D spectrum. For the i^{th} subcell with bandgap $E_{g,i}$, we express the current J_i through the cell using the diode equation assuming negligible series resistance:

$$J_i = J_{sc,i} - J_{0,i} e^{qV_i/kT} , \tag{2.10}$$

where $J_{sc,i}$ is the short-circuit current of the cell under illumination, $J_{0,i}$ is the dark current, V_i is the voltage on the cell, T is the cell temperature, q is the electron charge, and k is the Boltzmann constant. The short-circuit current comes directly from the incident illumination on the subcell and is given by:

$$J_{sc,i} = 2 \times q \int_{E_{g,i}}^{\infty} S_{AM1.5D}(E) \cdot T_i(E)\, dE . \tag{2.11}$$

$S_{AM1.5D}$ is the spectral density of photon flux of the AM1.5D illumination (in units of $cm^{-2} \times s^{-1} \times eV^{-1}$), and T_i is the transmission coefficient of the incident light through the i^{th} subcell. Assuming no transmission loss through the phase mask, T_i is simply given by the transmission curves in **Fig. 2.3b** or **Fig. 2.3d**. In setting the limits of integration, it was assumed that no photons are absorbed below the bandgap ($E < E_{g,i}$) and all photons are absorbed above the bandgap ($E \geq E_{g,i}$). The factor of two is a concentration factor arising from focusing the incident illumination on the phase mask to a sub-cell with half the area. This factor provides a small boost in the voltage of the cell.

In the absence of incident illumination, the cell is in thermal equilibrium with its surroundings at temperature T. By the principle of detailed balance, the rate of absorption of thermal radiation from the cell's surroundings is equal to the flux of emitted photons from the top surface of the cell. Thus, if the cell emits with a Lambertian distribution into an environment with refractive index n =1 (as in our experimental system), the emitted flux is found by

integrating the spectrum of blackbody radiation. However, not all of the photons emitted internally in the cell can escape from the top surface, as some are lost through non-radiative recombination or through emission into the substrate. The dark current is hence increased by the factor $1/\eta_{ext}$,[32] where η_{ext} (≤ 1) is the external luminescence yield of the cell, also called the external radiative efficiency:[33]

$$J_{0,i} = \frac{1}{\eta_{ext,i}} \times q \cdot \frac{2\pi}{c^2 h^3} \int_{E_{g,i}}^{\infty} \frac{E^2}{e^{E/kT} - 1} \, dE \, . \tag{2.12}$$

where c is the speed of light and h is Planck's constant. It has been shown that the radiative limit of $\eta_{ext} = 1$ yields the Shockley-Queisser limit of photovoltaic conversion efficiency.[32] Therefore, we consider $\eta_{ext} = 1$ as the case of ideal material quality, with a cell designed to maximize light extraction.

The output electrical power density is given by the product $J_i \times V_i$. The operating current and voltage ($J_{op,i}$, $V_{op,i}$) of the cell are the values for J_i and V_i that maximize this product. Finally, the electrical power output from the two cells are added to give the photovoltaic efficiency of the independently-connected two-junction system:

$$\eta_{PV} = \frac{\frac{1}{2} A_M \cdot J_{op,1} V_{op,1} + \frac{1}{2} A_M \cdot J_{op,2} V_{op,2}}{A_M \cdot \int_0^{\infty} S_{AM1.5D}(E) \cdot E \, dE} \, , \tag{2.13}$$

where A_M is the area of the phase mask and each subcell occupies half the area of the phase mask. The denominator represents the total integrated power in the AM1.5D solar illumination incident on the phase mask.

Fig. 2.11a shows the modified solar spectra (the integrand in **Equation 2.13**) incident on each of the two subcells in the system, compared to the standard AM1.5D spectrum. The transmission coefficient through each cell is found by simulating the fabricated structure in **Fig.**

2.3c over the full spectral extent of the AM1.5D spectrum. This operation is equivalent to producing the dashed curves in **Fig. 2.3d**, but over the wider range of 280 nm to 4000 nm (only wavelengths shorter than 2500nm are shown in **Fig. 2.11**). The splitting cross-over of 760 nm is evident from this plot. The choice of bandgaps that optimizes the two-junction PV efficiency in **Equation 2.13** is 1.64 eV for the visible subcell (which matches the 760nm wavelength) and 1.12 eV for the infrared subcell. In the radiative limit ($\eta_{ext} = 1$), the detailed-balance limit of photovoltaic efficiency for the two-junction system is 36.5%. Considering the efficiency of each cell alone (with 1x concentration), the visible subcell converts its incident illumination with 37.5% efficiency, while the infrared subcell has 34.1% efficiency. Both of these individual conversion efficiencies are enhanced above the Shockley-Queisser limit of 33.3%, which applies for single-junction solar cells under the unmodified AM1.5D spectrum.[1, 32]

The radiative limit can be approached very closely by materials like GaAs,[32] but less ideal materials will fall short of the limit. The two-junction efficiencies for less ideal values for η_{ext} are listed in **Table 2.1**. For the modified spectra in **Fig. 2.11a**, the optimal bandgaps remain at 1.64 eV and 1.12 eV.

Fig. **2.11b** shows the direct solar spectrum as modified by the response of the computationally optimized phase mask in **Fig. 2.3a**, before fabrication errors. As noted in the main text, the spectral splitting efficiency is both higher away from the cutoff of 760nm and sharper close to the cutoff. This can also be seen in the modified spectra in **Fig. 2.11b** when compared to **Fig. 2.11a**. The two-junction detailed-balance limit of photovoltaic efficiency in this case is 40.4%, a significant improvement over the fabricated phase mask. The large difference suggests that high spectral splitting efficiency is important for a high photovoltaic conversion efficiency in this system. Especially important is the sharpness of the spectral

splitting response near the cutoff of 760 nm; a sharp spectral response enhances the amount of absorption near the band edge of the visible subcell, where the photons are most efficiently utilized. The optimal bandgap choice for this phase mask is 1.64 eV for the visible subcell and 0.95 eV for the infrared subcell. The redshift in the lower bandgap likely results from the improved spectral splitting efficiency for longer wavelengths. The efficiency of this structure for lower values of η_{ext} are listed in **Table 2.1**.

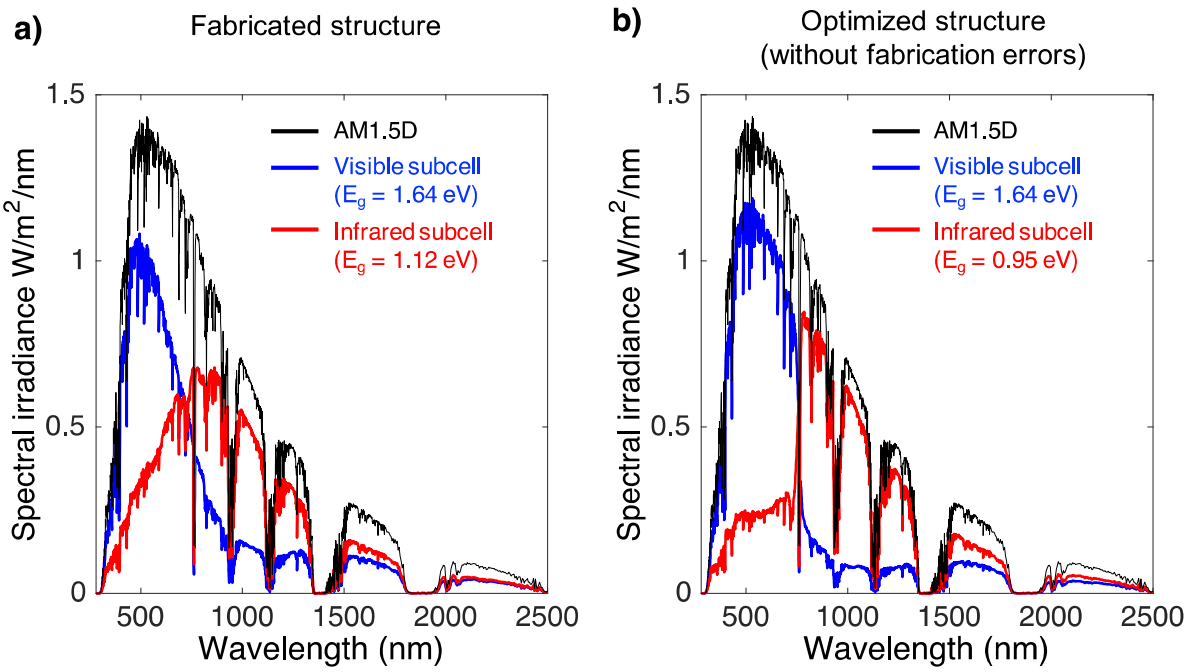

Figure 2.11 The incident spectrum on each of the two subcells is the AM1.5D direct solar spectrum modified by the spectral splitting function of the phase mask. a) The response of the fabricated phase mask in **Fig. 2.3c** is used, b) the response of the computationally optimized phase mask in **Fig. 2.3a** is used. The unmodified AM1.5D spectrum is shown in black for reference.

	Two-junction PV efficiency	
	Fabricated Structure ($E_{g,vis}$ = 1.64eV, $E_{g,IR}$ = 1.12eV)	Optimized Structure ($E_{g,vis}$ = 1.64eV, $E_{g,IR}$ = 0.95eV)
$\eta_{ext,1} = \eta_{ext,2} = 1$	36.5%	40.4%
$\eta_{ext,1} = \eta_{ext,2} = 0.1$	34.2%	37.7%
$\eta_{ext,1} = \eta_{ext,2} = 0.01$	32.0%	35.0%

Table 2.1 Detailed-balance calculations of two-junction photovoltaic efficiency using the response of the fabricated phase mask and the optimized phase mask at different values of the external luminescence yield η_{ext}.

2.11 One-micron-pixel Optimized Design

Using a smaller pixel size for the same overall design size in principle allows for better performance by providing additional degrees of freedom. Moreover, smaller features diffract more power to larger angles, as seen in **Fig. 2.7**. This allows for an increase in the geometric aspect ratio (lateral size to vertical distance), and therefore a more compact system in the vertical dimension. We therefore optimized, but did not fabricate, a phase mask with one thousand pixels having a width of 1.0μm. Like the optimization presented in the main work, the lateral size of the phase mask is 1.0mm, and the texture is vertically discretized into ten discrete levels spanning 1.8μm (in 200nm steps). The size of the air gap in this optimization was set to 4mm, to make a more compact overall system (**Fig. 2.12a**).

The optimization was carried out in a similar manner as the design in the main work: first, the texture was optimized purely for spectral splitting efficiency, then the discretization

constraints were introduced into the figure of merit. To make the geometrical update, we implemented the Broyden-Fletcher-Goldfarb-Shanno (BFGS) algorithm,[31] which produces superior convergence compared to the method of gradient descent. The simulation resolution was kept at the same value as the previous optimization. Since our optimization process based on the adjoint method does not require additional computational resources for a greater number of design variables (and the BFGS overhead is small), the optimization was completed within about the same amount of time as the design in the main work.

The final texture is shown in **Fig. 2.12b** and its spectral response is shown in **Fig. 2.12c**. Like the results in **Fig. 2.3b**, the simulation comprised of a finite-difference time-domain (FDTD) calculation of the near-field response, followed by a propagation of the field from three periods of the texture. The efficiency is then given by **Equation 2.7** with the transmission coefficients normalized to the image plane of the central period. The spectral splitting efficiency is 84.1% over the 360-1100nm range, and 82.4% over 380-970nm.

Despite the pixel size being comparable to the design wavelengths, the thin phase mask approximation continues to be a reasonable approximation to the exact solution to Maxwell's equations. When using **Equation 2.1** to calculate the near-field response, the spectral splitting efficiency is predicted to be ~1.4% higher than given by an FDTD simulation. This is a sufficiently small error to justify the continued use of the thin mask approximation in optimizations with 1μm pixel size. In addition, the polarization sensitivity remains small, with < 0.1% absolute difference in spectral splitting efficiency between the two polarizations.

Meanwhile, the larger aspect ratio of the system not only allows it to be more compact, but also increases its angular acceptance. Following the arguments presented in the main paper for the 5μm-pixel design, the largest incidence angle permitted by the system before the spectral

splitting efficiency falls to 50% is given approximately by: $\tan^{-1}(0.25\text{mm}/4\text{mm}) = 3.58^{\circ}$. This is a significant improvement over the angular acceptance of the 5μm design with a 13.7mm air gap, which gave a largest acceptable incidence angle of ~1°.

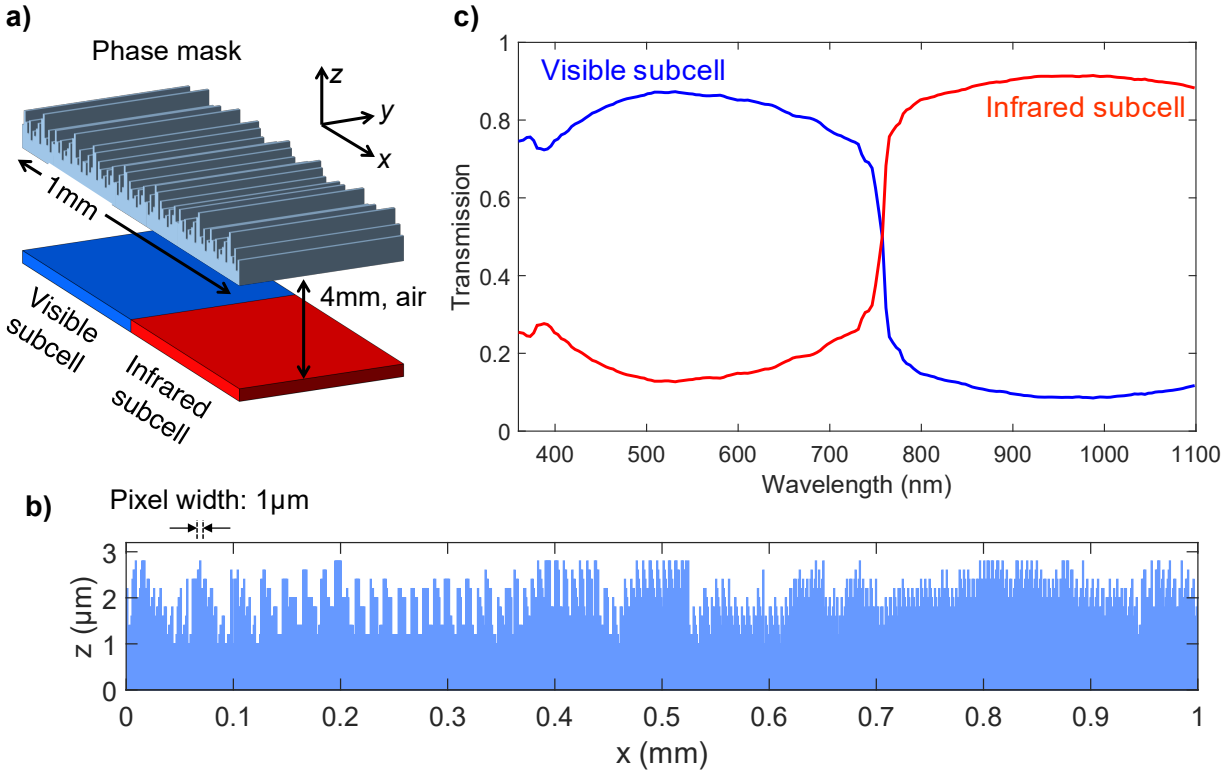

Figure 2.12 a) Schematic of the spectral splitting system with a 1μm-pixel-size phase mask and an air gap of 4mm. b) Height profile of the optimized phase mask, with ten discretized height levels. c) Simulated spectral splitting response of the phase mask in b).

2.12 References

1. Shockley, W.; Queisser, H. J. Detailed Balance Limit of Efficiency of *p-n* Junction Solar Cells. *J. Appl. Phys.* **1961**, *32*, 510-519.

2. Green, M. A.; Emery, K.; Hishikawa, Y.; Warta, W.; Dunlop, E. D. Solar Cell Efficiency Tables (version 46). *Prog. Photovoltaics.* **2015**, *23*, 805-812.
3. Warmann, E. C. Design Strategies for Ultra-high Efficiency Photovoltaics. Ph.D. Thesis, California Institute of Technology, Pasadena, CA, 2014.
4. Torrey, E. R.; Ruden, P. P.; Cohen, P. I. Performance of a split-spectrum photovoltaic device operating under time-varying spectral conditions. *J. Appl. Phys.* **2011**, *109*, 074909.
5. Broderick, L. Z.; Albert, B. R.; Pearson, B. S.; Kimerling, L. C.; Michel, J. Solar spectral variations and their influence on concentrator solar cell performance. *Proc. SPIE* **2013**, *8821*, 88210I-1-88210I-7.
6. Stefancich, M.; Zayan, A.; Chiesa, M.; Rampino, S.; Roncati, D.; Kimerling, L.; Michel, J. Single element spectral splitting solar concentrator for multiple cells CPV system. *Opt. Express* **2012**, *20*, 9004-9018.
7. Barnett, A.; Kirkpatrick, D.; Honsberg, C.; Moore, D.; Wanlass, M.; Emery, K.; Schwartz, R.; Carlson, D.; Bowden, S.; Aiken, D.; Gray, A.; Kurtz, S.; Kazmerski, L. Very High Efficiency Solar Cell Modules. *Prog. Photovoltaics.* **2009**, *17*, 75-83.
8. Eisler, C. N.; Kosten, E. D.; Warmann, E. C.; Atwater, H. A. Spectrum splitting photovoltaics: polyhedral specular reflector design for ultra-high efficiency modules. *IEEE Photovoltaic Spec. Conf., 39th* **2013**, 1848-1851.
9. Brongersma, M. L.; Cui, Y.; Fan, S. Light management for photovoltaics using high-index nanostructures. *Nat. Mater.* **2014**, *13*, 451-460.
10. Levy, U.; Marom, E.; Mendlovic, D. Simultaneous multicolor image formation with a single diffractive optical element. *Opt. Lett.* **2001**, *26* (15), 1149-51.

11. Kim, G.; Dominguez-Caballero, J.-A.; Lee, H.; Friedman, D. J.; Menon, R. Increased Photovoltaic Power Output via Diffractive Spectrum Separation. *Phys. Rev. Lett.* **2013**, *110*, 123901.
12. Kim, G.; Dominguez-Caballero, J.-A.; Menon, R. Design and analysis of multi-wavelength diffractive optics. *Opt. Express* **2012**, *20*, 2814-2823.
13. Shokooh-Saremi, M.; Magnusson, R. Particle swarm optimization and its application to the design of diffraction grating filters. *Opt. Lett.* **2007**, *32*, 894-896.
14. Johnson, E. G.; Abushagur, M. A. G. Microgenetic-algorithm optimization methods applied to dielectric gratings. *J. Opt. Soc. Am. A* **1995**, *12*, 1152-1160.
15. Miller, O. D. Photonic Design: From Fundamental Solar Cell Physics to Computational Inverse Design. Ph.D. Thesis, University of California, Berkeley, CA, 2012.
16. Lalau-Keraly, C. M.; Bhargava, S.; Miller, O. D.; Yablonovitch, E. Adjoint shape optimization applied to electromagnetic design. *Opt. Express* **2013**, *21*, 21693–21701.
17. Scranton, G.; Bhargava, S.; Ganapati, V.; Yablonovitch, E. Single spherical mirror optic for extreme ultraviolet lithography enabled by inverse lithography technology. *Opt. Express* **2014**, *22*, 25027-25042.
18. Ganapati, V.; Miller, O. D.; Yablonovitch, E. Light trapping textures designed by electromagnetic optimization for subwavelength thick solar cells. *IEEE J. Photovolt.* **2014**, *4* (1), 175–182.
19. Bhargava, S.; Yablonovitch, E. Lowering HAMR Near-Field Transducer Temperature via Inverse Electromagnetic Design. *IEEE Trans. Magn.* **2015**, *51* (4), 1-7.
20. Goodman, J. W. *Introduction to Fourier Optics*, 2nd ed.; McGraw-Hill: New York, 1996.

21. Poynting, J. On the Transfer of Energy in the Electromagnetic Field. *Philos. Trans. R. Soc. London* **1884**, *175*, 343–361.

22. Lorentz, H. A. The theorem of Poynting concerning the energy in the electromagnetic field and two general propositions concerning the propagation of light," *H. A. Lorentz Collected Papers* **1896**, *3*, 1–11.

23. Nocedal, J.; Wright, S. J. *Numerical Optimization*, 2nd ed.; Springer: New York, 1999.

24. National Renewable Energy Laboratory. Reference Solar Spectral Irradiance: Air Mass 1.5, ASTM G-173-03. http://rredc.nrel.gov/solar/spectra/am1.5 (accessed Aug 15, 2015).

25. Fischer J.; Wegener, M. Three-dimensional optical laser lithography beyond the diffraction limit. *Laser Photonics Rev.* **2013**, *7*, 22–44.

26. Thorlabs, Inc. C120 Compact Photodiode Power Head with Silicon Detector. http://www.thorlabs.com/thorcat/18300/S120C-SpecSheet.pdf (accessed October 17, 2015).

27. Erbs, D. G.; Klein, S. A.; Duffie, J. A. Estimation of the diffuse radiation fraction for hourly, daily and monthly-average global radiation. *Sol. Energy* **1982**, *28*, 293-302.

28. Chang-Hasnain C. J.; Yang, W. High-contrast gratings for integrated optoelectronics. *Adv. Opt. Photonics* **2012**, *4*, 379-440.

29. Chou, S. Y.; Krauss, P. R.; Renstrom, P. J. J. Nanoimprint lithography. *J. Vac. Sci. Technol., B* **1996**, *14*, 4129-4133.

30. Goodman, J. W. *Introduction to Fourier Optics*, 2nd ed.; McGraw-Hill: New York, 1996.

31. Nocedal, J.; Wright, S. J. *Numerical Optimization*, 2nd ed.; Springer: New York, 1999.

32. Miller, O. D.; Yablonovitch, E.; Kurtz, S. R. Strong Internal and External Luminescence as Solar Cells Approach the Shockley-Queisser Limit. *IEEE J. Photovolt.* **2012**, *2* (3), 303–311.

33. Green, M. A. Radiative efficiency of state-of-the-art photovoltaic cells. *Prog. Photovoltaics.* **2012**, *20*, 472-476.

34. Xiao, T. P.; Cifci, O. S.; Bhargava S.; Chen H.; Gissibl T.; Zhou W.; Giessen H.; Toussaint K. C.; Yablonovitch E.; Braun P. V. Diffractive Spectral-Splitting Optical Element Designed by Adjoint-Based Electromagnetic Optimization and Fabricated by Femtosecond 3D Direct Laser Writing. ACS Photonics, **2016** 3 (5), 886-894

CHAPTER 3

LUMINESCENT CAVITY DESIGN FOR HIGH AMBIENT CONTRAST RATIO, HIGH EFFICIENCY DISPLAYS*

3.1 Introduction and Motivation

Advancements in display technology have immensely increased the data processing rate of humans and continue to evolve with new demands on reduced thicknesses, increased efficiencies, and overall improved designs. Electronic displays come in two fundamentally different display architectures: emissive displays, which emit light directly and non-emissive displays, which modulate light from a source. Liquid crystal displays (LCDs), a non-emissive display, remain the dominant flat panel display technology along with organic light emitting diode (OLED) displays, an emissive technology.[123] LCDs exhibit competitive advantages such as their cost and reliability stemming from years of continued efforts to improve them, however, significant obstacles remain such as their low efficiency and poor contrast ratios.

One key problem of LCDs is their low module efficiency; only 6-7% of the backlight is emitted through the display.[4] One of the most significant loss mechanisms in their design is the substantial absorption from color filters. The color filters generate desired red, green or blue (RGB) pixels by absorbing a portion of the spectrum emitted from a white light emitting diode backlight, cutting maximum achievable efficiencies by one-third from the beginning.[5] Recent work focuses on avoiding color filter absorption by utilizing diffraction, interference or surface plasmon effects to manipulate the spectrum of a broadband backlight source.[67891011] Similar optics have also found applications in solar cells[1213] and image sensors[14] to manipulate and control spectra. These optical solutions, however, require high quality thin-film deposition of multiple materials and/or features on the order of the wavelength of light (< 500 nm) and

*Some portions of this chapter was previously published in a patent by the author.[38]

typically possess angular sensitivity.[15] In addition to their low efficiency, LCDs and various other displays have low ambient contrast ratios, which has a significant impact on image quality.[161718] Reflection of ambient light from the optical components of an LCD leads to a dimming effect due to the emitted light from the display competing with reflected light from the ambient. Hence, it is vital to suppress reflection on the display surface. LCDs employ a circular polarizer to reduce reflection at the face of the display.[1920] Here, external irradiation becomes circularly polarized incident on the display and upon reflection from an internal surface, its polarization state reverses so that the beam is now completely blocked by the circular polarizer on the way back. While effective, emission from the display components also passes through the circular polarizer, which absorbs almost half of the emitted light immediately preceding the viewer. Therefore, display architectures with low incident reflectance and high transmittance of auxiliary optical components is highly desirable for further improvement of display technology.

Here, we show a new design for a display that uses a quantum dot (QD)-based luminescent waveguide inside of a reflective cavity to provide high photon extraction efficiency and low incident reflectance from the top surface of the display. Photoluminescence from the QDs is mostly trapped in the waveguide via total internal reflection (TIR); escaped photons are reflected inside the cavity until extracted from a small aperture at the top of the device. Due to their narrow bandwidth emission,[212223] QDs can be used in such a design to eliminate absorptive color filters while still taking from mature and cost-effective LCD technology. Additionally, this design implements a patterned black absorbing layer on top of the pixel array to prevent reflection of ambient light to the viewer and thus improve the ambient contrast ratio, a much-needed feature for electronic devices used in outdoor environments.

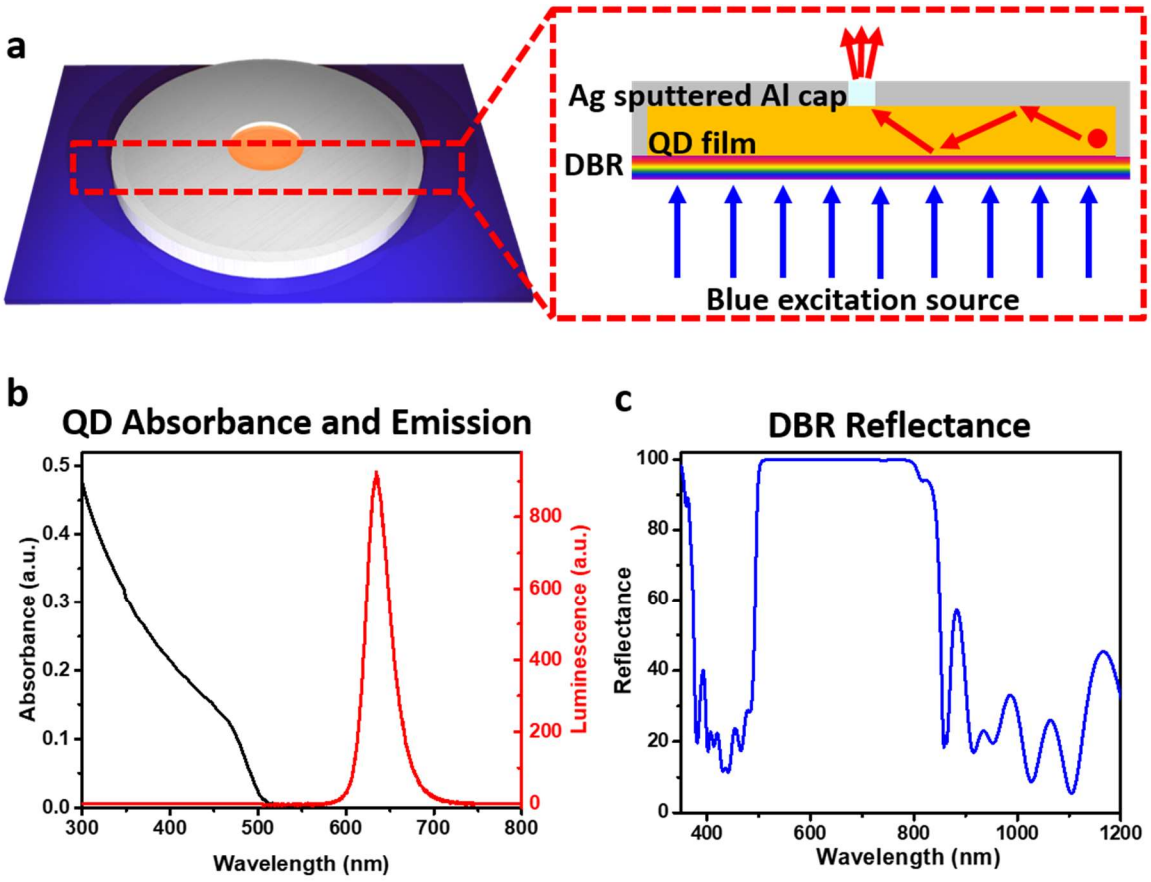

Figure 3.1 a) 3D and cross-section view of the proposed design. The film is 12 mm in diameter. b) Measured absorbance and emission spectrum of the QD film c) Measured reflectance of DBR.

Photovoltaics have utilized waveguides for the purpose of concentration for over 40 years and work on these luminescent solar concentrators (LSCs) continues to develop and increase optical efficiencies.[24] First introduced in 1973 by Lerner,[2526] an LSC utilizes a luminophore embedded in a polymer or glass waveguide to absorb incident solar irradiance from all angles (i.e., direct and diffuse sunlight). The photon transport relies on the TIR modes of the waveguide, directing the emitted light to the edges of the matrix. Concentration is effected by the Stokes shift of the dye, where the decrease in entropy of the light (i.e., concentrated light) comes at the expense of a loss in energy from the down-converted photon. Concentration ratios greater than

30 have been demonstrated in the literature that minimize parasitic losses of LSCs including dye reabsorption and waveguide efficiency.[27] Here, we take improvements made on LSCs and transform the design into an emissive display technology. Instead of concentrating photons towards a solar cell, photons are directed towards a small aperture placed at the top of an optical microcavity, in which the outer surface is covered by an absorptive surface.

This luminescent cavity design builds upon conventional LCD designs, taking elements from existing, high-performing designs and eliminating poor-performing aspects, such as the absorbing color filters. This design strategy has the potential to increase module efficiencies, leading to a reduction in power demands and additionally improves upon ambient contrast ratios, making it a particularly promising design to keep LCD technology competitive and withhold its lion's share in the display market.

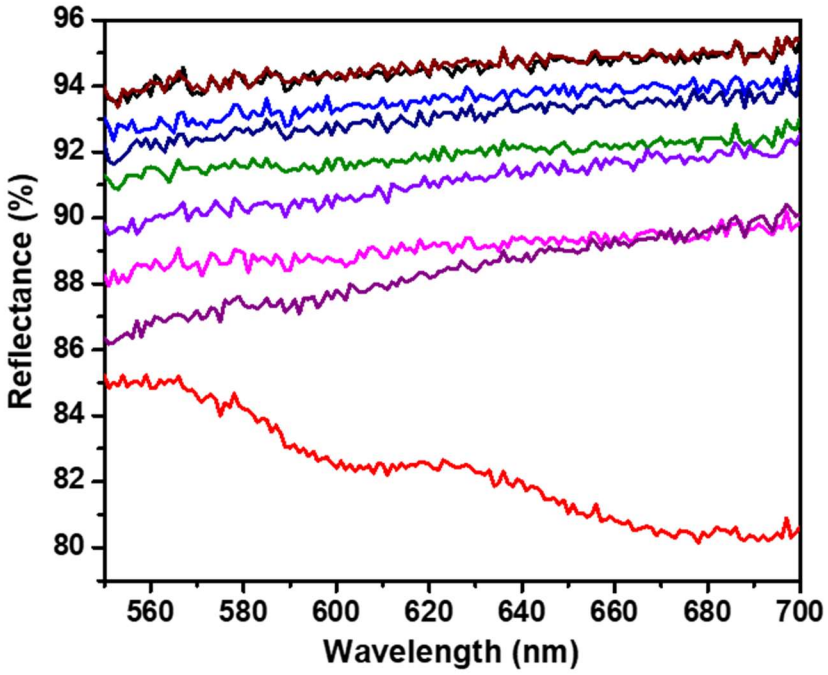

Figure 3.2 Measured reflectance of the machined reflective walls. Any sample having less than 90% reflectance has been ruled out.

3.2 Display Architecture

We propose to replace the color filters in conventional LCDs with a luminescent cavity. **Figure 3.1a** displays the single pixel design, comprised of an enclosed reflective cavity. The back surface utilizes a distributed Bragg reflector (DBR) to transmit the excitation wavelengths into the cavity, and the remaining interior surfaces are designed to be highly reflective to support photon recycling; a pinhole opening on the front surface serves as the extraction point of light from within the cavity. A luminescent waveguide, QD-doped poly(lauryl methacrylate) (PLMA), sits inside the cavity. **Figure 3.1b** shows absorption and emission of the QDs used in this study. These core-shell CdSe/CdS QDs absorb strongly in the blue and ultraviolet wavelength ranges

(black, **Figure 3.1b**) and emit at a center wavelength of 630 nm (red, **Figure 3.1b**). Notably, these QDs have very little absorption in the range where they emit, leading to very few reabsorption events (a key parasitic loss in LSCs). Further, emission from QDs demonstrates narrow linewidth (full-width at half-maximum, FWHM, of 31.6 nm) rendering color filter elimination possible. The DBR is composed of a deposited multilayer stack of transparent oxides and is used as the back surface, designed to be highly transparent at the excitation wavelength (440 nm) and almost 100% reflective at the emission wavelength of the QDs (630 nm, **Figure 3.1c**). The interior surfaces of an aluminum cap are sputter-coated with silver to create the rest of the reflective cavity, exploiting the high reflectivity of silver at the wavelength range of interest.[28] Custom aluminum caps were machined for this design and due to inconsistencies during processing and polishing, we determined a threshold of reflectivity for the caps as poor reflectivity was detrimental to the extraction efficiency. **Figure 3.2** shows the diffuse reflectance for a set of sputter-coated aluminum caps along with the threshold that we chose (> 90% at 630 nm).

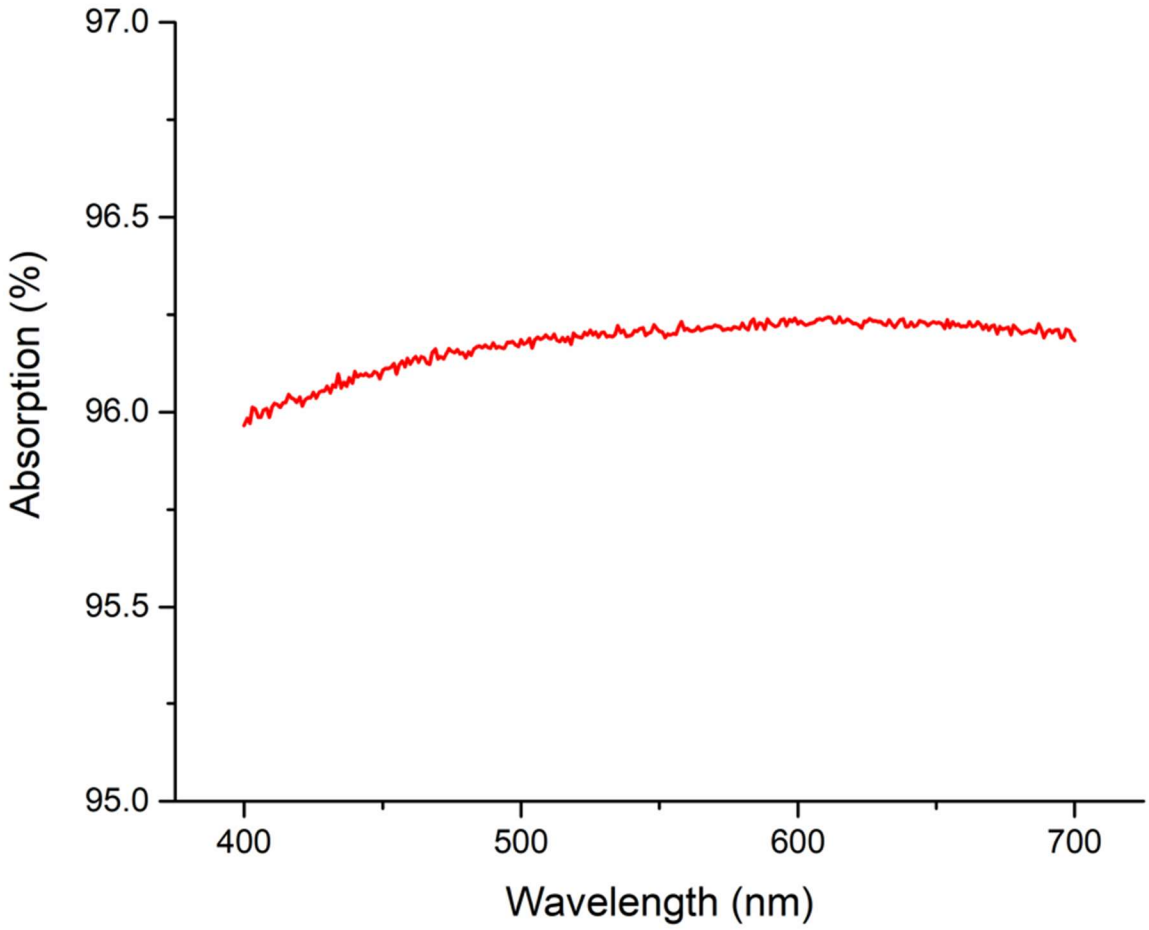

Figure 3.3 Absorbance spectrum of black PDMS layer measured using UV-Vis spectrometer.

The second key component of this design implements an absorbing material on the external surface of the device. Here, thin membranes of poly(dimethylsiloxane) (PDMS) mixed with iron oxide nanoparticles (defined as black PDMS, bPDMS) were used as a black absorbing material. **Figure 3.3** shows the absorbance spectrum of a thin (ca. 50 μm) bPDMS membrane.

Each pixel can be individually addressed by introducing a blue backlight behind the DBR. As opposed to conventional LCDs, which use a broadband light source, our source has a very narrow linewidth with a FWHM of 5.4 nm. In a full-color (i.e., RGB) display, green- and

red-emitting QDs may be used to generate these two colors and the light source itself can be used directly to generate the blue color. As a proof-of-concept, we use QDs with emission at a center wavelength of 630 nm, but the unique optical design principals can be easily translated to extended materials sets (i.e., QDs with varying emission). In this way, an RGB display is realized that minimizes parasitic absorption of the backlight as the blue backlight in this design gets absorbed by QDs, but is then re-emitted and directed outwards with limited loss due to the highly reflective interior surfaces and selective reflectance of the DBR.

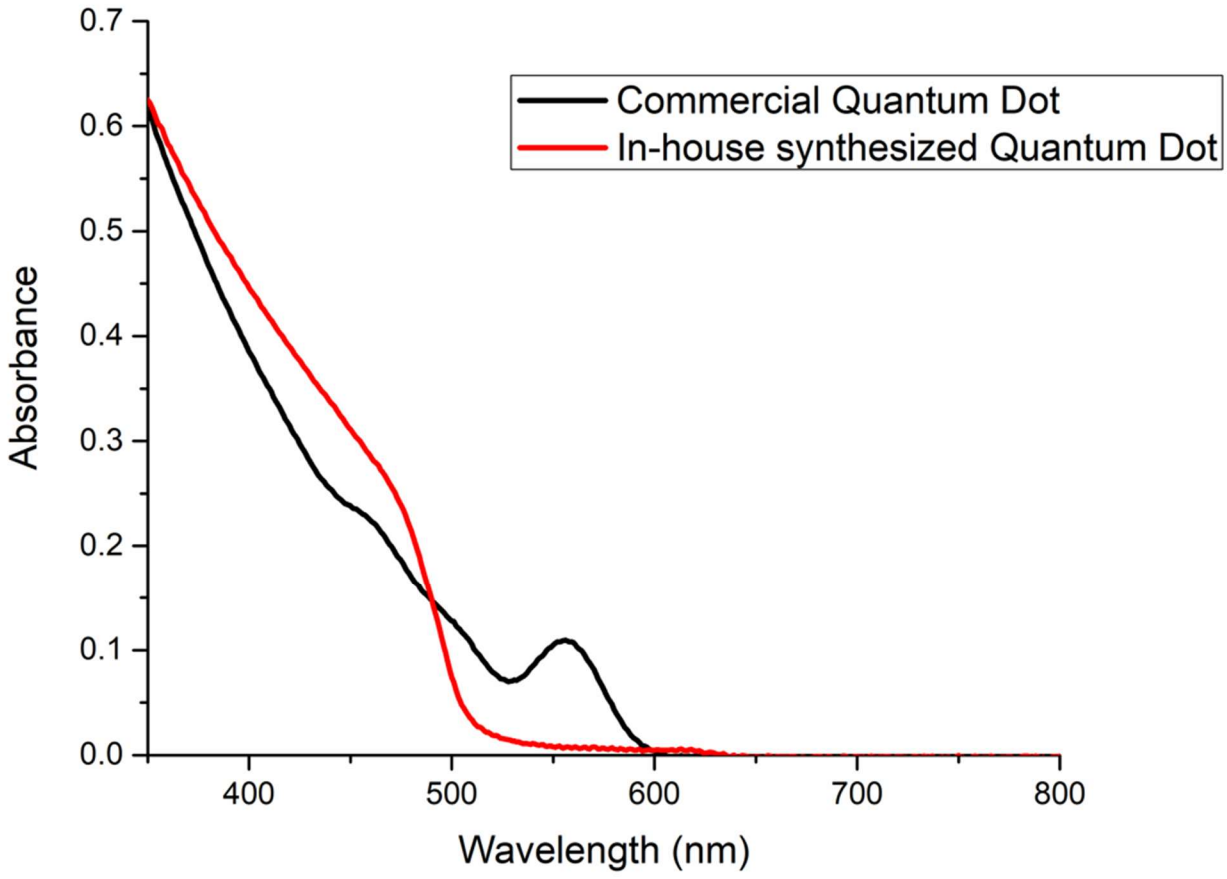

Figure 3.4 Measured absorbance of two QD films. Red line shows the spectrum of in-house synthesized QD and black line shows the spectrum of commercial QD.

Previous work on LSCs suggests that the luminophore should be considered very carefully and that it should satisfy multiple requirements.[26272930] These include a large Stokes shift to prevent reabsorption, high quantum yield, and the polymer matrix that surrounds the QDs should prevent scattering of photons and be overall non-absorbing. **Figure 3.1b** clearly shows the large Stokes shift of the CdSe/CdS QDs, minimizing reabsorption, and their high quantum yield in solution results in a quantum yield of 77.7% embedded in the polymer matrix. The large improvement in reabsorption is further illustrated when comparing the synthesized CdSe/CdS QDs to commercial QDs, as seen in **Figure 3.4**. The commercial QDs show a peak that is directly related to a reabsorption event due to their smaller Stokes shift. The large Stokes shift of the CdSe/CdS QDs has previously been optimized by manipulating shell thickness (CdS) to dictate the absorption spectrum and can also be tuned via core size (CdSe).[2729] Finally, the polymer matrix we use, PLMA, exhibits high transmittance and does not cause aggregation of the core-shell QDs (a source of scattering within the matrix).

3.3 Factors Affecting Efficiency

For the purpose of this study, we define the extraction efficiency ($\eta_{extract}$) as follows:

$$\eta_{extract} = \frac{I_{PL}}{I_S}$$

where I_{PL} is the intensity of the photoluminescence of the assembled device and I_S is the intensity of the excitation source (i.e., transmitted intensity through a device with no luminescent film). An in-house fluorometer setup with an integration sphere was used to measure light intensities with a CCD camera; a schematic of this setup can be seen in **Figure 3.5**. I_{PL} and I_S were calculated by integrating the measured counts at the wavelength range of interest.

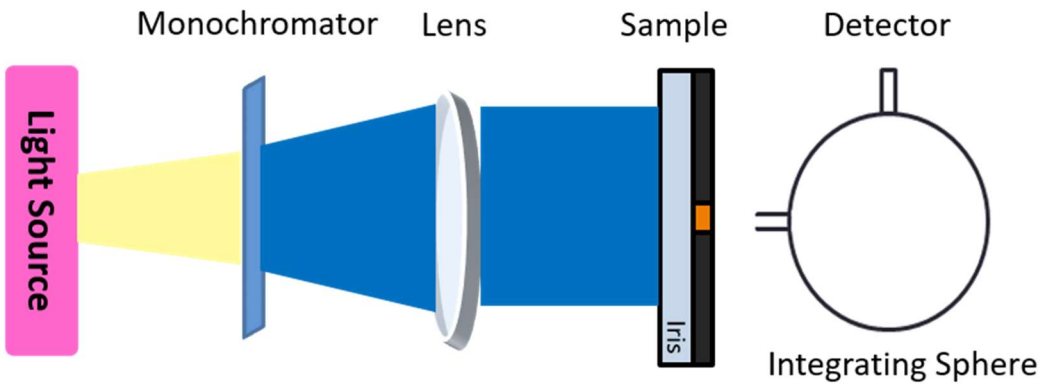

Figure 3.5 Schematic of the optical characterization setup to measure efficiency and leakage of the devices.

Control experiments were done to validate the characterization setup with no film inside the optical microcavity. Aperture areas, defined as the area of the opening over the total area of the top surface, of 2.8% and 11% showed 3.0% and 9.9% of the excitation source leaking through the device, respectively. These values agree well with the aperture area values (i.e., 2.8% and 11%) as expected. As an additional control, we measured devices with an undoped PLMA film (i.e., no QD) and observed 3.0% and 9.9% of the excitation source leaking through, illustrating the high transparency of the PLMA matrix.

Figure 3.6a shows the measured spectra of the excitation source (shown in black) and sample photoluminescence (shown in red) from a sample having an 11.1% aperture area. The extraction efficiency of the sample is calculated to be 40.9%, which is significantly better than the theoretical maximum possible efficiency of an absorptive color filter of 33.3%5. The QD films do exhibit transparency to the excitation wavelength, which was observed to be only 0.7% of the source light for the 11.1% aperture area. Should this leaked light become significant, it

might be desirable to add an optical element such as a bandpass filter on top of the cavity to absorb this undesired leakage.

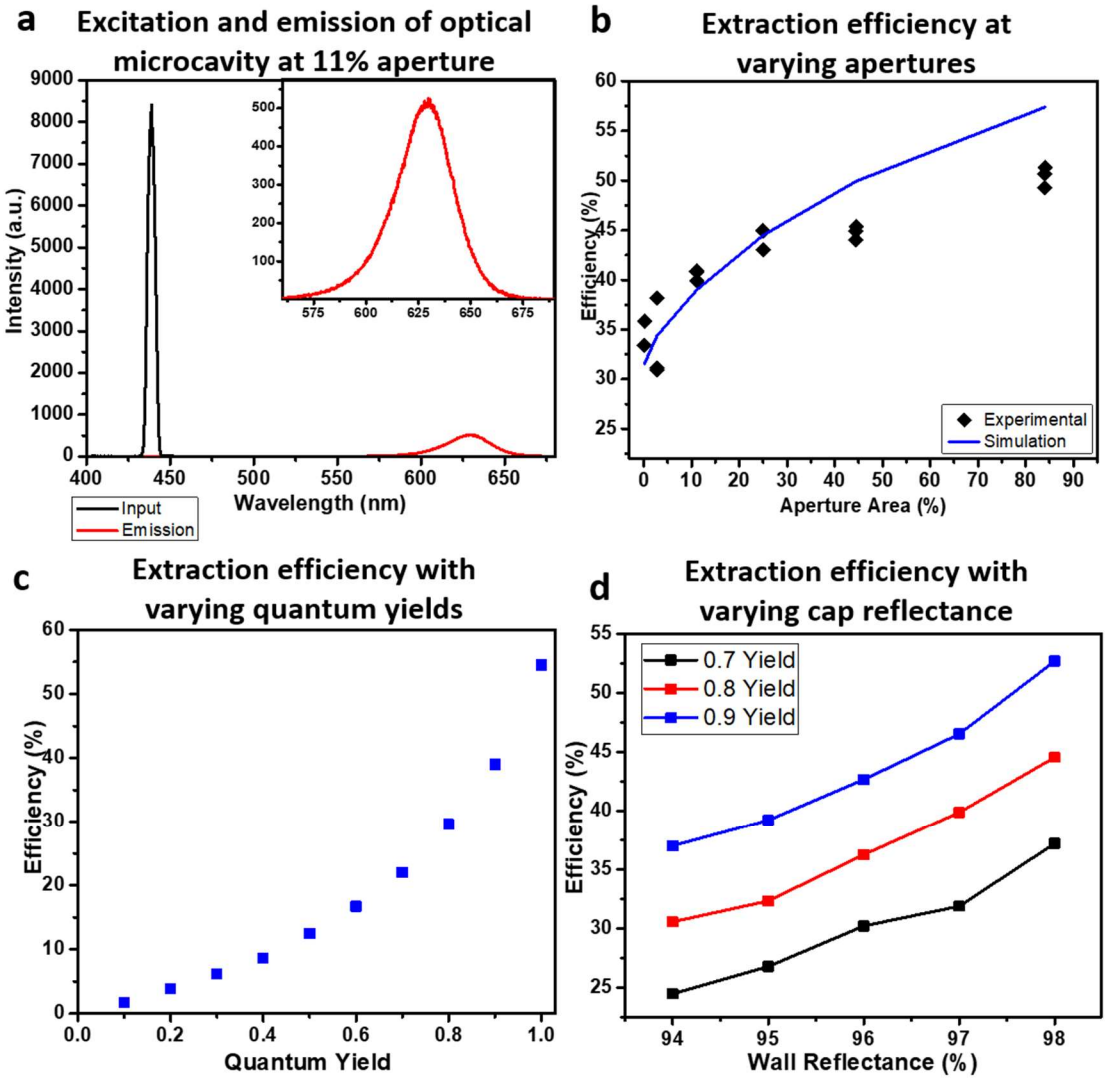

Figure 3.6 a) Measured excitation (in black) and emission (in red) of the device having 11% aperture. The inset shows the zoomed in emission spectrum b) Experimental (in solid diamonds) and simulation (in blue line) efficiencies for various aperture openings c) Simulation studies showing how the quantum yield affects the efficiency at a fixed aperture area d) Simulation result of efficiency for devices having various wall reflectances and quantum yields.

Monte Carlo ray tracing simulations further corroborate our experimental data and illustrate possible efficiency enhancements with various materials improvements. Monte Carlo models are regularly used to simulate LSCs to predict device performance.[313233] Here, we use a modified version of an LSC model used in previous works.[27]

There are multiple factors that affect the efficiency of the devices, of which one easily tunable factor is aperture area. A larger aperture area results in higher efficiencies due to fewer necessary reflections within the cavity, ultimately minimizing losses associated with multiple non-unity reflections. Larger apertures, however, directly affect how much of the top surface area is covered by the absorptive layer, resulting in a reduced ambient contrast. Hence, there is an inherent trade-off between $\eta_{extract}$ and the ambient contrast ratio. To this end, we measured efficiencies of devices with six different aperture areas, from 0.17% to 84% and these results are shown in **Figure 3.6b**, where the diamonds refer to experimental results and the simulation results are shown in blue. Experimental results show that $\eta_{extract}$ can be modulated from 35.8% to 51.3% with varying aperture areas. The simulation matches well with the experimental data at smaller aperture areas, but there lies a discrepancy at larger aperture areas. We attribute this difference to the machined aluminum caps, which introduce deviations from the desired reflectance, particularly at the corners of the interior surfaces. Larger aperture area caps are predominately comprised of these corners and exhibited reduced reflectance compared to the smaller aperture area caps. We propose that reflective caps fabricated with high quality, flat optical surfaces could mitigate this discrepancy and would follow the simulated efficiency results.

In addition to the aperture area, another important factor affecting $\eta_{extract}$ of the device is the quantum yield of the luminescent layer. Higher quantum yields result in a higher efficiency

due to suppression of non-radiative processes. **Figure 3.6c** illustrates this dependence of quantum yield on a device with 11.1% aperture opening. In the case of unity quantum yield, the simulation predicts an efficiency of 57%, which is nearly twice that of the conventional color filter array (i.e., 33.3%).

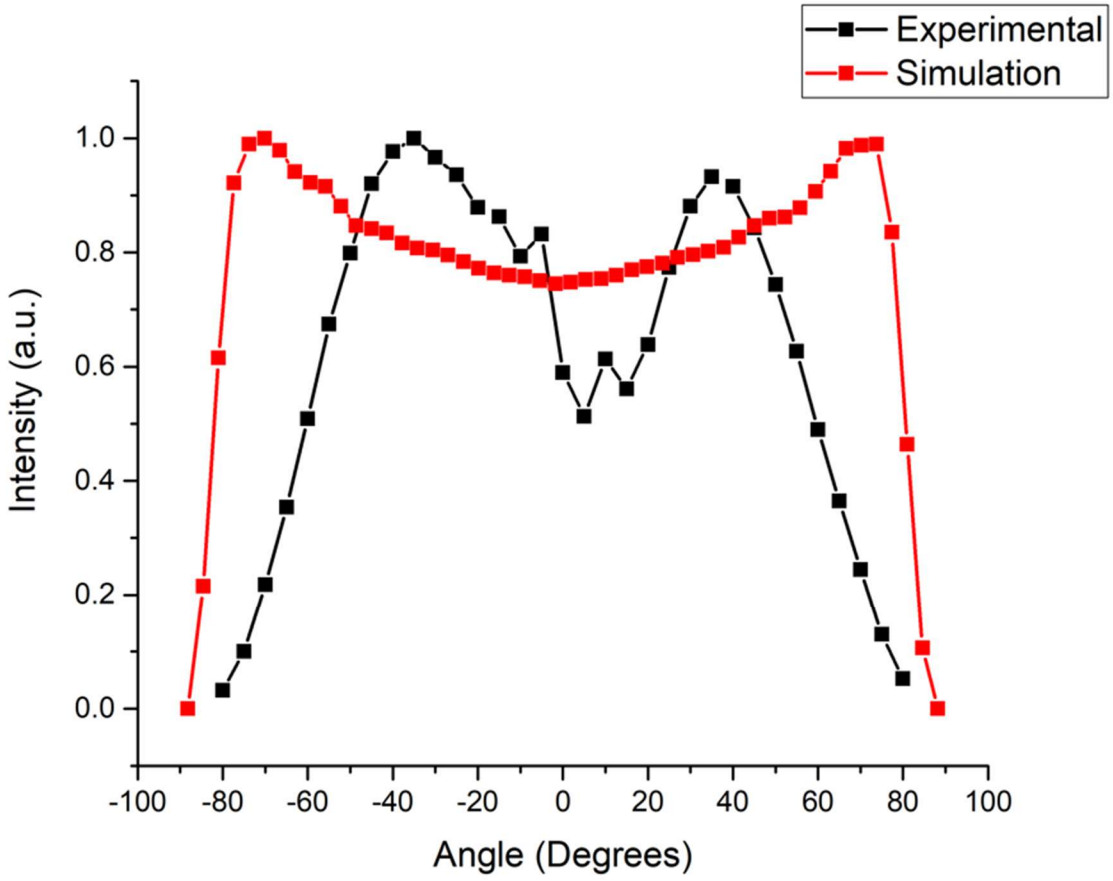

Figure 3.7 Radiance pattern of the device showing wide-view emission.

Loss of efficiency in the extraction of photons from the aperture also stems from imperfect reflectance on the interior surfaces of the cavity. A fraction of the emitted light will be absorbed by the metal layer, reducing $\eta_{extract}$. The simulations assume a reflectance of 96% for the interior surfaces that are silver sputter-coated. **Figure 3.6d** shows the simulation results of

devices with various interior surface reflectivities for three different quantum yields. As expected, $\eta_{extract}$ increases with surface reflectance due to minimized absorption losses by the metal layer.

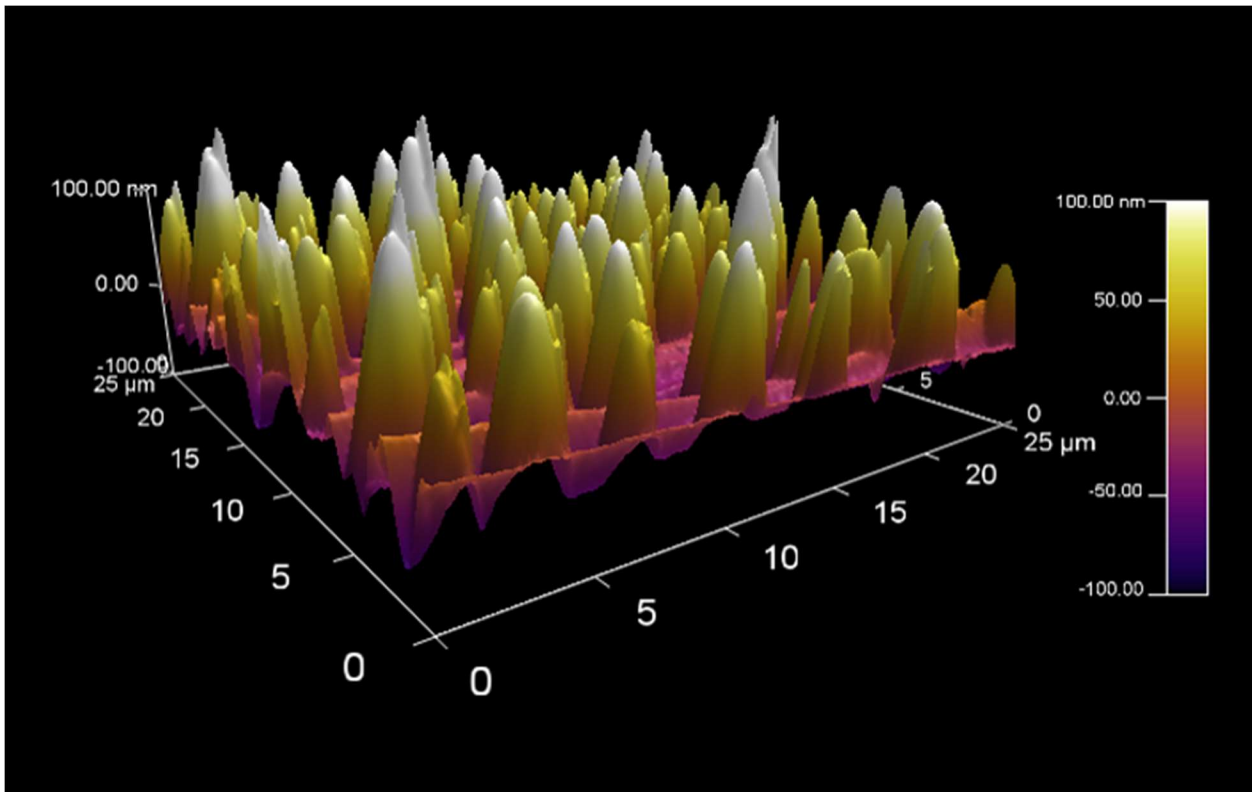

Figure 3.8 Atomic force microscopy image of QD film showing the surface roughness for a 625 μm^2 area.

One of the most important aspects of a display that dictates its specific application is its viewing angle.[34] Wide viewing angles are usually preferred for large displays and televisions whereas small, portable electronics typically employ narrow viewing angle focused on directing emission normal to the surface for single-user purpose. [35] We measured luminance of the device at every 5° and compared the results to a ray tracing simulation (see **Figure 3.7**). The measured luminance shows a broad viewing angle with a dip at the normal direction whereas the

simulation predicts the highest luminance at 70°. Since the luminesced light trapped within the waveguide is traveling laterally, the photons having a higher emission angle are more likely to escape the device, explaining the higher luminance at high angles. However, in the experimental study the QD film is not optically smooth as per the AFM image in **Figure 3.8** which may explain the deviation from the simulation. It is important to note that a fully assembled display is composed of multiple layers, which introduces complexity into the emission pattern[36] and additional optics could be utilized to modify the viewing angle as needed.[37]

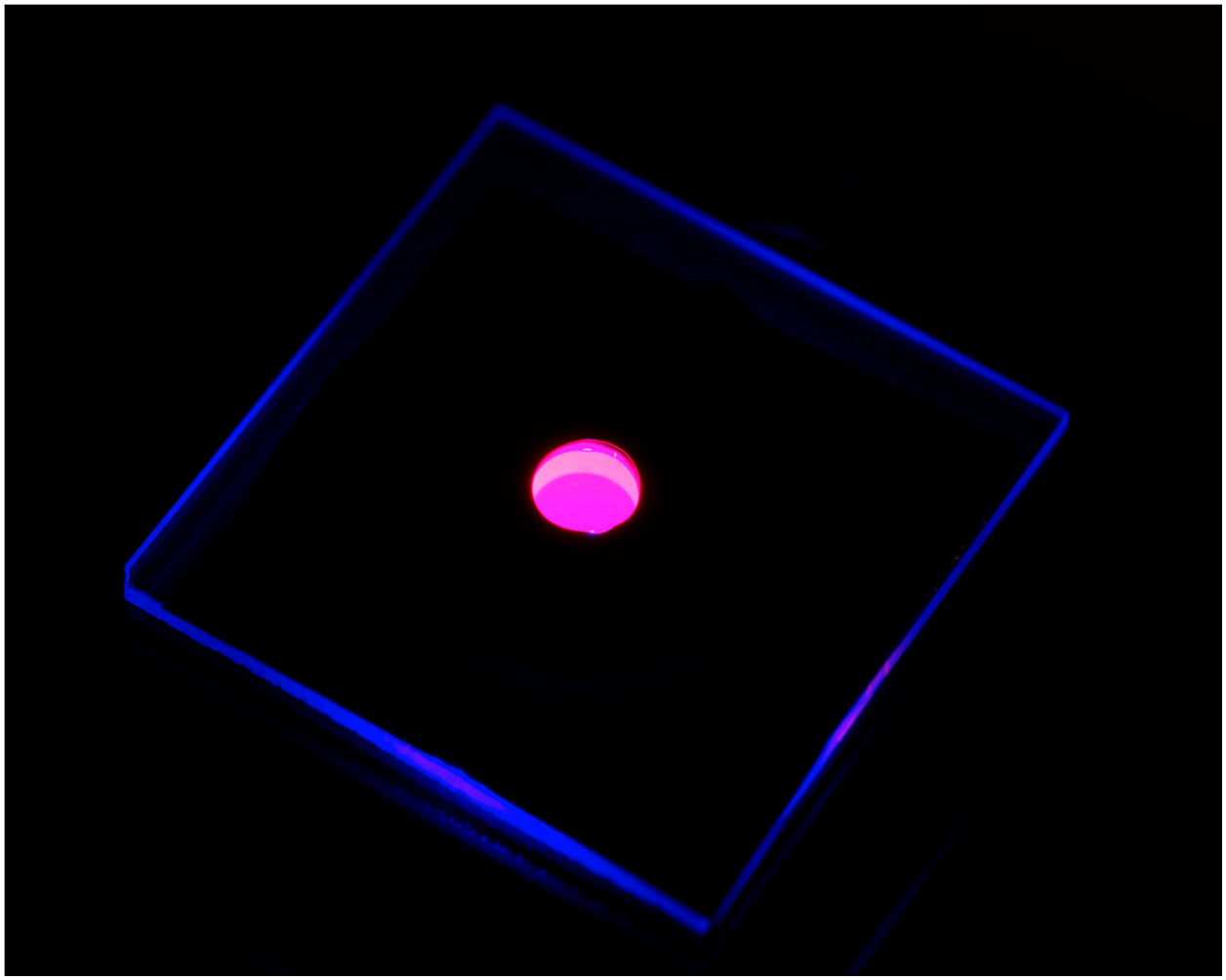

Figure 3.9 Photograph of the assembled device (12 mm diameter film is sitting on a 25 mm DBR) under dark conditions when the backlight is on.

To demonstrate the proposed device performs well under high ambient light, we took photographs of the device when the backlight is on. **Figure 3.9** shows the device under dark ambient light conditions and **Figure 3.10** shows the same device under high ambient light conditions. Emission from the aperture is still clearly visible demonstrating the suitability of the proposed display architecture.

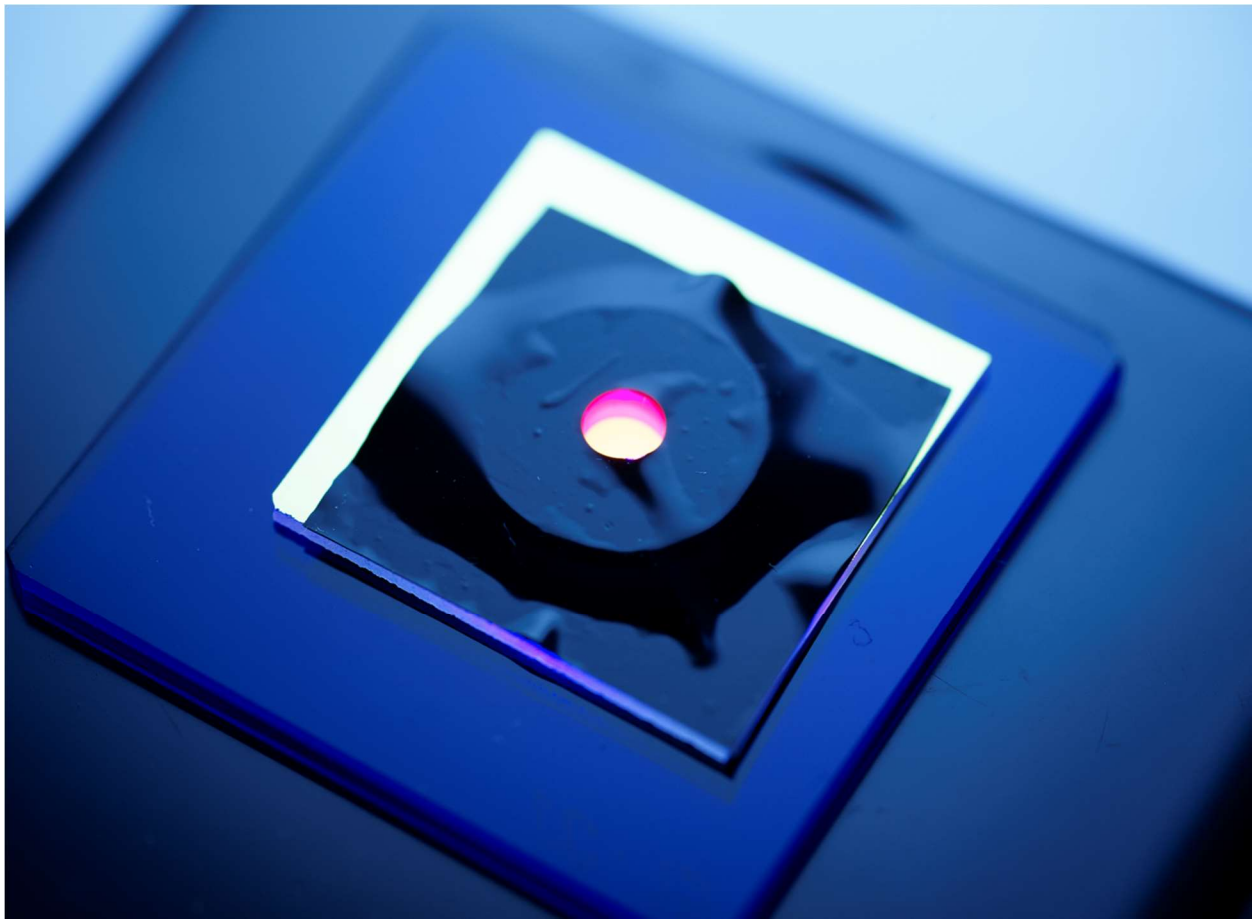

Figure 3.10 Photograph of the device under high ambient light. Light emission from the aperture is clearly visible demonstrating sunlight readability. The device consists of a 12 mm diameter QD film sitting on a 25 mm DBR.

3.4 References

1. Zhang, Y. S., Liu, C. Y., Emelyanenko, A. V. & Liu, J. H. Synthesis of Predesigned Ferroelectric Liquid Crystals and Their Applications in Field-Sequential Color Displays. Adv. Funct. Mater. (2018). doi:10.1002/adfm.201706994
2. Yang, D.-K. . & Wu, S.-T. . Fundamentals of Liquid Crystal Devices. Fundamentals of Liquid Crystal Devices (2014). doi:10.1002/9781118751992
3. Tsujimura, T. OLED Display Fundamentals and Applications. John Wiley & Sons, Inc. (2012). doi:10.1016/S0379-6779(98)80075-1
4. Armitage, D., Underwood, I. & Wu, S.-T. Introduction to Microdisplays. (John Wiley & Sons, Ltd., 2006).
5. Luo, Z., Zhang, G., Zhu, R., Gao, Y. & Wu, S.-T. Polarizing grating color filters with large acceptance angle and high transmittance. Appl. Opt. (2016). doi:10.1364/AO.55.000070
6. Yang, C. et al. Compact multilayer film structure for angle insensitive color filtering. Sci. Rep. (2015). doi:10.1038/srep09285
7. Kanamori, Y., Shimono, M. & Hane, K. Fabrication of transmission color filters using silicon subwavelength gratings on quartz substrates. IEEE Photonics Technol. Lett. (2006). doi:10.1109/LPT.2006.883208
8. Ye, Y., Zhou, Y., Zhang, H. & Chen, L. Polarizing color filter based on a subwavelength metal–dielectric grating. Appl. Opt. (2011). doi:10.1364/AO.50.001356
9. Fleischman, D., Sweatlock, L. A., Murakami, H. & Atwater, H. Hyper-selective plasmonic color filters. Opt. Express (2017). doi:10.1364/OE.25.027386

10. Chen, Q. & Cumming, D. R. S. High transmission and low color cross-talk plasmonic color filters using triangular-lattice hole arrays in aluminum films. Opt. Express (2010). doi:10.1364/OE.18.014056

11. Si, G. Y., Leong, E. S. P., Danner, a. J. & Teng, J. H. Plasmonic Coaxial Fabry-Pérot Nanocavity Color Filter. in Proceeding of SPIE (2010). doi:10.1117/12.861151

12. Xiao, T. P. et al. Diffractive Spectral-Splitting Optical Element Designed by Adjoint-Based Electromagnetic Optimization and Fabricated by Femtosecond 3D Direct Laser Writing. ACS Photonics (2016). doi:10.1021/acsphotonics.6b00066

13. Kim, G., Dominguez-Caballero, J. A., Lee, H., Friedman, D. J. & Menon, R. Increased photovoltaic power output via diffractive spectrum separation. Phys. Rev. Lett. (2013). doi:10.1103/PhysRevLett.110.123901

14. Wang, P. & Menon, R. Ultra-high-sensitivity color imaging via a transparent diffractive-filter array and computational optics. Optica (2015). doi:10.1364/OPTICA.2.000933

15. Lee, K. T., Seo, S. & Guo, L. J. High-color-purity subtractive color filters with a wide viewing angle based on plasmonic perfect absorbers. Adv. Opt. Mater. (2015). doi:10.1002/adom.201400533

16. Chen, H., Tan, G. & Wu, S.-T. Ambient contrast ratio of LCDs and OLED displays. Opt. Express 25, 33643–33656 (2017).

17. Lee, J.-H. et al. High ambient-contrast-ratio display using tandem reflective liquid crystal display and organic light-emitting device. Opt. Express (2005).

18. F., K. E., Max, L. & John, P. Display daylight ambient contrast measurement methods and daylight readability. J. Soc. Inf. Disp. 14, 1019–1030 (2006).

19. Bennett, S. & Trapani, G. Contrast enhancement of LED, vaccum fluorescent and plasma displays with circular polarizing filters. Displays (1984). doi:10.1016/0141-9382(84)90006-4

20. Singh, R., Narayanan Unni, K. N., Solanki, A. & Deepak. Improving the contrast ratio of OLED displays: An analysis of various techniques. Optical Materials (2012). doi:10.1016/j.optmat.2011.10.005

21. Chen, O. et al. Compact high-quality CdSe-CdS core-shell nanocrystals with narrow emission linewidths and suppressed blinking. Nat. Mater. (2013). doi:10.1038/nmat3539

22. Steckel, J. S. et al. Quantum dots: The ultimate down-conversion material for LCD displays. J. Soc. Inf. Disp. (2015). doi:10.1002/jsid.313

23. Kim, H.-J., Shin, M.-H., Lee, J.-Y., Kim, J.-H. & Kim, Y.-J. Realization of 95% of the Rec 2020 color gamut in a highly efficient LCD using a patterned quantum dot film. Opt. Express (2017). doi:10.1364/OE.25.010724

24. Meinardi, F. et al. Highly efficient luminescent solar concentrators based on earth-Abundant indirect-bandgap silicon quantum dots. Nat. Photonics (2017). doi:10.1038/nphoton.2017.5

25. Batchelder, J. S., Zewai, A. H. & Cole, T. Luminescent solar concentrators. 1: Theory of operation and techniques for performance evaluation. Appl. Opt. (1979). doi:10.1364/AO.18.003090

26. Debije, M. G. & Verbunt, P. P. C. Thirty Years of Luminescent Solar Concentrator Research: Solar Energy for the Built Environment. Adv. Energy Mater. (2012). doi:10.1002/aenm.201100554

27. Bronstein, N. D. et al. Quantum Dot Luminescent Concentrator Cavity Exhibiting 30-fold Concentration. ACS Photonics (2015). doi:10.1021/acsphotonics.5b00334

28. Babar, S. & Weaver, J. H. Optical constants of Cu, Ag, and Au revisited. Appl. Opt. (2015). doi:10.1364/AO.54.000477

29. Bronstein, N. D. et al. Luminescent solar concentration with semiconductor nanorods and transfer-printed micro-silicon solar cells. ACS Nano (2014). doi:10.1021/nn404418h

30. Yablonovitch, E. Thermodynamics of the fluorescent planar concentrator. J. Opt. Soc. Am. (1980). doi:10.1364/JOSA.70.001362

31. Wilton, S. R. et al. Monte Carlo study of PbSe quantum dots as the fluorescent material in luminescent solar concentrators. Opt. Express (2014). doi:10.1364/OE.22.000A35

32. Leow, S. W. et al. Analyzing luminescent solar concentrators with front-facing photovoltaic cells using weighted Monte Carlo ray tracing. J. Appl. Phys. (2013). doi:10.1063/1.4807413

33. Sahin, D., Ilan, B. & Kelley, D. F. Monte-Carlo simulations of light propagation in luminescent solar concentrators based on semiconductor nanoparticles. J. Appl. Phys. (2011). doi:10.1063/1.3619809

34. Boher, P., Leroux, T., Bignon, T. & Blanc, P. Color display evaluation vs. viewing angle using L*a*b*color space and Fourier-optics measurements. J. Inf. Disp. (2011). doi:10.1080/15980316.2011.621313

35. Lim, Y. J. et al. Viewing angle controllable liquid crystal display with high transmittance. Opt. Express (2010). doi:10.1364/OE.18.006824

36. Boher, P., Leroux, T., Collomb-Patton, V. & Bignon, T. Optical Characterization of OLED Displays. J. Soc. Inf. Disp. (2015).

37. Mori, H. The Wide View (WV) film for enhancing the field of view of LCDs. IEEE/OSA Journal of Display Technology (2005). doi:10.1109/JDT.2005.858935

38. Braun, P.V. et al. Optical Microcavity for a High-Contrast Display. U.S. Patent No.: 10,073,293 B2 (2018)

CHAPTER 4

MICROPIXEL ARRAY DESIGN FOR PORTABLE LUMINESCENT MICROCAVITY DISPLAYS

4.1 Introduction and Motivation

The single pixel demonstration serves to optimize the optics within the cavity and study the physics of the proposed architecture, however, it is not of reasonable dimensions for a pixel in a display panel and further demonstrates only one, single pixel. The current portable electronics industry demands displays with large pixel arrays, where each pixel is on the order of micrometers in size. **Figure 4.1** shows an optical image of 15" Apple Macbook Pro display.[1] Each subpixel has a lateral width of about 60 μm. Due to having smaller display sizes, tablets and phones have even smaller pixels. This chapter introduces a micrometer sized pixel array using the strategies studied in Chapter 3.

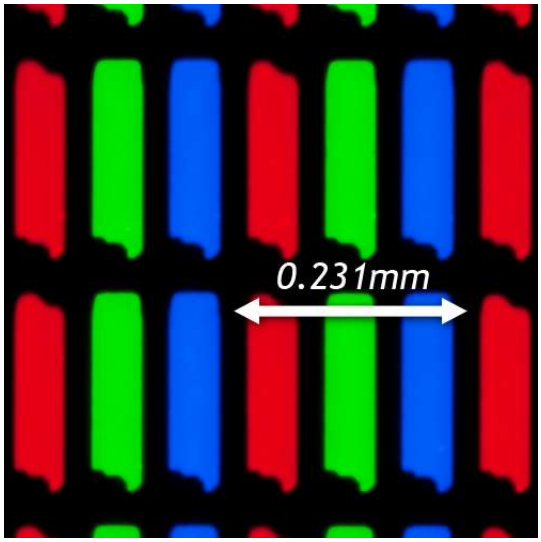

Figure 4.1 Color filter array of 15" Apple Macbook Pro display.

4.2 Design and Microfabrication

Figure 4.2 shows the schematic of a microscale pixel array. Individual pixels are fabricated by polymerizing QD films inside of fabricated holes and can be individually addressed with light sources placed underneath each pixel. Conventional LCDs use a single backlight and turn the desired pixels on and off by applying an electric field, which controls the polarization of the liquid crystals to either block or transmit the emitted light. Our microcavity design is not a complete display but a subcomponent without liquid crystals, so we utilize individual light sources for each pixel. The mode of operation is very similar to the single pixel design. Diffraction due to smaller pixels is not a concern in our design because the size of the pixels are still more than 10 times the wavelength of the light used (i.e., 635 nm).[2]

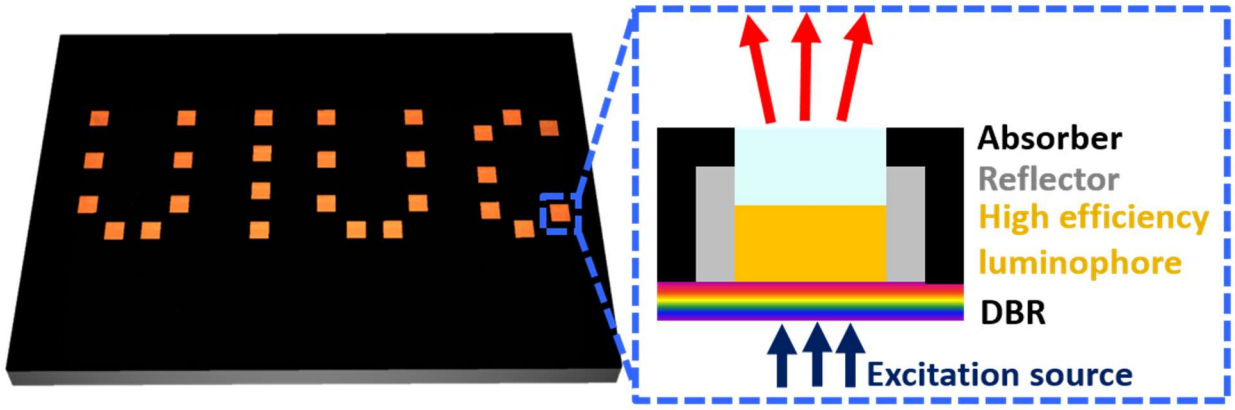

Figure 4.2 3D schematic of micropixel array design (left) and cross-section view of an individual pixel.

We used microfabrication techniques to produce micropixel array device. The desired pattern can be transferred to the substrate using micro and nano-lithography techniques which have been developed thanks to semiconductor industry.[3] In addition to photolithography

techniques other approaches to lithography were also developed: holographic lithography,[4] nanoimprinting lithography,[5] and soft lithography.[6] In photolithography, a custom-made photomask with the desired pattern is transferred onto a photoresist which is a light-sensitive chemical by using light (**Figure 4.3**). [3] A development process takes place after the exposure to the light.

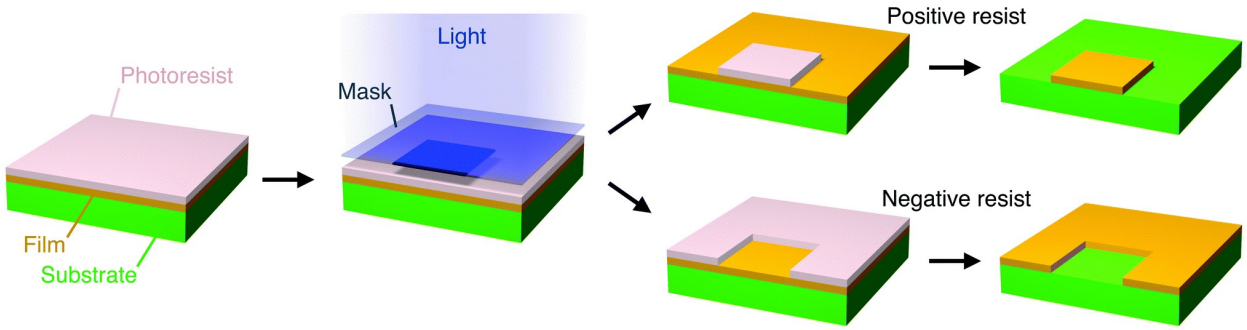

Figure 4.3 Step-by-step photolithography process. Depending on the chemistry of the employed resist exposed or non-exposed pattern can selectively stay on the substrate[3].

The microscale pixel array is fabricated from a thin silicon wafer (200 μm) oriented in (100) direction. **Figure 4.5** illustrates the microfabrication process flow. First, a thin layer of Si_3N_4 is deposited on the Si wafer as a mask layer for a subsequent KOH wet etch. The holes (pixels) are patterned via standard photolithography as mentioned above and the Si_3N_4 layer is then selectively etched to expose the Si using inductively coupled plasma reactive ion etching (ICP-RIE). A scanning electron micrograph (SEM) image is shown in **Figure 4.4**.

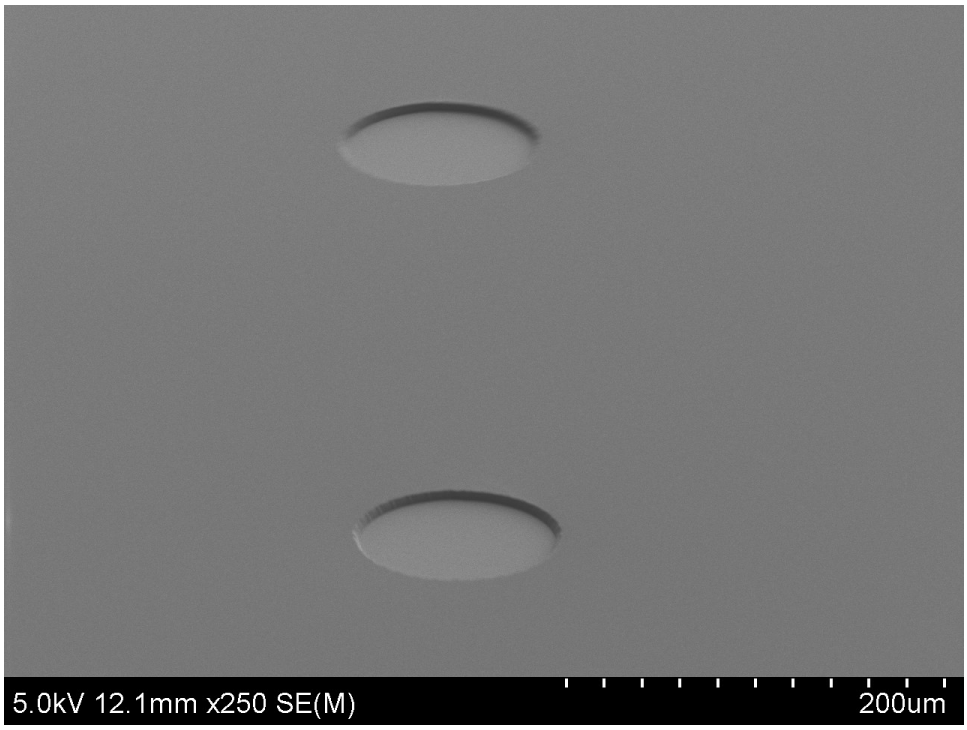

Figure 4.4 SEM micrograph showing 2 pixels after patterning and selective nitride removal.

An anisotropic etchant, potassium hydroxide (KOH), is used to etch Si, resulting angled sidewalls.[7] Aqueous KOH etching has been used in the microelectronics industry in the 1980s and production of VMOS transistors, pyramids for field-emitter arrays, and thin-wall Josephson junctions.[8] KOH etches silicon's planes at a different rate, giving angled sidewalls. It has been suggested that monolayers silicon dioxides or silicates can preferentially coat each atomic plane.[9] After the completion of etching, holes that permeate through the entire Si wafer are laser drilled and **Figure 4.6** shows an SEM micrograph of a fabricated pixel array post-laser drill. In the laser drill process, a tightly focused laser beam continuously heats the sample and material is removed by evaporation. During the laser drilling, some of the evaporated Si deposits the sidewalls. To achieve smooth sidewalls, a second round of KOH etching is performed. **Figure 4.7** shows the

SEM images of a sample before and after the second KOH etching. The pixel array is then sputter-coated with silver as the reflective layer.

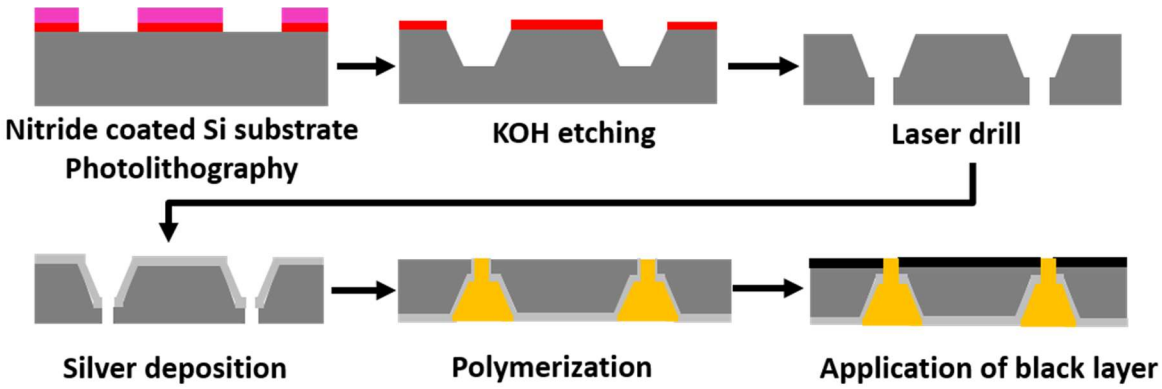

Figure 4.5 Process flow to fabricate micropixel array.

The next step is the polymerization of the micropixel array inside the holes. It is important to avoid any agglomeration of QD in a polymer-QD composite since any agglomeration inevitably reduces the efficiency of the luminescent layer. It has been shown that poly(lauryl methacrylate) (LMA), along with a high concentration of cross-linker ethylene glycol dimethacrylate (EDGMA), can be used to achieve well-dispersed QD.[10] A very similar procedure, with the addition of UV photoinitiated polymerization to speed up the polymerization process,[11] is used to make QD-doped polymer layers.

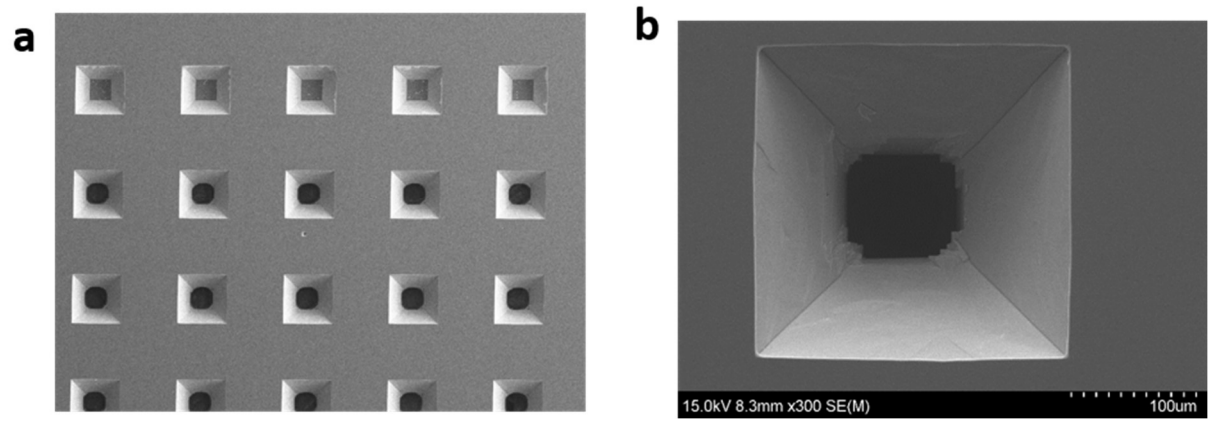

Figure 4.6 a) Fabricated micropixel array after laser drilling process comparing the drilled pixels (bottom 3 row) with intact pixels b) A single pixel after laser drilling.

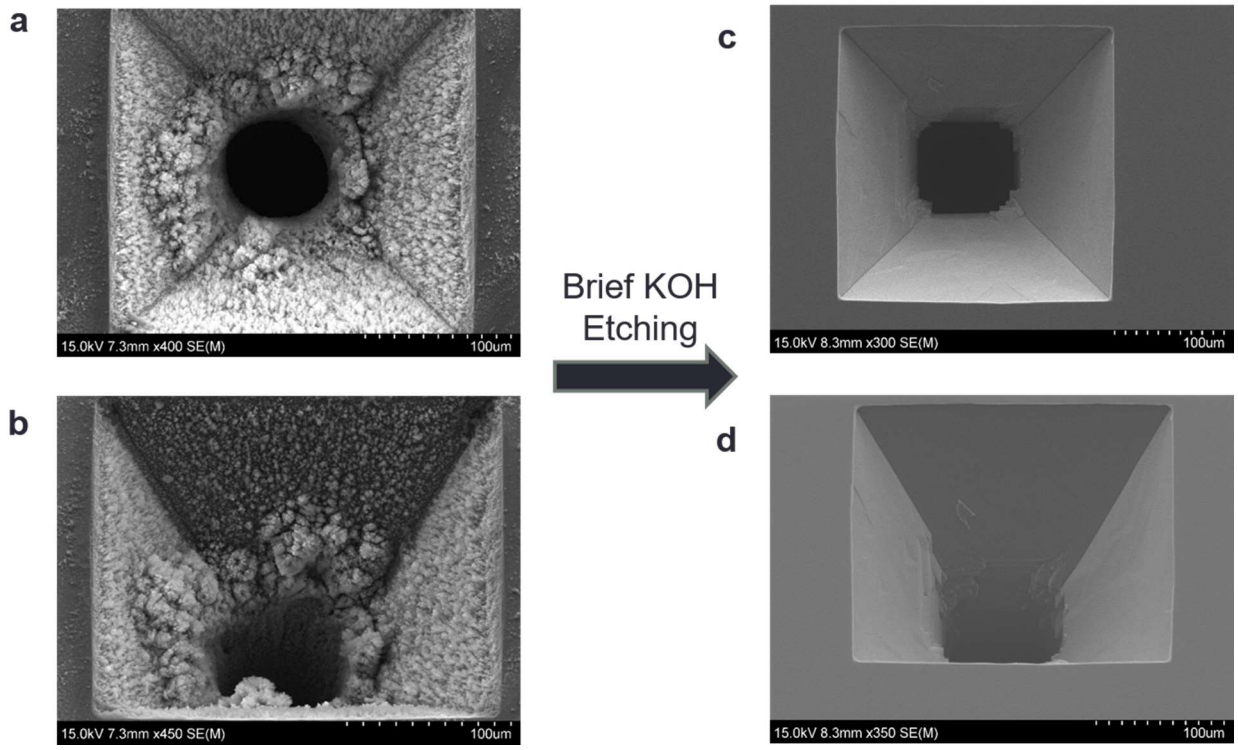

Figure 4.7 SEM images of a single pixel after laser drilling process. a) and b) are taken right after drilling. c) and d) show the pixel after a brief KOH etching. Smooth sidewalls can be obtained after the second KOH etching.

Specifically, Lauryl Methacrylate and EDGMA cross-linker are introduced to a flask at a 10:1 concentration ratio. Using a syringe, several drops of Trioctylphosphine (TOP) is placed into the flask as a surfactant. CdSeS/ZnS alloyed quantum dots in toluene are introduced to the flask. Afterwards, a rotary evaporator is used to remove the solvent. Polymerization of the QD-PLMA film inside the holes is performed by using a PDMS slab as a temporary substrate on the back side to prevent leakage of the QD-LMA monomer solution prior to polymerization. The prepared liquid fills the etched patterns with the push of liquid from a pipette. After the filling, UV illumination is used to polymerize the film inside a glovebox. For a relatively low concentrated film, it takes around 30 minutes of curing time. After fully curing of the polymer, any film remaining on the non-patterned Si wafer is removed using a razor blade. The final step is to apply an absorptive material over the external surface of the device; here, we use a thin membrane of bPDMS. Holes are generated in the bPDMS film using a needle under a microscope to align with the pixels.

4.3 Results

The extraction efficiency ($\eta_{extract}$) as follows:

$$\eta_{extract} = \frac{I_{PL}}{I_S}$$

A sample with 69 pixels was used to measure $\eta_{extract}$ of the optical microcavity array. For the micropixel array sample, we define I_S as the intensity of light at the excitation wavelength with an empty pixel array (i.e., prior to polymerization). The output, I_{PL}, is then measured after polymerization with the QD-PLMA film. $\eta_{extract}$ is then calculated from the above equation. **Figure 4.9** shows the input spectrum (in black) and emitted light as well as the leakage (in red). The $\eta_{extract}$ of this micropixel array is calculated to be 52.2% with a leakage of 20.1%. Increasing

the optical density of the QD-PLMA film might result in a higher $\eta_{extract}$ by reducing the transmittance through the film, thereby reducing the leakage. Alternatively, a thicker Si wafer can be used that allows thicker QD film which reduces leakage, resulting in a higher $\eta_{extract}$.

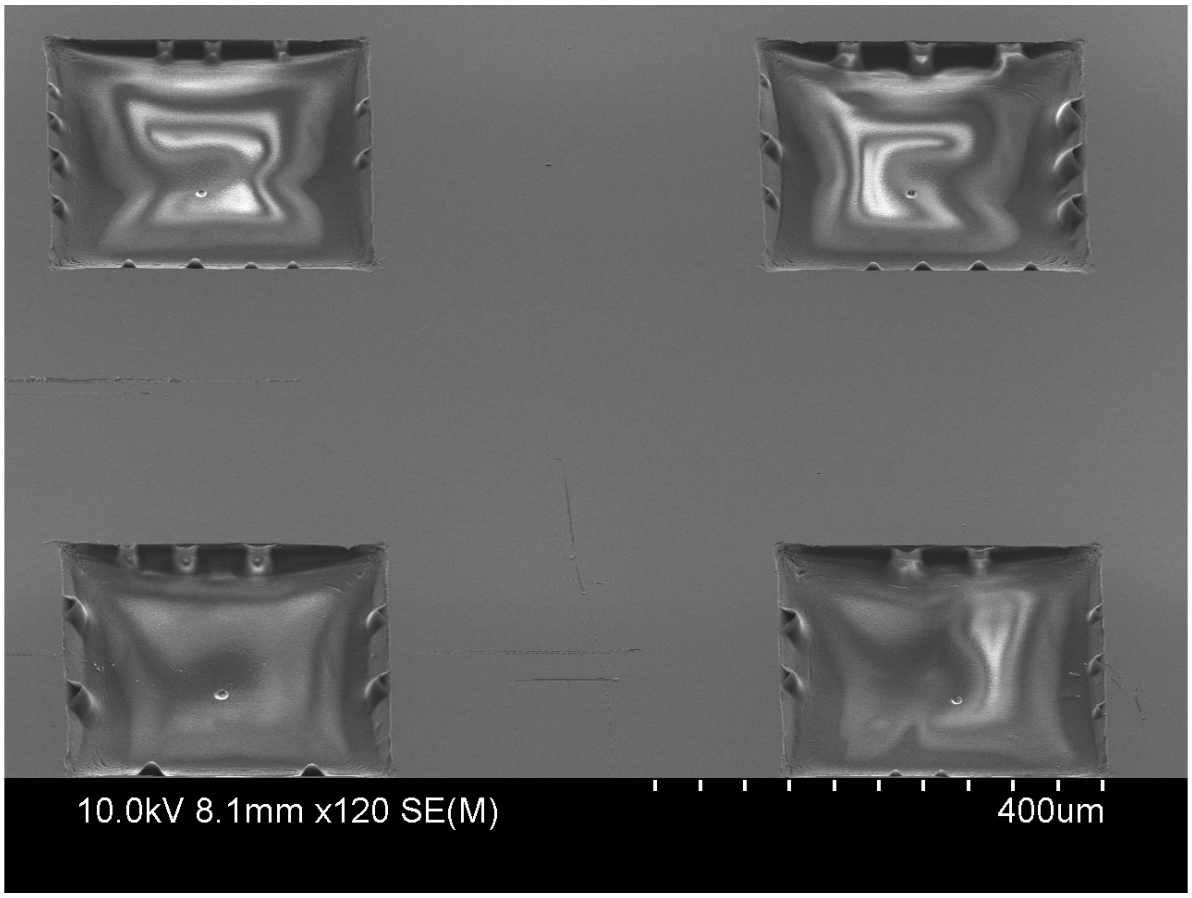

Figure 4.8 SEM micrograph showing 4 pixels filled with QD film. The patterned pixels are almost completely filled with some meniscus effect at the edges which is an effect of capillary action due to surface tension in the monomer:QD solution.

Image of the micropixel array with randomly patterned pixels under dark ambient conditions are shown in **Figure 4.10**. The image is taken when the backlight is on at low ambient light and the light emission is clearly seen at the central region of the sample for each pixel. On the other hand, **Figure 4.11** shows the device when the backlight is on and the device is

illuminated with bright artificial ambient light and here, light emission is still observed for each pixel, paving the way towards a device that is readable under high ambient light conditions such as a sunny day or very bright indoors. We also observed the device when placed under a substantial ambient light with the backlight off (picture not shown). The overall device is perceived as very dark, again indicating substantial absorption of ambient light suitable for high ambient contrast ratio displays.

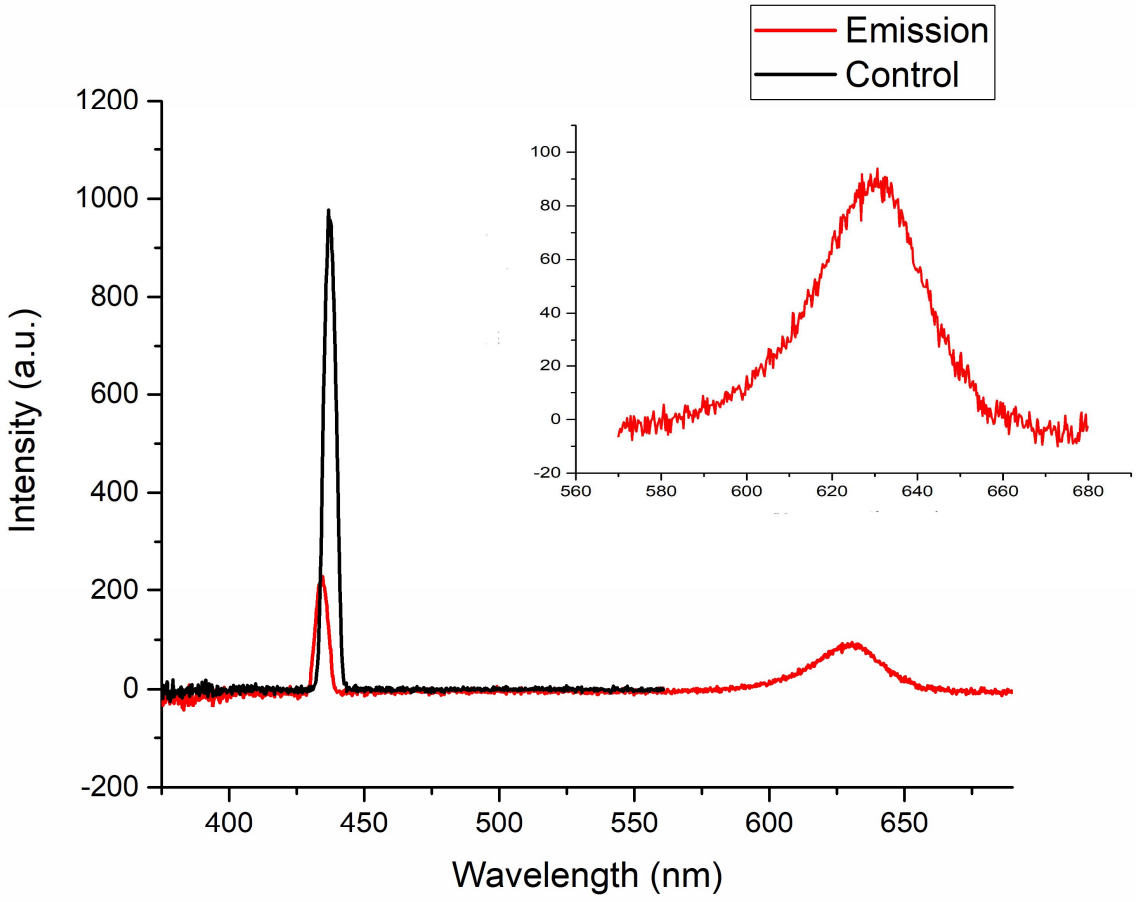

Figure 4.9 Spectra of emission (in red) and control (in black) are shown. The intensity of light at the excitation wavelength with an empty pixel array is defined to be control. The inset shows photoluminescence part.

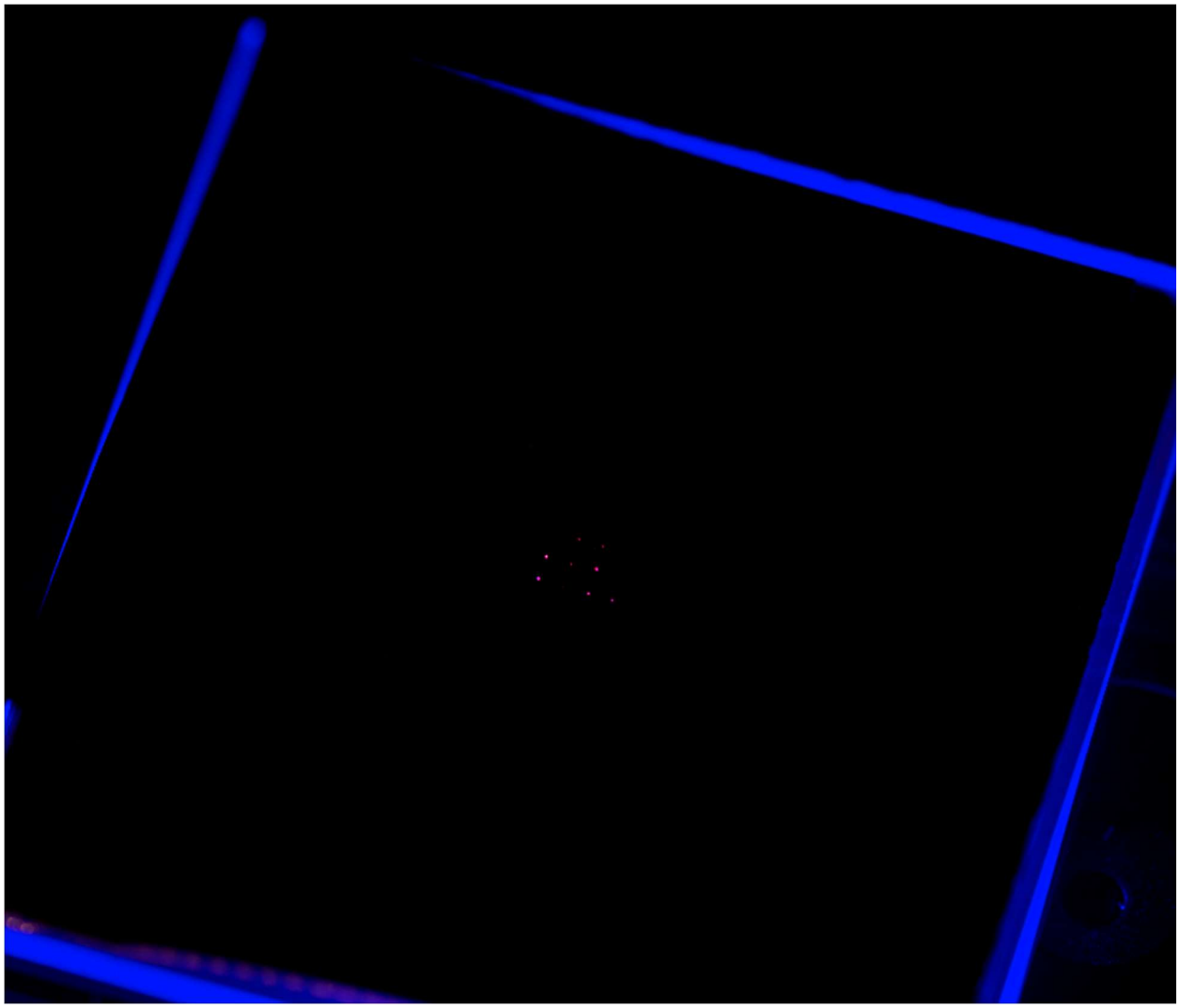

Figure 4.10 Photograph of the fabricated micropixel array design having several randomly patterned pixels under dark ambient conditions.Light is extracted from 80 μm openings.

In summary, the motivation of this work is to demonstrate the proof-of-concept luminescent cavity design that was mentioned in the previous chapter can be miniaturized and can include multiple, individually addressable pixels. We have combined traditional microfabrication techniques (photolithography, wet etching, and deposition) with laser drilling to define spaces to fill QD films. We have shown an extraction efficiency of 52.2% while 20.1% of

the source light passes through the device without getting absorbed. The pictures of the devices taken in both dark and intensely illuminated conditions show the potential of the design as a high ambient contrast ratio device.

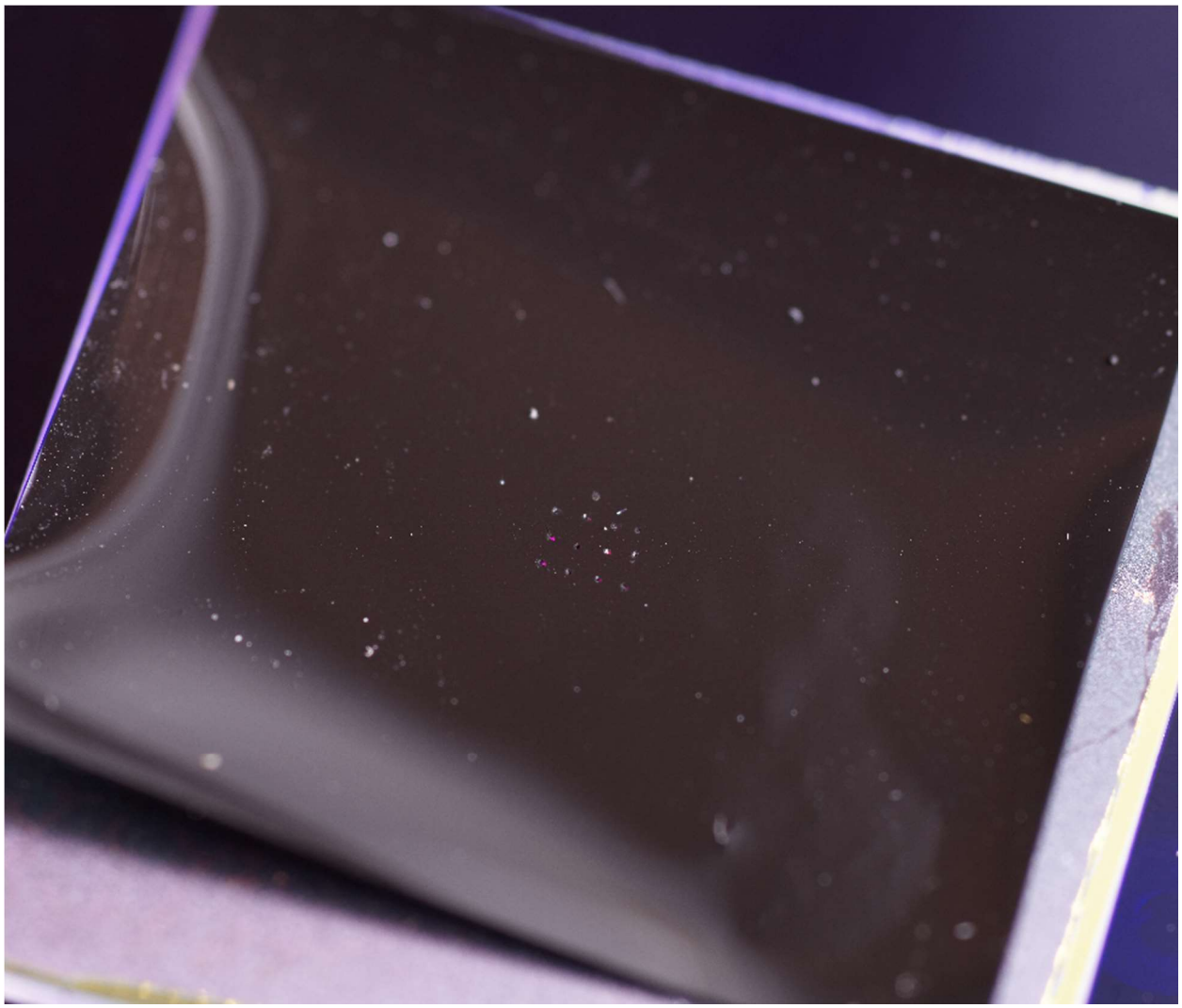

Figure 4.11 Photograph of the micropixel array taken under bright ambient light when the backlight is on. Light extraction from the pixels (at the center of the image) can be observed. The pixel size is 80 μm.

4.4 References

1. Carles Mitja. Displays pixel size. https://carlesmitja.net/2011/03/02/displays-pixel-size (accessed Jun 2, 2018)
2. Hecht, E. Optics. Addison-Wesley, 2002
3. Dumanli, A. G. & Savin, T. Recent advances in the biomimicry of structural colours. *Chemical Society Reviews* (2016). doi:10.1039/c6cs00129g
4. Maldovan M. and Thomas E. L., Periodic Materials and Interference Lithography, Wiley, Weinheim, 2009
5. Kooy, N., Mohamed, K., Pin, L. T. & Guan, O. S. A review of roll-to-roll nanoimprint lithography. *Nanoscale Res. Lett.* (2014). doi:10.1186/1556-276X-9-320
6. Lee, H. S., Shim, T. S., Hwang, H., Yang, S. M. & Kim, S. H. Colloidal photonic crystals toward structural color palettes for security materials. *Chem. Mater.* (2013). doi:10.1021/cm4012603
7. Franssila, S. *Introduction to Microfabrication*. *Introduction to Microfabrication* (2010). doi:10.1002/9781119990413
8. Palik, E. D. A Raman Study of Etching Silicon in Aqueous KOH. *J. Electrochem. Soc.* (1983). doi:10.1149/1.2119866
9. Palik, E. D., Faust, J. W., Gray, H. F. & Greene, R. F. Study of the Etch-Stop Mechanism in Silicon. *J. Electrochem. Soc.* (1982). doi:10.1149/1.2124367
10. Lee, J., Sundar, V. C., Heine, J. R., Bawendi, M. G. & Jensen, K. F. Full color emission from II-VI semiconductor quantum dot-polymer composites. *Adv. Mater.* (2000). doi:10.1002/1521-4095

11. Bronstein, N. D. *et al.* Luminescent solar concentration with semiconductor nanorods and transfer-printed micro-silicon solar cells. *ACS Nano* (2014). doi:10.1021/nn404418h

CHAPTER 5

SUMMARY OF WORK AND FUTURE OUTLOOK

5.1 Summary of Work

This dissertation has focused on various designs to manage the light spectrum for photonic devices to achieve higher efficiencies. Due to broadband nature of most of the light sources and narrow-band sensitivity of detectors (e.g. a photovoltaic cell), spectrum management such as splitting, up-converting or down-converting the incoming light offers better performance.

Chapter 2 tackles the problem of single-junction photovoltaic cells' inefficient utilization of the energy contained in the full spectrum of sunlight which is the greatest source of loss in conventional solar cell designs. To overcome this deficiency, we propose a multi-junction system that laterally splits the solar spectrum onto a planar array of single-junction cells with different bandgaps. As a first demonstration, we designed, fabricated, and characterized dispersive diffractive optics which spatially separated the visible (360-760nm) and near-infrared (760-1100nm) bands of sunlight in the far field. Inverse electromagnetic design was used to optimize the surface texture of the thin diffractive phase element. An optimized thin film fabricated by femtosecond two-photon absorption 3D direct laser writing shows an average splitting ratio of 69.5% between the visible and near-infrared light over the 380-970nm range. The splitting efficiency is predicted to be 80.4% assuming a structure without fabrication errors. Further design optimization and fabrication improvements have the potential to improve the splitting efficiency under direct sunlight, allow for a more compact geometry, and ultimately incorporate a greater number of photovoltaic bandgaps.

Chapter 3 deals with improving efficiency and ambient contrast ratio of liquid crystal display (LCD) devices. LED-backlit (LCD) devices currently dominate the color display market, in part because they are relatively inexpensive and reliable to produce. LCD produces color by filtering white light through color filters placed adjacent to the liquid crystal (LC) layer. Each sub-pixel of the display contains a color filter to output either red, green or blue light. Since the color filter eliminates two out of three colors of the RGB (red-green-blue) spectrum, there may be substantial losses in optical intensity, which leads to higher power requirements. Another issue with LCDs and in general displays is they may suffer from a low ambient contrast ratio because of reflection of external light from the front surface. To mitigate these issues, we propose a proof-of-concept optical microcavity comprising an enclosed cavity having a front wall and a back wall, where the front wall comprises a pinhole opening for emission of light from the cavity and the back wall is configured to transmit light into the cavity. An outer surface of the front wall absorbs some or substantially all optical wavelengths of externally incident light so as to appear black. An inner surface of the front wall and sidewalls comprises a high light reflectivity to promote photon recycling within the cavity and light emission through the pinhole opening. We achieved a photon extraction efficiency of 40.9% for devices having 11% opening area which is significantly better than the theoretical maximum possible efficiency of an absorptive color filter of 33.3%.

Portable displays have a pixel pitch of around 50-250 μm. To demonstrate our proof-of-concept design can be integrated into modern portable electronic displays, **Chapter 4** focuses on producing micropixel arrays. We have designed, fabricated and characterized devices having tens of pixels with each pixel having a size of 80 μm. We used microfabrication techniques such as photolithography, wet etching, plasma etching, and sputter deposition to define the pattern.

Laser drilling is used to generate through holes where QD film can reside. Photon extraction efficiency of the individually addressable, micropixel array was measured to be 52.2% with 20.1% of the light going through the array without getting absorbed (i.e., leaked).

5.2 Future Outlook

Although this dissertation focuses on improving efficiency and ambient contrast ration of LCD devices, the idea of cycling photons inside a micro-cavity and allowing the extraction of photons from only a small opening in the front wall can potentially benefit OLED displays, in addition to LCDs because of the employed metal cathode in OLED displays, reflection of ambient light is a big concern[12]. Some modifications to the proposed design are necessary to be integrated into OLED displays. The back wall may comprise an organic emissive layer for generating light of a predetermined wavelength range (or desired color) in the cavity, such that the subpixel is part of an OLED. The OLED does not employ a backlight; rather, it relies on electrically driven photon emission from the organic emissive layer, which may comprise an organic semiconductor. By utilizing a top-emitting organic emissive layer and surrounding it with highly reflective front and side wall surfaces, leaving only a small opening through the front wall, an OLED comprising an optical cavity may be formed. For the device to function efficiently, reabsorption of emitted photons inside the cavity is preferably minimized. Thus, the organic emissive layer may have a large Stokes shift. A suitable organic semiconductor may comprise 4-(dicyanomethylene)-2-tert-butyl-6-(1,1,7,7-tetramethyljulolidin-4-yl-vinyl)-4H-pyran (DCJTB). A phosphor may or may not be included within the cavity; light of a desired color may be emitted directly from the organic emissive layer, and since a bandpass filter is not needed for light transmission into the cavity, down-conversion is not required to prevent escape of the light.

In addition, the need for circular polarizers, which are typically required for OLED displays, may be eliminated.

While flat luminescent layers are useful for proof-of-concept, alternative geometries could result in even better performance. In the luminescent solar concentrator (LSC) literature, alternatives for planar LSC exist, such as cylindrical LSCs, which have been shown to have higher geometric concentration ratio (up to 1.9 times the planar geometry).[34] For our purposes, this means concentrating light into a smaller aperture and thus, having a higher contrast ratio. On the quest for exploring alternative geometries, looking into methods of tapering the sidewalls of the luminescent concentrator as a route towards simplifying the fabrication process while potentially reducing losses through the edges of the device might be desirable. Specifically, a hemispherical shape is one example of a tapered geometry. There is a literature dating back to 1980s on making hemispherical microlenses out of a polymer or glass.[5] One of the earliest demonstrations was the fabrication of Fresnel zone plates made of PMMA using e-beam lithography.[6] A few years later, photosensitive glass (i.e., glass doped with metal colloids such as silver) was used to make microlens arrays.[7] Another method of producing microlenses is by taking advantage of the optically induced swelling of optical recording materials such as dichromated gelatin.[8] Micron-sized graded index (GRIN) lenses, which have refractive index modulation throughout the substrate, were also produced. A common way of producing GRIN lenses is by using ion diffusion,[8] but porous silicon lenses can also be used to achieve more drastic refractive index modulation and it is a technique used in our lab.[9] One of the most straightforward and efficient methods to make microlenses is to use thermal reflow process.[10] Thermal reflow of photoresist is a method pioneered by Popovich[11] in 1988 and it is currently the method of choice to produce luminescent hemispheres. In this method, microlenses are produced

by heating the patterned photoresist layer. The most energetically favorable configuration of the liquid resist is the hemisphere. A wide range of microlenses have been fabricated with diameters ranging from 5 μm to 1000 μm.[1213] Once a microlens is made out of photoresist, it is possible to convert this pattern to another material. Microlens photoresist arrays have been transformed into a metal mold by electroplating,[14] with the metallic master mold then used to produce thermoplastic microlens arrays with a hot embossing method.[15] One way to produce hemispherical luminescent layers is to electrodeposit a conductive material to the microlens pattern. The capacity to do this is readily available as electrodeposition of various materials is performed in our laboratory. Afterward, this mold can replace one of the flat quartz layers used to make luminescent films and produce the desired hemispherical shape. An alternative method of producing hemispherical QD-polymer shape is using UV curable resins mixed with the appropriate QD directly without any microfabrication. It has been shown as early as in 1997 that microlens arrays can be fabricated by putting small droplets of UV curable resins or optical adhesives to a substrate. By the action of surface tension, these droplets reform into a spherical shape.[16] These small droplets can also be placed with the help of an ink-jet printer.[17] Here at UIUC, researchers have used electrohydrodynamic jet (E-jet) printing to write a QD-polymer mixture and used UV light to polymerize a luminescent layer.[18] It is important to note that changing the geometry of the luminescent layer will not affect the rest of the fabrication methods of the luminescent microcavity. The method of assembly is to place the luminescent layer on the DBR and sputter reflective material on top of the luminescent material.

5.3 References

1. Singh, R., Narayanan Unni, K. N., Solanki, A. & Deepak. Improving the contrast ratio of OLED displays: An analysis of various techniques. *Optical Materials* (2012). doi:10.1016/j.optmat.2011.10.005
2. Chen, H., Tan, G. & Wu, S.-T. Ambient contrast ratio of LCDs and OLED displays. *Opt. Express* (2017). doi:10.1364/OE.25.033643
3. McIntosh, K. R., Yamada, N. & Richards, B. S. Theoretical comparison of cylindrical and square-planar luminescent solar concentrators. *Appl. Phys. B Lasers Opt.* (2007). doi:10.1007/s00340-007-2705-8
4. Bose, R., Farrell, D.J., Pardo-Sanchez, C., Pravettoni, M., Mazzer, M., Chatten, A.J., Barnham, K. W. J. Luminescent Solar Concentrators: Cylindrical Design. in *24th, European photovoltaic solar energy conference* 359–362 (2009).
5. O'Neill, F. T. & Sheridan, J. T. Photoresist reflow method of microlens production Part I: Background and experiments. *Opt.* (2002). doi:10.1078/0030-4026-00186
6. Fujita, T., Nishihara, H. & Koyama, J. Fabrication of micro lenses using electron-beam lithography. *Opt. Lett.* (1981). doi:10.1364/OL.6.000613
7. Borrelli, N. F., Morse, D. L., Bellman, R. H. & Morgan, W. L. Photolytic technique for producing microlenses in photosensitive glass. *Appl. Opt.* **24,** 2520–2525 (1985).
8. Klug, R. & Brenner, K. H. Implementation of multilens micro-optical systems with large numerical aperture by stacking of microlenses. *Appl. Opt.* (1999). doi:10.1364/AO.38.007002
9. Ning, H. *et al.* Transfer-Printing of Tunable Porous Silicon Microcavities with Embedded Emitters. *ACS Photonics* (2014). doi:10.1021/ph500230j

10. Ashraf, M., Gupta, C., Chollet, F., Springham, S. V. & Rawat, R. S. Geometrical characterization techniques for microlens made by thermal reflow of photoresist cylinder. *Opt. Lasers Eng.* (2008). doi:10.1016/j.optlaseng.2008.05.008

11. Popovic, Z. D., Sprague, R. A. & Neville Connell, G. A. Technique for monolithic fabrication of microlens arrays. *Appl. Opt.* (1988). doi:10.1364/AO.27.001281

12. Nussbaum, P., Völkel, R., Herzig, H. P., Eisner, M. & Haselbeck, S. Design, fabrication and testing of microlens arrays for sensors and microsystems. *Pure Appl. Opt. (Print Ed. (United Kingdom)* (1997). doi:10.1088/0963-9659/6/6/004

13. Audran, S. *et al.* Study of mechanisms involved in photoresist microlens formation. *Microelectron. Eng.* (2006). doi:10.1016/j.mee.2006.01.150

14. Lin, T. H., Hung, S. Y., Yang, H. & Chao, C. K. Fabrication of a microlens array electroformed mold with low roughness and high hardness. *J. Micromechanics Microengineering* (2007). doi:10.1088/0960-1317/17/3/001

15. Kwon, H., Yee, Y., Jeong, C.-H., Nam, H.-J. & Bu, J.-U. A high-sag microlens array film with a full fill factor and its application to organic light emitting diodes. *J. Micromechanics Microengineering* (2008). doi:10.1088/0960-1317/18/6/065003

16. Keyworth, B. P., Corazza, D. J., McMullin, J. N. & Mabbott, L. Single-step fabrication of refractive microlens arrays. *Appl. Opt.* (1997). doi:10.1364/AO.36.002198

17. Ando, Y. I. and S. K. and Y. A. and Y. Ink-Jet Fabrication of Polymer Microlens for Optical-I/O Chip Packaging. *Jpn. J. Appl. Phys.* **39,** 1490 (2000).

18. See, G. G. *et al.* Polarized quantum dot emission in electrohydrodynamic jet printed photonic crystals. *Appl. Phys. Lett.* (2015). doi:10.1063/1.4927648